Università degli Studi di Trento
Facoltà di Scienze Matematiche Fisiche e Naturali
Dipartimento di Fisica

Mean-field theory for the dynamics of superfluid fermions in the BCS-BEC crossover

Thesis submitted for the Ph.D degree
in physics

Ph.D thesis by
Peng Zou

DOTTORATO DI RICERCA IN FISICA, XXVI CICLO
May 16th 2014

Acknowledgement

First I want to express my deep gratitude to my supervisor Prof. Franco Dalfovo, who always gave his scientific support, patience, guidance and encouragement to me for the whole three years. His rigorous attitude and careful spirit on science will influence my whole life. I am indebted to Robin Scott, my "little tutor", who taught me many numerical skills during my first year, with many valuable discussions; he also showed me how to canoe.

The BEC group is like a big and warm family, with the most experienced and kind elder Lev Pitaevskii, the leader Sandro Stringari and the manager Stefano Giorgini, and all the others: Iacopo, Chiara, Alessio, Gabriele, Giacomo, David, Riccardo, Marta, Tomoki, Zeng-Qiang, Natalia, Marek, Pierre-Élie, Hannah, Nicola, Giovanni, Luis, Alberto, Simone D., Grazia, Simone S., Giulia, Robin, Marco, Rifat Onur, Yun, Stefano, Yan-Hua. I appreciate all the time with all of you, from the picnics, excursions, Christmas lunch to each parties, there are so many good memories and joys. In particular, I am indebted to secretaries, Beatrice Ricci, who helped to solve all difficulties for my initial travel to Italy, Micaela Paoli, Flavia Zanon and Rachele Zanchetta, who dealt with all boring daily routine for me, and also the technician Giuseppe Froner. I want to thank Stefano Finazzi for sharing the knowledge related to Rydberg atoms. I also thank Marta for discussions about time-dependent simulations and Josephson effect on bosons. I thank Yun Li for sharing the experience on solving the Gross-Pitaevskii equation numerically, and Zeng-Qiang Yu for sharing his knowledge of fermions.

It is very fortunate to have chance to discuss physics with Augusto Smerzi, Aurel Bulgac, Michael McNeil Forbes and Rishi Sharma. The talks with them deeply helped me to understand the Josephson effect, the two-mode model and the

superfluid local density approximation theory. I thank Hui Hu for suggesting me to calculate the dynamic structure factor and his patient reply to all my questions.

Really I am really grateful to Milo and his family. I will remember forever my second day in Trento, a kind family, using their private car, helping a lost foreigner to find his way home in a dark and rainy night.

Thank Yan-Hua Hou and all other dear friends in Trento, thank you very much for all your encouragements and help during my daily life. Although I do not list all of your names here, it is the existence of all of you that made my life in Trento interesting, happy, rich and different. How nice and beautiful the memories are in San Bartolameo, Povo, Monte Chegul, Fiume Adige, Mausoleo di Cesare Battisti, etc.. Wish all your dreams come true.

Contents

Acknowledgement **i**

Contents **iii**

1 Introduction **1**
- 1.1 Historical overview 1
- 1.2 Josephson effect in ultracold quantum gases 3
- 1.3 Dynamic structure factor 7
- 1.4 Thesis outline 11

2 Bogoliubov-de Gennes equations **13**
- 2.1 Derivation of BdG equations 13
- 2.2 BdG equations for uniform system in a box 17
- 2.3 Calculation of ΔE in the presence of a potential barrier 22
- 2.4 TDBdG equations in a box 25

3 Double wells and BdG equations **29**
- 3.1 Josephson oscillations and self-trapping with TDBdG 29
- 3.2 Two-mode model for small Josephson oscillations 34
- 3.3 Strong coupling 40

4 Nonlinear Josephson equations and density functionals **45**
- 4.1 Josephson effect in NLSE 45
- 4.2 Can fermions exhibit π-mode oscillations? 51
- 4.3 Superfluid local density approximation 53
- 4.4 Josephson effect with SLDA 56

5 Dynamic structure factor **59**
5.1 Random phase approximation 59
5.2 Dynamic structure factor in BdG theory 62
5.3 Dynamic structure factor in SLDA theory 69
5.4 Results 73

6 SLDA at finite temperature **79**
6.1 $\mu(T)$ and $\Delta(T)$ 79
6.2 $S(q,\omega)$ at finite temperature 83

7 Conclusions and Perspectives **87**

A 4th order Runge Kutta method algorithm **91**

Bibliography **92**

List of Publications **101**

List of Figures

1.1 The Gaussian-shape double well potential. In experiments, laser beams and magnetic traps can be used to generate such external potential for the confinement of ultracold atoms. 4

1.2 Absorption images of a ^{87}Rb condensate confined in a double-well potential from Josephson oscillations (left) to self-trapping (right). In the Josephson regime the atoms tunnel back and forth between the two wells, while in the self-trapping regime more atoms always remain in the left well. Taken from Michael Albiez *et al* [1]. 6

1.3 Bragg spectra showing density dynamic structure factor $S(q, \omega)$ for trapped Fermi gases across the BCS-BEC crossover. Magnetic field and $1/(k_F a)$ for each spectrum are given in the legend. The inset shows the 750 and 991 G spectra along with the calculated $S(q, \omega)$ for an ideal Fermi gases and molecular BEC at 750G. Taken from G. Veeravalli *et al* [2]. 9

2.1 Density and order parameter of unitary fermions for the symmetric (solid lines) and anti-symmetric (dashed lines) solutions of the stationary BdG equations in a box of length $L = 30k_F^{-1}$ and $L_\perp = 13k_F^{-1}$. The particle number is $N = 156$ in both cases. The density n_0 is the ground state density in the center of the box. 19

2.2 Energy per particle of the ground state (left) and the lowest antisymmetric state (right) of unitary fermions in a box with periodic boundary conditions in the transverse direction and closed boundary conditions in the longitudinal direction. For each longitudinal length L, the two states have the same number of particles N. The number N, as a function of L, is such that the bulk density in the ground state is the same for all points. Energies are plotted as a function of $1/(k_F L)$. From a linear fit we extract the value in the $1/L \to 0$ limit, which is 0.351 and 0.348 for E^+/N and E^-/N, respectively. These values agree with the analytic BdG prediction $(3/5)(1+\beta) = 0.354$ for the ground state energy of a unitary gas. The remaining discrepancy, of the order of 1%, is due to numerical uncertainties induced by the finite cutoff energy, the discretization of the quasiparticles states in the transverse directions, and other sources of small numerical fluctuations. 20
2.3 Left panel: energy difference $\Delta E = E^- - E^+$ per unit area, obtained from the energies plotted in Fig. 2.2. In the $(1/L) \to 0$ limit, the points should converge to the analytic BdG prediction $\epsilon_s = (1+\beta)^{1/2}/(8\pi\sqrt{3}) \simeq 0.0176$ [3] for the energy of a dark soliton in an infinite uniform gas. The value extracted from a linear fit to the data agree with this prediction within a 3% uncertainty. Right panel: soliton energy in the box as defined in Eq. (2.19). The $1/L \to 0$ limit is the same as in the left panel, but convergence is faster. 21
2.4 The rectangular-shape double well potential with a central barrier, whose width and height are d and V_0, respectively. 23
2.5 Energy difference $\Delta E = E^- - E^+$, divided by the area $L_\perp^2$, as a function of the barrier height V_0 and width d. Here $N = 156$, $L_\perp = 13 k_F^{-1}$, $L = 30 k_F^{-1}$, and $E_{\text{cut}} = 70 E_F$. 24
2.6 Left: energy difference $\Delta E = E^- - E^+$, divided by the area $L_\perp^2$, as a function of the barrier height V_0 for different widths d. Right: the same quantity as a function of the barrier width d for different values of height V_0. All the other parameters are the same as in the previous figure. 24

2.7 The density profile (left) and the order parameter profile (right) of the unitary fermions in a box, with a central barrier, whose height and width are $V_0 = 0.2E_F$ and $d = 20k_F^{-1}$, respectively. The black line is the ground state solution, while the red line is the anti-symmetric solution (or dark soliton solution). Both solutions have the same particle number $N = 164$. 25
2.8 Left panel: sound wave-packets produced by an initial density perturbation in the center of the box and propagating back and forth in the uniform unitary gas. Right panel: same as before but for a stronger perturbation, at which, in addition to sound, generates also two dark solitons moving in opposite directions, slower than sound. . 26
2.9 Breathing mode of unitary fermions in a harmonic trap $V_{\text{trap}} = m\omega_{\text{trap}}^2 x^2/2$. The frequency ω_{breath} of the trap is initially $0.4E_F/\hbar$, then suddenly changed to $0.5E_F/\hbar$. A breathing mode is generated, with frequency $\omega_{\text{breath}} = 0.86E_F/\hbar$. 27
2.10 Soliton oscillation in a harmonic trap $V_{\text{trap}} = m\omega_{\text{trap}}^2 x^2/2$, with trapping period $T_{\text{trap}} = 2\pi/\omega_{\text{trap}} = 63\hbar/E_F$. The period of this oscillation is about $108\hbar/E_F \approx 1.71T_{\text{trap}}$. 28

3.1 The rectangular-shape double well potential with a middle barrier, whose width and height is d and V_0, respectively. An offset potential V_{off} in the left helps to produce the initial population imbalance. . . . 30

3.2 Evolution of the density distribution $n(x,t)/n_0$ (left plots) and the phase $\phi(x,t)/\pi$ (right plots) of a two-component superfluid Fermi gas at unitarity and zero temperature obtained by solving the time-dependent BdG equations (Eqs. 2.15). Time, in units of $\hbar/E_F$, flows from top to bottom. The gas is uniform in the transverse directions and confined between hard walls in the longitudinal direction at $x = \pm L/2$ with $L = 20k_F^{-1}$, with a central square barrier of height $V_0 = 5E_F$ and width $d = 0.6k_F^{-1}$ respectively. The number of atoms is $N = 100$. The initial imbalance is produced by adding a constant offset potential $V_{\rm off}$ at $t < 0$ on the left side only; here we use $V_{\rm off} = 0.02E_F$ (upper plots) and $V_{\rm off} = 0.05E_F$ (lower plots), which corresponds to an initial relative imbalance $z_0 = -0.024$ (lower plots) and $z_0 = -0.06$ (lower plots). 31
3.3 Relative population imbalance (left) and phase difference (right) as a function of time for the same simulation of Fig. 3.2 Black lines:$|z_0| = 0.024$ and $V_{\rm off} = 0.02E_F$; Red lines: $|z_0| = 0.06$ and $V_{\rm off} = 0.05E_F$ . . 32
3.4 The current-phase relation obtained in four BdG simulations with the same barrier ($V_0 = 5E_F$ and $d = 0.6k_F^{-1}$) and different initial imbalance, $z_0 = -0.024$ (a), -0.06 (b), -0.078 (c), and -0.096 (d). The red dashed line in panel (d) is obtained by solving the nonlinear Schrödinger equation in the same configuration and for the same initial imbalance. 33
3.5 Same as in Fig. 3.2 but for a larger initial imbalance (in the upper two panels $z_0 = -0.096$, and in the lower ones $z_0 = -0.121$), such to cause self-trapping. 34
3.6 Relative population imbalance $z(t)$ and phase difference $\Phi(t)/\pi$ for the same simulation of Fig. 3.5. Black lines: $|z_0| = 0.096$ and $V_{\rm off} = 0.08E_F$; Red lines: $|z_0| = 0.121$ and $V_{\rm off} = 0.1E_F$. 35

3.7 Population imbalance *vs.* phase difference in simulations with the same barrier ($V_0 = 5E_F$ and $d = 0.6k_F^{-1}$) and different initial imbalance, $|z_0| = 0.024$, 0.06, 0.0856, 0.0869, 0.096, 0.121, from the inner ellipse to the outer open trajectory. The red ellipse corresponds to the simulation in Fig. 3.2; the pink open trajectory corresponds to the simulation in Fig. 3.5. The transition from Josephson oscillations to self-trapping occurs at about $|z_0| \approx 0.0869$. 35

3.8 The Josephson current I_J extracted from time-dependent BdG simulations in the regime of small oscillations and weak tunneling is plotted as a function of the energy difference $\Delta E = E^- - E^+$, between the lowest antisymmetric and symmetric solutions of the stationary BdG equations (2.12). All points correspond to $E_{\text{cut}} = 50E_F$, $N = 100$, $L = 20k_F^{-1}$ and $L_\perp = 13k_F^{-1}$, while (V_0/E_F, k_Fd) is (5,1), (5,0.8), (5,0.6), (6,0.45), (5,0.5), (4,0.6), (4,0.55), for points from bottom-left to top-right. The red line represents the equality $\hbar I_J = \Delta E$. 37

3.9 Period of small amplitude Josephson oscillations as a function of $\Delta E/2$, in log-log scale. The black solid line is the period T_{BdG} observed in time dependent BdG simulations for 99.3024 atoms in a double well potential. For each black point the width of the barrier is the same, $d = 0.6k_F^{-1}$, while its height decreases from $V_0 = 7E_F$ (leftmost point) to $0.6E_F$ (rightmost point). The red dashed line is the period $T_p = 2\pi/\omega_p = 2\pi\hbar/\sqrt{E_C E_J}$ of plasma oscillations, where E_C and E_J are calculated by solving the stationary BdG equations (2.12), assuming $E_J = \Delta E/2$. 38

3.10 Current-phase relation for a unitary Fermi gas in the presence of a square barrier with $V_0 = 0.4E_F$ and $d = 4k_F^{-1}$. Black points were calculated in [4] by solving the stationary BdG equations in a uniform system and looking for solutions at constant current. The red lines are the results of our TDBdG simulations with a small initial imbalance in the double well potential with the same square barrier. The imbalance is produce with an offset potential $V_{\text{off}} = 0.02E_F$ (left) and $0.04E_F$ (right). 41

3.11 Evolution of the density distribution $n(x,t)/n_0$ and phase $\phi(x,t)$ at unitarity, obtained by solving the time-dependent BdG equations (2.15), as in Fig. 3.2, but for a lower barrier ($V_0 = 1E_F$ and $d = 0.6k_F^{-1}$). The initial imbalance is $|z_0| = 0.353$. Solid and dashed lines in the left panel represent the propagation of a sound-like density wave packet and a grey soliton, respectively. 42

3.12 Phase-current relations obtained in time dependent BdG simulations for increasing initial population imbalance, from $V_{\text{off}} = 0.02E_F$ (top left panel) to $V_{\text{off}} = 0.4E_F$ (bottom right). The height and width of barrier are $V_0 = 1E_F$ and $d = 0.6k_F^{-1}$, respectively, and the corresponding tunneling energy is $E_J = 0.729E_F \approx 11E_C$. 44

4.1 Population imbalance *vs.* phase difference at unitarity. The potential barrier has height $V_0 = 5E_F$ and width $d = 0.6k_F^{-1}$, as in Fig. 3.7. Solid lines are the results of time-dependent BdG simulations, while dashed lines are the solutions of the nonlinear Josephson equations (4.8) and (4.10), with $E_J = 0.0833E_F$ and $E_C = 0.0678E_F$ taken from the solutions of the stationary BdG equations. Closed trajectories correspond to Josephson oscillations with initial imbalance $|z_0| = 0.06$, while open trajectories correspond to self-trapped states with $|z_0| = 0.096$. 47

4.2 Population imbalance *vs.* phase difference at $1/(k_F a) = -0.5$. The potential barrier has height $V_0 = 5E_F$ and width $d = 0.6k_F^{-1}$. Solid lines are the results of time-dependent BdG simulations, while dashed lines are the solutions of the nonlinear Josephson equations (4.8) and (4.10), with $E_J = 0.083E_F$ and $E_C = 0.0812E_F$ taken from the solutions of the stationary BdG equations. Closed trajectories correspond to Josephson oscillations with initial imbalance $|z_0| = 0.05$, while open trajectories correspond to self-trapped states with $|z_0| = 0.1$. 48

4.3 Energy difference ΔE and maximum Josephson current I_J calculated with the BdG equations (solid lines) and the NLSE (dashed lines), as a function of the interaction strength $1/(k_F a)$. The parameters of the barrier are $d = 0.6k_F^{-1}$ and $V_0 = 5E_F$, and the number of atoms $N = 100$. 50

4.4 The phase diagrams for π-mode Josephson oscillation (region A), π-mode self-trapping (region B) and self-trapping (region C), when initial phase difference $\Phi_0 = \pi$. The red dashed line is the minimum initial population imbalance z_0 to investigate π-mode Josephson oscillation, while the blue solid line is the minimum z_0 to investigate π-mode self-trapping. 52

4.5 Evolutions of density $n(x,t)/n_0$, the phase of order parameter $\phi(x,t)/\pi$ and absolute value of order parameter $|\Delta(x,t)|/E_F$, obtained by solving the time-depend superfluid local density approximation equations (4.26). We use an offset potential $V_{\text{off}} = 1E_F$ and $d = 0.6k_F^{-1}$ to produce a locally low density in the middle of the box, then release it at $t = 0E_F/\hbar$. We could observe a sound wave travelling back and forth inside of the box, with speed approximately $0.35v_F$. 57

5.1 Dynamic structure factor, from BdG+RPA theory as a function of ω for fixed momentum transfer $q = 3k_F$ and for various interaction strength. Black solid lines (red dashed lines) refer to the density dynamic structure factor $S(q,\omega)$ (spin dynamic structure factor $S_S(q,\omega)$). The results almost coincide with those of [5]. The dynamic structure factor is given in units of N/E_F. 67

5.2 Comparison of theoretical and experimental results for the quantity $P(q,\omega)$ defined in 5.27 and measured by means of Bragg scattering. The LDA+RPA+BdG predictions (lines) agree reasonably well with the experimental data (empty squares) in the BCS-BEC crossover. The theoretical curves have no free parameters. The spectrum is normalized so that the area below the curve is unity. The frequency is measured in units of the recoil energy of the atoms. Taken from [6]. 68

5.3 The color-plot (left) shows the dynamic structure factor for momentum transfer q in the range from 0 to $2k_F$ obtained with RPA calculations based on SLDA. The slope of the low energy branch corresponds to the sound speed $c_s = 0.35v_F$, while the horizontal threshold at $\omega = 1.0E_F/\hbar$ is equal to the minimum energy 2Δ to break a Cooper-pair. The same $S(q, \omega)$ for $q01k_F$ is plotted in the right panel. 74

5.4 The phononic peak of the dynamic structure factor is shown in the low-q limit. The red solid line is the SLDA result and the black solid line is the BdG result. 75

5.5 Static structure factor of superfluid unitary fermions at zero temperature calculated by SLDA+RPA theory (blue solid line), compared with the results of Quantum Monte Carlo (black dotted line) [5] and BdG+RPA (red dashed line) theory. 76

5.6 Dynamic structure factor for a relatively large momentum transfer ($q = 4k_F$) calculated by both SLDA+PRA theory (red line) and BdG+RPA theory (black line). 76

6.1 Order parameter (squares), mean-field interaction energy (circles) and effective mass (diamonds) of a unitary Fermi gas at finite temperature calculated with a Quantum Monte Carlo technique in [7]. The solid, dotted, and dashed lines are the same quantities calculated within an independent quasiparticle model. Taken from [7]. 80

6.2 Chemical potential μ (red solid line) and order parameter Δ (blue solid line) as a function of temperature obtained with SLDA with T independent parameters α, β and γ. The dashed lines are the same quantities but in BdG theory. The experimental result for the chemical potential [8] is shown as the lowest long dashed line. The transition temperature T_c is $0.33T_F$ in SLDA and $0.5T_F$ in BdG. The SLDA curve of the chemical potential is much closer to the experimental data than BdG. 82

6.3 Chemical potential μ (red solid line) and order parameter Δ (blue solid line) as a function of temperature obtained with SLDA by using the parameters $\alpha = 1$, $\beta = -0.574$ and $1/\gamma = -0.193$. The MIT experimental results [8] are represented by the black dash line. . . . 83

6.4 The color-plot(left) exhibits the dynamic structure factor at temperature $T/T_F = 0.2, 0.3, 0.4$, for momentum transfer q ranged from $0k_F$ to $2k_F$. When the system is superfluid (the upper and middle two panels), a horizontal line is emergent when the energy transfer ω is equal to the minimum energy $2\Delta(T)$ to break a Cooper-pair at temperature T, while this horizontal line disappear if $T > T_c$ (the under two panels). The right panel is the dynamic structure factor at momentum transfer $q = 1k_F$, when will give a sudden jump when $\omega = 2\Delta(T)/\hbar$ if $T < T_c$. 84

6.5 Height of molecular peak in dynamic structure factor at $q = 4k_F$ and $\omega = \omega_r/2 \approx 6.86E_F/\hbar$ as a function of temperature. Left panel: SLDA+RPA (black solid line) and BdG+RPA (red dash line). Right panel: experimental data from Bragg scattering [9], in arbitrary units; the vertical line indicates the transition temperature T_c; the lowest dotted line is the prediction for an ideal Fermi gas. 86

Chapter 1

Introduction

1.1 Historical overview

The story of ultracold quantum gases began in 1924-1925, when Satyendra Nath Bose [10] and Albert Einstein [11] predicted that many bosonic particles can occupy the lowest single-particle energy state when the temperature is reduced below a critical value. This quantum phenomenon is named Bose-Einstein condensation. Usually, normal atomic gases would become liquid and then solid before forming a Bose-Einstein condensate (BEC), at low temperature. However, if a sample of atomic gas has a low enough density to prevent three-body recombination, the gas will stay in a metastable state for a long enough time when cooling the system to a critical temperature, and one can investigate the condensate. In this case, the typical density is of the order of 10^{14} particles/cm^3 and the temperature tens to hundreds of nano-kelvin, where the thermal wavelength $\lambda_T = \sqrt{2\pi\hbar^2/(mk_BT)}$ becomes comparable to the interatomic distances in the atomic gases.

Experimentally, it is quite hard to cool quantum gases to such a low temperature. Seventy years after the theoretical prediction of Bose and Einstein, thanks to the development of new cooling techniques (laser cooling and evaporative cooling) for atoms in magnetic traps, in 1995, the first Bose-Einstein condensate was observed in laboratories at JILA [12] and MIT [13] with bosonic gases of ^{87}Rb and ^{23}Na, respectively. A new field of research started from these experiments.

Also Fermi gases can be trapped in magnetic fields and cooled to low temperature with laser cooling techniques. The main difference with bosonic gases is the effect of collisional processes, which are essential in the evaporative cooling. At low density and temperature the interaction between atoms is dominated by s-wave collisions and the only relevant interaction parameter is the s-wave scattering length a. However, in a single-component Fermi gas, this s-wave contact interaction is inhibited by the Pauli exclusion principle, which causes dramatic consequences on the cooling mechanism. This has made the achievement of degenerate atomic Fermi gases a difficult goal, which was ultimately overcome by the use of sympathetic cooling technique, either employing two different spin components of the same Fermi gases or adding a Bose gas component as a refrigerant. In 1999, a group at JILA firstly observed the degenerate Fermi gas in laboratories [14] with two spin components of ^{40}K. Later quantum degeneracy effects were observed in ^{6}Li with sympathetic cooling between ^{6}Li and bosonic ^{7}Li isotope [15, 16]. The cooling technique of fermions using different bosonic species has also proven efficient as, for instance, in the case of ^{40}K-^{87}Rb [17] as well as ^{6}Li-^{23}Na [18].

In the last two decades ultracold gases have been a very "hot" topic, attracting the attention of many experimental and theoretical groups in an interdisciplinary context. One of the important properties of these systems is that the interaction between atoms can be adjusted almost at will by using Fano-Feshbach resonances [19]. This phenomenon was originally found in the scattering cross section of neutrons in nuclei and turns out to be particularly effective for atomic gases. In fact, by tuning the intensity of an external static magnetic field, the s-wave scattering length can be continuously changed from small negative a (attraction) to small positive a (repulsion) crossing a singularity where a is infinite. In the cases of fermions this corresponds to a transition from a weakly interacting Fermi superfluid in the Bardeen-Cooper-Schrieffer state (BCS) to a state of weakly repulsive condensate of molecules (BEC). The intermediate regime is called BCS-BEC crossover. In particular, at the resonance, when a diverges, the gas of fermions is in the "unitary" regime and manifests universal properties, where the macroscopic observables become completely independent of the interatomic potential [20, 21, 22]. This regime is difficult to obtain with bosons because of the atom losses caused by 3-body collisions when a increases, but this effect is inhibited in fermions due to Pauli exclusion principle. In 2002, the unitary Fermi gases were firstly realized at Duke experiment group [23].

An appealing feature of ultracold gases is that they are very pure and clean, and one can use laser beams and magnetic field to manipulate them and confine them in different geometries, including periodic lattice structures (optical lattice) [24]. One can also change the dimensionality of systems to observe low-dimension physics. The easy manipulation with external fields allows one to create and observe excited states, collective motions, transport phenomena, quantized vortices, solitons, shock waves, and many other dynamical properties.

On the theoretical side, since at present an exact solution of the many-body problem along the whole BCS-BEC crossover is not available, one has to resort to approximation schemes or numerical simulations. Theoretical challenges in describing the BCS-BEC crossover arise from its strongly correlated nature: there is no small interaction parameter to set the accuracy of theories [25]. Significant progress has been made in developing better quantum Monte Carlo simulations [26, 27, 28, 29] and strong-coupling theories [25, 30, 31, 32, 33, 34]. Quantum Monte Carlo technique is believed to be able to provide quantitatively reliable results, but it suffers from the "sign problem" for fermions. At high temperature, the quantum cluster expansion has been proved to be an efficient method [35, 25, 36, 37, 38, 39, 40], but it cannot work at very low temperature because the small quantity, the fugacity $z \equiv \exp[\mu/(k_B T)]$, is no longer a well-defined small expansion parameter. A useful approximation is provided by the standard BCS mean-field theory of superconductivity [41]. The main merit of this approach is that it provides a comprehensive, although approximate, description of the equation of state along the whole crossover regime, including the unitary limit and the BEC regime of small and positive "a". This thesis will use this mean-field theory and its generalized version to investigate the dynamics of the superfluid Fermi gases at unitarity and in the BCS-BEC crossover.

1.2 Josephson effect in ultracold quantum gases

The Josephson effect [42, 43] is one of the key features of superconductors and superfluids. It is named after the British physicist Brian David Josephson, who predicted in 1962 the mathematical relationships between the current and voltage across a

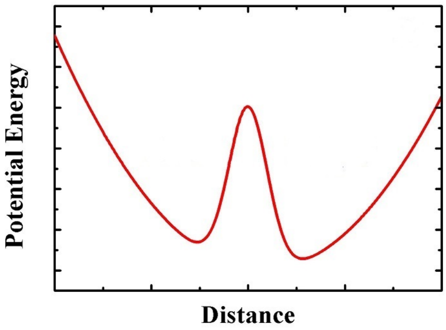

Figure 1.1: The Gaussian-shape double well potential. In experiments, laser beams and magnetic traps can be used to generate such external potential for the confinement of ultracold atoms.

weak link connecting two superconductors. It involves very fundamental properties and has important applications. Experimentally, a weak link may consist of a thin insulating barrier (known as a superconductor-insulator-superconductor junction, or S-I-S), a short section of non-superconducting metal (S-N-S), or a physical constriction that weakens the superconductivity at the point of contact (S-s-S). In typical solid state devices it is rather difficult or even impossible to adjust the relevant parameters of Josephson junctions. This difficulty is largely overcome in ultracold quantum gases.

The physics of the Josephson junctions can be effectively investigated with ultracold gases confined in a double well potential [44, 45, 46](see Fig. 1.1). Although initially the Josephson effect was introduced for the charged electrons, which are fermions, the first investigation of this effect in cold gases was done for weakly linked Bose-Einstein condensates (BEC).

In 1997 and 1999, A. Smerzi *et al.* [47, 48] employed the double well potential to investigate theoretically the Josephson effect in ultracold bosonic gases. They wrote coupled nonlinear Josephson equations for the relative population and the phase difference between the two wells. These equations were derived by assuming that the wave function of the system, governed by the Gross-Pitaevskii (GP) equation can be described as a superposition of left and right localized condensates. This idea is often called two-mode model[49, 50]. Such nonlinear Josephson equations admit four solutions, corresponding to four different dynamical regimes. When the initial phase difference is zero and the initial population imbalance is smaller than a critical value, one can observe small amplitude periodic oscillations, which are called Josephson oscillations, where the atoms just tunnel back and forth between the two wells, and whose period is determined by two key parameters: the mean-field (on-site) energy and the tunnelling energy. If the initial population imbalance is beyond this critical value, the system may exhibit self-trapped solutions (self-trapping) with the relative population oscillating around a nonzero value. When the initial phase difference is π, one finds another two dynamical regimes: π-mode Josephson oscillations and π-mode self-trapping, where both the time-averaged quantum phase difference across the junction equals π, but time-averaged population imbalance is zero and nonzero, respectively. In order to observer the π mode, the ratio between on-site energy and tunnelling energy is required to be smaller than a certain value. A large number of theoretical papers have been published along this line and experiments have also been performed [46, 51, 52, 1, 53, 54, 55]. In 2001, F. S. Cataliotti *et al.* [51] reported on the direct observation of an oscillating atomic current in a one-dimensional array of Josephson junctions realized with an atomic Bose-Einstein condensate. In 2004, Th. Anker *et al* [52] reported the first experimental observation of nonlinear self-trapping of Bose-condensed ^{87}Rb atoms in a one-dimensional waveguide with a superimposed deep periodic potential. In 2005, M. Albiez *et al.* [1] reported the first realization of a single bosonic Josephson junction, implemented by two weakly linked Bose-Einstein condensates in a double-well potential. Clear examples of Josephson oscillations and self-trapping are shown in Fig. 1.2. In 2010, Tilman Zibold *et al* [53] reported the π mode in a rubidium spinor Bose-Einstein condensate.

These four dynamical regimes are found in bosons. It is very interesting to check whether they exist also in Fermi gases. However, much less is known about Josephson effects in dilute Fermi gases. The Bogoliubov-de Gennes (BdG) equations for a two-component superfluid in the crossover from the Bardeen-Cooper-Schrieffer (BCS) phase to BEC were used in Ref. [4, 56] to describe a stationary supercurrent flowing in the presence of a three-dimensional barrier with a slab geometry; the current-phase relation and the critical current were studied in the crossover for

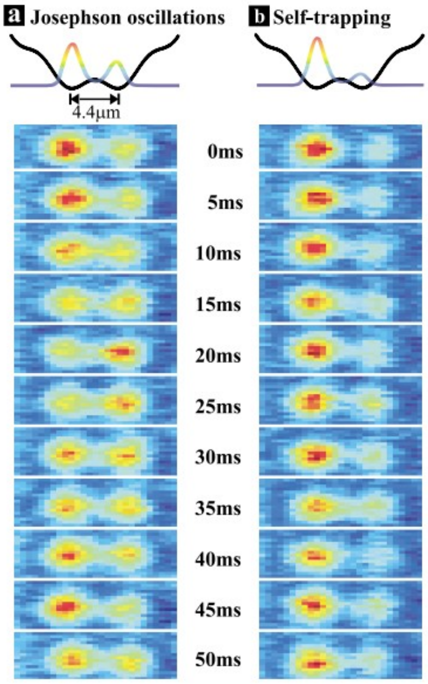

Figure 1.2: Absorption images of a ^{87}Rb condensate confined in a double-well potential from Josephson oscillations (left) to self-trapping (right). In the Josephson regime the atoms tunnel back and forth between the two wells, while in the self-trapping regime more atoms always remain in the left well. Taken from Michael Albiez *et al* [1].

relatively low barriers, i.e., the height of the barrier is smaller than the chemical potential of the superfluid. The same problem was also investigated by means of a density functional approach describing bosonic Cooper pairs [57]; the equation of state of the gas was included via a suitable parametrization and the order parameter of the superfluid was obtained as the solution of a nonlinear Schrödinger equation (NLSE). This method gives results in good agreement with the BdG results of Ref. [4, 56] from unitarity to the BEC limit. For a double well potential in the weakly linked limit (i.e., large barriers) the same density functional can be used to derive coupled nonlinear equations for the relative population and the phase difference analog to those for BECs [58, 59]. A similar NLSE has been used to discuss in detail the transition from Josephson oscillations to self-trapping [60].

Some open issues are worth considering. First, the applicability of a two-mode model to weakly linked dilute Fermi superfluids has been tested so far only within a density functional approach describing a gas of bosonic pairs (namely Cooper pairs, which become molecules in the BEC limit); being a generalization of the GP equation, the theory naturally reduces to the two-mode model under the same assumptions as for coupled BECs. It is thus interesting to test the two-mode model also within a more microscopic theory like BdG which includes fermionic degrees of freedom. Second, the available BdG calculations [4, 56] and their comparison with the density functional results [57] are limited to the case of a stationary current through a low and thick barrier, where the flow is almost hydrodynamic and a local density approximation can be applied [61]; time-dependent simulations with higher and thinner barriers can provide a more stringent and informative test. Finally, the stationary BdG equations does not include bosonic collective modes (e.g., phonons) in the spectrum of excitations and cannot address the problem of dynamical instabilities, soliton nucleation, phase slips, etc., which may occur in a superfluid flow in the presence of a potential barrier. This type of physics can instead be addressed by time-dependent BdG simulations.

The predictions of Bogoliubov-de Gennes theory are known to have limited accuracy. For instance, the chemical potential μ and gap order parameter Δ given by BdG in a uniform gas of unitarity are about 40% different from experimental values or quantum Monte Carlo simulations. Based on density functional theory, A. Bulgac *et al.* developed a generalized BdG theory for superfluid Fermi gases, which is named Superfluid Local Density Approximation (SLDA) [62, 63, 64], which includes the zero temperature value of μ and Δ from experiments or quantum Monte Carlo simulations as two input parameters. This theory is expected to be more accurate than BdG of unitarity, and its time-dependent version, TDSLDA, can be used to investigate the dynamical properties.

In the first part of this thesis, we will study the Josephson effect by using TDBdG equations, NLSE, the two-mode model, as well as TDSLDA.

1.3 Dynamic structure factor

In the second part of the thesis we will investigate the dynamic structure factor of superfluid fermions. The dynamic structure factor is a very important quantity, which contains information on the dynamical properties of a man body system, both at low energy (collective modes) and high energy (single-particle excitations). Experimentally, the dynamic structure factor can be measured via two-photon Bragg scattering [65, 2, 66] where two slightly detuned laser beams are impinged upon the trapped gas. The difference in the wave vectors of the beams defines the momentum transfer q, while the frequency difference defines the energy transfer $\hbar\omega$. The atoms exposed to these beams can undergo a stimulated light scattering event by absorbing a photon from one of the beams and emitting a photon into the other.

Essentially, the dynamic structure factor is the Fourier transform of the density-density correlation functions at two different space-time points [67, 68]. For a two-component atomic Fermi gases with equal spin populations $N/2$ (referred to as spin-up, $\sigma =\uparrow$, and spin-down $\sigma =\downarrow$), the density (spin) dynamic structure factor is defined as

$$S_{D(S)}(q,\omega) = 2\left[S_{\uparrow\uparrow}(q,\omega) \pm S_{\uparrow\downarrow}(q,\omega)\right] \tag{1.1}$$

where we have $S_{\uparrow\uparrow}(q,\omega) = S_{\downarrow\downarrow}(q,\omega)$ and $S_{\uparrow\downarrow}(q,\omega) = S_{\downarrow\uparrow}(q,\omega)$, and the components are given by

$$S_{\sigma\sigma'}(q,\omega) = Q^{-1}\sum_{nn'} e^{-\beta E_{n'}} \langle n|\delta\rho_\sigma(q)|n'\rangle \times \left\langle n' \middle| \delta\rho^\dagger_{\sigma'}(q) \middle| n \right\rangle \delta(\hbar\omega - E_{nn'}) \tag{1.2}$$

where $|n\rangle$ and $E_{nn'} = E_n - E_{n'}$ are, respectively, the eigenstate and eigenvalue of the many-body system, while $Q = \sum_n \exp(-\beta \mathrm{E_n})$ is the partition function and $\beta = 1/(k_B T)$ is the inverse temperature. The density operator $\delta\hat{\rho}_\sigma(q) = \sum_{i\sigma} e^{-i\mathbf{q}\cdot\mathbf{r}_i}$ is the Fourier transform of the atomic density operator $\delta\hat{\rho}_\sigma(\mathbf{r})$ for spin-σ atoms. In the following, for simplicity, we just use $S(q,\omega)$ for density dynamic structure factor and for spin dynamic structure factor, $S_S(q,\omega)$. Theoretically, linear response theory can be used to calculate the dynamic structure factor, which is related to the imaginary part of response function via the fluctuation-dissipation theorem.

At high momentum transfer, the dynamic structure factor is characterized by a quasi-elastic peak at $\omega = \hbar q^2/2M$, where M is the mass of the elementary constituents of the system. In the whole crossover, the density dynamic structure factor of superfluid fermions is characterized by a two-peak structure [5, 2, 69], while the spin dynamic structure has only one peak [66]. Figure 1.3 shows the first experimental result of density dynamic structure factor for strongly interacting fermions, done by Swinburne experimental group [2]. The position of the peak is expected to depend on whether photons scatter from free atoms ($M = m$) or molecules ($M = 2m$). The density dynamic structure factor has both of them, but the spin

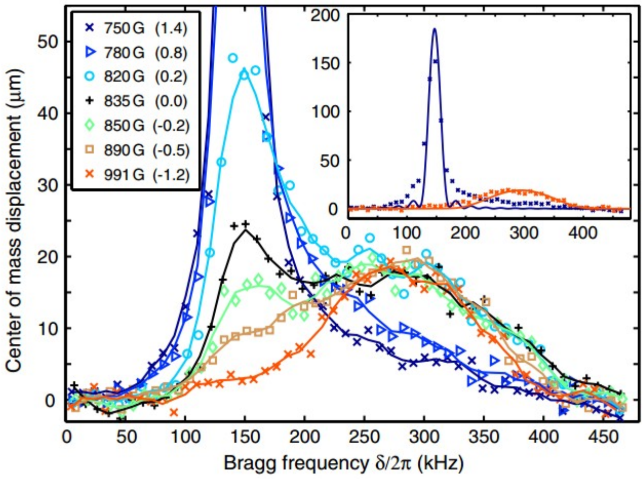

Figure 1.3: Bragg spectra showing density dynamic structure factor $S(q, \omega)$ for trapped Fermi gases across the BCS-BEC crossover. Magnetic field and $1/(k_F a)$ for each spectrum are given in the legend. The inset shows the 750 and 991 G spectra along with the calculated $S(q, \omega)$ for an ideal Fermi gases and molecular BEC at 750G. Taken from G. Veeravalli *et al* [2].

dynamic structure factor has only the molecular peak. Their occurrence depends on the actual value of the momentum transfer. If q is much larger than the inverse of the molecular size, photons mainly scatter from atoms and the quasi-elastic peak takes place at $\omega = \hbar q^2/2m$. In the opposite case, photons scatter from molecules and the excitation strength is concentrated at $\omega = \hbar q^2/4m$. During the whole crossover, the signal of molecular peak in BEC regime is obviously stronger than that in BCS regime, which reflects the fact that there are more molecules (or Cooper pairs) in BEC regime.

The density dynamic structure factor satisfies various sum rules, which involve frequency moments defined by $\langle \omega^n \rangle \equiv \int_{-\infty}^{\infty} d\omega \; \omega^n S(q, \omega)$. For $n = 0$, $\langle \omega^0 \rangle$ is equal to the static structure factor $S(q)$, which is intimately connected to the universal Tan's contact $\mathcal{I}$ at high momentum transfer q [70, 71, 72]. The $n = 1$ moment is the well known longitudinal f-sum rule, $\langle \omega \rangle \equiv \int_{-\infty}^{\infty} d\omega \; \omega S(q, \omega) = q^2/(2m)$ which was derived by Czech physicist, Georg Placzek, in 1952 (p. 365 of Lifshitz an Pitaevskii(1980) [73]). Higher-order moments sum rules can also be derived in a similar manner. Such sum rules are very useful constraints in experimental studies since the data can be used to compute $\langle\omega^n\rangle$. They are also used to check the theoretical predictions.

Universality of strongly interacting fermions is a feature of great interest which manifests also in the dynamic structure factor [74]. For large energy transfer, $\omega \to \infty$, the spin-parallel and spin-antiparallel dynamic structure factors have, respectively, a tail of the form $\sim \pm\omega^{-5/2}$, decaying slower than the density dynamic structure factor $S(q,\omega)$ $(\omega^{-7/2})$. These universal behaviors have already been verified by Bragg spectroscopy [66] of ultracold atomic Fermi gases.

Recently, the Swinburne experiment group measured the density dynamic structure of unitary Fermi gas also at finite temperature [9], where no theoretical predictions are available. At zero temperature, a dynamical mean-field theory or Bogoliubov-de Gennes and random phase approximation were already used to calculate the dynamic structure factor in the whole crossover [5]. In particular, at high momentum transfer q, the predictions of this theory quantitatively agree well in the BEC-unitarity regime, and not so well in the BCS regime [6]. However at finite temperature, this method has fatal drawback at high temperature (above T_c), where instead of interacting normal gases, it describes a pure ideal Fermi gases without interaction, which is obviously wrong. Thank to the introducing the Hartree term inside the energy density functional, the superfluid local density approximation can describe an interacting normal Fermi gases, and can provide quantitatively reliable results for unitary superfluid Fermi gases at zero temperature, so it is interesting to use this theory to calculate the dynamic structure factor, especially to check its effect at finite temperature.

In this thesis, we will use the superfluid local density approximation to calculate the dynamic structure factor of unitary fermions at zero temperature first, and then expand this theory to finite temperature and check its effect on predicting the dynamic structure factor at finite temperature.

1.4 Thesis outline

Here we give a brief outline of the chapters of this thesis. In the chapter 2, we introduce the Bogoliubov-de Gennes equations and their time-dependent version, and use them to investigate stationary and dynamical properties of superfluid Fermi gases in a box. In chapter 3, we use the same theory to characterize the dynamic behaviour of the gas in a double-well potential. In chapter 4, we will discuss the same problem using Nonlinear Schrödinger equation (or generalized GP equations), the nonlinear Josephson equations and the Superfluid Local Density Approximation. The comparison between the results of different theories is discussed in details. In chapter 5, we introduce the linear response theory and the dynamic structure factor. We use the strategy of the Random Phase Approximation to calculate $S(q,\omega)$ with BdG theory and SLDA. In the chapter 6, we summarize the main results of our calculation of $S(q,\omega)$ at finite temperature and comment the comparison with experiment. Finally, we will present all conclusions and perspectives of the whole thesis in the chapter 7.

Chapter 2

Bogoliubov-de Gennes equations

Theoretical challenges in describing the crossover behaviour arise from its strongly correlated nature: there is no small interaction parameter to set the accuracy of theories [25]. A useful approximation is provided by the standard BCS mean-field theory of superconductivity. This approach was first introduced by Eagles(1968) [75] and Leggett(1980) [76] with the main motivation to explore the properties of superconductivity and superfluidity beyond the weak-coupling limit $k_F|a| \ll 1$. The main merit of this approach is that it provides a comprehensive, although approximation, description of the equation of state along the whole crossover regime, including the limit $1/(k_F a) \to 0$ and the BEC regime of small and positive a. In this part of thesis, we introduce the Bogoliubov-de Gennes (BdG) equations and their time-dependent version (TDBdG).

2.1 Derivation of BdG equations

For two-component Fermi gases with a s-wave contact interaction, the system can be described by the Hamiltonian

$$H = \sum_\sigma \int d\mathbf{r} \Psi^\dagger_\sigma(\mathbf{r})[-\frac{\hbar^2}{2m}\nabla^2 + V(\mathbf{r}) - \mu_\sigma]\Psi_\sigma(\mathbf{r}) + g\int d\mathbf{r}\Psi^\dagger_\uparrow(\mathbf{r})\Psi^\dagger_\downarrow(\mathbf{r})\Psi_\downarrow(\mathbf{r})\Psi_\uparrow(\mathbf{r}) \tag{2.1}$$

where the pseudospins $\sigma = \uparrow, \downarrow$ denote the two hyperfine states and $\Psi_\sigma(\mathbf{r})$ is the Fermi field operator that annihilates an atom at position $\mathbf{r}$ in the spin σ state. The number of total atoms is $N = N_\uparrow + N_\downarrow$. The quantities $\mu_{\uparrow,\downarrow}$ are the chemical potential of each spin states. The function $V(\mathbf{r})$ is the external potential and g is the bare interatomic interaction strength.

Starting from the Heisenberg equation of motion of Hamiltonian (2.1) for the field operators $\Psi_\uparrow(\mathbf{r}, t)$ and $\Psi_\downarrow(\mathbf{r}, t)$, one can obtain the following two equations:

$$\begin{aligned} i\hbar\frac{\partial\Psi_\uparrow}{\partial t} &= \left[-\frac{\hbar^2}{2m}\nabla^2 + V - \mu_\uparrow\right]\Psi_\uparrow + g\Psi_\downarrow^\dagger\Psi_\downarrow\Psi_\uparrow, \\ i\hbar\frac{\partial\Psi_\downarrow}{\partial t} &= \left[-\frac{\hbar^2}{2m}\nabla^2 + V - \mu_\downarrow\right]\Psi_\downarrow - g\Psi_\uparrow^\dagger\Psi_\downarrow\Psi_\uparrow. \end{aligned} \tag{2.2}$$

Within the mean-field approximation, the terms $g\Psi_\downarrow^\dagger\Psi_\downarrow\Psi_\uparrow$ and $g\Psi_\uparrow^\dagger\Psi_\downarrow\Psi_\uparrow$ are replaced with their respective mean-field approximations $g\Psi_\downarrow^\dagger\Psi_\downarrow\Psi_\uparrow = -\Delta(\mathbf{r})\Psi_\downarrow^\dagger + gn_\downarrow(\mathbf{r})\Psi_\uparrow$ and $g\Psi_\uparrow^\dagger\Psi_\downarrow\Psi_\uparrow = -\Delta(\mathbf{r})\Psi_\uparrow^\dagger - gn_\uparrow(\mathbf{r})\Psi_\downarrow$, where we define the order parameter (or gap function) $\Delta(\mathbf{r}) = -g\langle\Psi_\downarrow\Psi_\uparrow\rangle$ and the density $n_\sigma(\mathbf{r}) = \langle\Psi_\sigma^\dagger\Psi_\sigma\rangle$. The above decoupling thus leads to

$$\begin{aligned} i\hbar\frac{\partial\Psi_\uparrow}{\partial t} &= \left[\mathcal{H}_\uparrow^S - \mu_\uparrow\right]\Psi_\uparrow - \Delta(r)\Psi_\downarrow^\dagger, \\ i\hbar\frac{\partial\Psi_\downarrow}{\partial t} &= \left[\mathcal{H}_\downarrow^S - \mu_\downarrow\right]\Psi_\downarrow + \Delta(\mathbf{r})\Psi_\uparrow^\dagger. \end{aligned} \tag{2.3}$$

where $\mathcal{H}_\sigma^S = -\hbar^2\nabla^2/(2m) + V(\mathbf{r}) + gn_{\bar{\sigma}}(\mathbf{r})$ is the quasiparticle Hamiltonian of spin species σ. The equations of motion can be rewritten by using the standard stationary-state Bogoliubov transformations:

$$\begin{aligned} \Psi_\uparrow &= \sum_j \left[u_{j\uparrow}(\mathbf{r})c_{j\uparrow}e^{-iE_{j\uparrow}t/\hbar} + v_{j\downarrow}^*(\mathbf{r})c_{j\downarrow}^\dagger e^{iE_{j\downarrow}t/\hbar}\right], \\ \Psi_\downarrow^\dagger &= \sum_j \left[u_{j\downarrow}^*(\mathbf{r})c_{j\downarrow}^\dagger e^{iE_{j\downarrow}t/\hbar} - v_{j\uparrow}(\mathbf{r})c_{j\uparrow}e^{-iE_{j\uparrow}t/\hbar}\right]. \end{aligned} \tag{2.4}$$

These yield the well-known BdG equations for the Bogoliubov quasiparticle amplitudes $u_{j\sigma}(\mathbf{r})$ and $v_{j\sigma}(\mathbf{r})$ with excitation energies $E_{j\sigma}$,

$$\begin{bmatrix} \mathcal{H}_\sigma^S - \mu_\sigma & \Delta(\mathbf{r}) \\ \Delta^*(\mathbf{r}) & -\mathcal{H}_{\bar{\sigma}}^S + \mu_{\bar{\sigma}} \end{bmatrix} \begin{bmatrix} u_{j\sigma}(\mathbf{r}) \\ v_{j\sigma}(\mathbf{r}) \end{bmatrix} = E_{j\sigma} \begin{bmatrix} u_{j\sigma}(\mathbf{r}) \\ v_{j\sigma}(\mathbf{r}) \end{bmatrix} \tag{2.5}$$

where $u_{j\sigma}(\mathbf{r})$ and $v_{j\sigma}(\mathbf{r})$ are normalized by $\int d\mathbf{r}(|u_{j\sigma}(\mathbf{r})|^2+|v_{j\sigma}(\mathbf{r})|^2) = 1$. The density and the order parameter can then be written as

$$\begin{aligned} n_\sigma(\mathbf{r}) &= \frac{1}{2}\sum_j \left[|u_{j\sigma}|^2 f(E_{j\sigma}) + |v_{j\bar{\sigma}}|^2 f(-E_{j\bar{\sigma}})\right], \\ \Delta(\mathbf{r}) &= \frac{g}{2}\sum_j \left[u_{j\uparrow}v^*_{j\uparrow} f(E_{j\uparrow}) - u_{j\downarrow}v^*_{j\downarrow} f(-E_{j\downarrow})\right]. \end{aligned} \tag{2.6}$$

where $f(x) = 1/(e^{x/k_BT} + 1)$ is the Fermi-Dirac distribution function of quasiparticles, and the statistical average $\langle c^\dagger_{j\sigma} c_{j\sigma}\rangle = f(E_{j\sigma})$ and $\langle c_{j\sigma} c^\dagger_{j\sigma}\rangle = f(-E_{j\sigma})$ have been used. The solutions of the BdG equations contain both positive and negative excitation energies. Thus, to avoid double counting, a factor of 1/2 appears in the summation in Eqs.(2.6). One can easily identify that there is a one-to-one correspondence between the solution for the spin-up and spin-down energy levels. For example,

$$E_{j\sigma} \leftrightarrow -E_{j\bar{\sigma}} \tag{2.7}$$

and

$$\begin{bmatrix} u_{j\sigma}(\mathbf{r}) \\ v_{j\sigma}(\mathbf{r}) \end{bmatrix} \leftrightarrow \begin{bmatrix} -v^*_{j\bar{\sigma}}(\mathbf{r}) \\ +u^*_{j\bar{\sigma}}(\mathbf{r}) \end{bmatrix}. \tag{2.8}$$

By exploiting this symmetry of the BdG equations, we only need to solve the BdG equations for the spin-up part. This has the following form after removing the spin index; i.e., we let $u_j = u_{j\uparrow}$,$v_j = v_{j\uparrow}$ and $E_j = E_{j\uparrow}$, to give

$$\begin{bmatrix} \mathcal{H}^S_\uparrow - \mu_\uparrow & \Delta(\mathbf{r}) \\ \Delta^*(\mathbf{r}) & -\mathcal{H}^S_\downarrow + \mu_\downarrow \end{bmatrix} \begin{bmatrix} u_j(\mathbf{r}) \\ v_j(\mathbf{r}) \end{bmatrix} = E_j \begin{bmatrix} u_j(\mathbf{r}) \\ v_j(\mathbf{r}) \end{bmatrix}. \tag{2.9}$$

Also, we can write simplified expressions for density $n_\sigma(\mathbf{r})$ and order parameter $\Delta(\mathbf{r})$:

$$n_\uparrow(\mathbf{r}) = \textstyle\sum_j |u_j|^2 f(E_j), \quad n_\downarrow(\mathbf{r}) = \sum_j |v_j|^2 f(-E_j), \quad \Delta(\mathbf{r}) = g\sum_j u_j v^*_j f(E_j). \tag{2.10}$$

One should pay attention to the order parameter $\Delta(\mathbf{r})$ because $\sum_j u_j v^*_j$ diverges when using a contact interaction. This would lead to an unphysical ultraviolet divergence and requires a regularization that expresses the bare parameter g in terms of the observed or renormalized value $(4\pi\hbar^2 a/m)^{-1}$. To this purpose, one can write [76, 77, 41]

$$\frac{1}{g} = \frac{m}{4\pi\hbar^2 a} - \sum_k \frac{1}{2\epsilon_k} \tag{2.11}$$

where a is the s-wave scattering length between atoms with different spin and $\epsilon_k = \hbar^2 k^2/(2m)$. Generally, this regularization requires an infinitely small bare parameter g $(g \to 0)$, in order to compensate the ultraviolet divergence in the summation $\Sigma_k 1/(2\epsilon_k)$. At the same time, this small bare parameter g does great influence in the existence of Hartree term $(gn_{\bar{\sigma}})$ in the quasiparticle Hamiltonian $\mathcal{H}_\sigma^S = -\hbar^2\nabla^2/(2m) + V(\mathbf{r}) + gn_{\bar{\sigma}}(\mathbf{r})$.

For weak couplings, one may indeed obtain Hartree terms like $(4\pi\hbar^2 a/m)n_\sigma$. With regularization, these corrections are beyond mean field and are effective only in the deep BCS limit. Towards the unitarity limit with increasing scattering length, they are no longer the leading corrections and become even divergent. Higher-order terms are needed in order to remove the divergence at unitarity. For example, one may use Páde approximations in the equation of state [20]. Thus, in the BCS-BEC crossover region, neglecting the Hartree terms is not an unreasonable approximation. Since the density $n_{\uparrow,\downarrow}$ are convergent, the Hartree term gives almost no contribution to the quasiparticle Hamiltonian. Therefore, strictly speaking, within a mean-field approximation the Hartree term (gn_σ) *should* vanish identically.

After throwing away the Hartree term $gn_\sigma(\mathbf{r})$ inside $\mathcal{H}_{\bar{\sigma}}^S$, we have $\mathcal{H}_\uparrow^S = \mathcal{H}_\downarrow^S \equiv \mathcal{H}_0 = -\hbar^2\nabla^2/(2m) + V(\mathbf{r})$. For equally populated components $(N_\uparrow = N_\downarrow)$, the chemical potential of fermions in different spin states should be equal, $\mu_\uparrow = \mu_\downarrow \equiv \mu$. Finally, we get the stationary BdG equations.

$$\begin{bmatrix} \mathcal{H}_0 - \mu & \Delta(\mathbf{r}) \\ \Delta^*(\mathbf{r}) & -\mathcal{H}_0 + \mu \end{bmatrix} \begin{bmatrix} u_j(\mathbf{r}) \\ v_j(\mathbf{r}) \end{bmatrix} = E_j \begin{bmatrix} u_j(\mathbf{r}) \\ v_j(\mathbf{r}) \end{bmatrix} \tag{2.12}$$

which need to be self-consistently solved together with the equations of density and order parameter. In the particular case of a homogeneous gas, $u_j(\mathbf{r})$ and $v_j(\mathbf{r})$ can be expanded with plane wave functions, e.g., $u_j(\mathbf{r}) \to u_k e^{i\mathbf{kr}}$ and $v_j(\mathbf{r}) \to v_k e^{i\mathbf{kr}}$. Thus the stationary BdG equations will gives two branches of solutions with

$$\begin{array}{rlrl} E_k^+ = E_k = \sqrt{\xi_k^2+\Delta^2}, & & E_k^- = -E_k = -\sqrt{\xi_k^2+\Delta^2}. \\ |u_k|^2 = \frac{1}{2}\left(1+\frac{\xi_k}{E_k}\right), & & |u_k|^2 = \frac{1}{2}\left(1-\frac{\xi_k}{E_k}\right). \\ |v_k|^2 = \frac{1}{2}\left(1-\frac{\xi_k}{E_k}\right), & & |v_k|^2 = \frac{1}{2}\left(1+\frac{\xi_k}{E_k}\right). \\ u_k v_k^* = \frac{\Delta}{2E_k}, & & u_k v_k^* = -\frac{\Delta}{2E_k}. \end{array} \tag{2.13}$$

where $\xi_k = \hbar^2 k^2/(2m) - \mu$.

If we repeat the same derivation but with dynamical Bogoliubov transformations

$$\begin{aligned} \Psi_\uparrow &= \sum_j \left[u_{j\uparrow}(\mathbf{r},t)c_{j\uparrow} + v_{j\downarrow}^*(\mathbf{r},t)c_{j\downarrow}^\dagger\right], \\ \Psi_\downarrow^\dagger &= \sum_j \left[u_{j\downarrow}^*(\mathbf{r},t)c_{j\downarrow}^\dagger - v_{j\uparrow}(\mathbf{r},t)c_{j\uparrow}\right], \end{aligned} \tag{2.14}$$

we obtain the time-dependent Bogoliubov-de Gennes equations

$$\begin{bmatrix} \mathcal{H}_0-\mu & \Delta(\mathbf{r},t) \\ \Delta^*(\mathbf{r},t) & -\mathcal{H}_0+\mu \end{bmatrix} \begin{bmatrix} u_j(\mathbf{r},t) \\ v_j(\mathbf{r},t) \end{bmatrix} = i\hbar\frac{\partial}{\partial t}\begin{bmatrix} u_j(\mathbf{r},t) \\ v_j(\mathbf{r},t) \end{bmatrix}. \tag{2.15}$$

In the following, we solve stationary BdG equations to calculate all static physical quantities as, for instance, the grand canonical energy $E = \langle \hat{H} - \mu\hat{N}\rangle$ of the system at zero temperature:

$$E = \int d\mathbf{r} \sum_j \left[2(\mu - E_j)|v_j(\mathbf{r})|^2 + \Delta^*(\mathbf{r})u_j(\mathbf{r})v_j^*(\mathbf{r})\right]. \tag{2.16}$$

We also solve the TDBdG equations by means of a 4th order Runge Kutta algorithm in order to simulate dynamic processes.

2.2 BdG equations for uniform system in a box

Actual simulations are performed in a finite computational box. In our case we use a three-dimensional rectangular box of size $L \times L_\perp^2$. A discrete basis set is needed to describe all quasiparticle amplitudes. The basis set contains a finite number of functions whose energies are limited by an energy cutoff E_{cut}. The value of E_{cut}

has to be large enough to avoid the dependence of results on it. Accordingly, the regularization equation (2.11) can be rewritten as

$$\frac{1}{k_F a} = \frac{8\pi E_F}{g k_F^3} + \frac{2}{\pi}\sqrt{\frac{E_{cut}}{E_F}} \tag{2.17}$$

while $E_F = \hbar^2 k_F^2/(2m)$ and $k_F = (3\pi^2 n_0)^{1/3}$ are the Fermi energy and wave vector of a uniform ideal Fermi gas with bulk density n_0.

However, when calculating the energy (2.16), one finds that the convergence to a cutoff independent value is typically quite slow [78]. Two methods can be used to overcome this problem: hybrid BdG technique where the local density approximation may be adopted for sufficiently high-lying states [79, 80], or an improved regularization procedure [81] developed by A. Bulgac and Y. Yu. In this thesis, we use the second technique: for a given external potential $V(\mathbf{r})$ and chemical potential μ, we define a local Fermi wave vector $k_F(\mathbf{r})$ from the relation $\mu = \hbar^2 k_F(\mathbf{r})^2/(2m) + V(\mathbf{r})$ and a local cutoff wave vector $k_{\text{cut}}(\mathbf{r})$ from $E_{\text{cut}} = \hbar^2 k_{\text{cut}}^2/(2m) + V(\mathbf{r}) - \mu$. The regularization of the interaction consists of replacing the bare interaction strength g, in the expression of order parameter $\Delta(\mathbf{r})$ with a local effective $g_{\text{eff}}(\mathbf{r})$ given by

$$\frac{1}{g_{\text{eff}}(\mathbf{r})} = \frac{m}{4\pi\hbar^2 a} - \frac{m k_{\text{cut}}(\mathbf{r})}{2\pi^2\hbar^2}\left[1 - \frac{k_F(\mathbf{r})}{2k_{\text{cut}}(\mathbf{r})}\ln\frac{k_{\text{cut}}(\mathbf{r}) + k_F(\mathbf{r})}{k_{\text{cut}}(\mathbf{r}) - k_F(\mathbf{r})}\right]. \tag{2.18}$$

In the following, we focus on Fermi gases at zero temperature ($T = 0$), where the total density $n(\mathbf{r}) = n_\uparrow(\mathbf{r}) + n_\downarrow(\mathbf{r})$ and the order parameter $\Delta(\mathbf{r})$ are calculated with equation $n(\mathbf{r}) = 2\sum_j |v_j(\mathbf{r})|^2$ and $\Delta(\mathbf{r}) = \sum_j g_{\text{eff}}(\mathbf{r}) u_j(\mathbf{r}) v_j^*(\mathbf{r})$, respectively, and all summations are restricted to the interval $0 \leq E_j \leq E_{\text{cut}}$. The system is contained in a box with transverse size $L_\perp$ and longitudinal size L. In the rest of this chapters, as a test case for the numerical solutions of the BdG and TDBdG equations, we consider the case $V(\mathbf{r}) = 0$ everywhere in the box with infinite hard walls at the boundaries. It is also convenient to exploit the symmetry of the system to distinguish solutions (and quasiparticle amplitudes) which are symmetric or anti-symmetric under spatial reflection $x \to -x$, with $x = 0$ as the center of the box.

The symmetric solution corresponds to the ground state, solution exhibiting a 0 phase jump at $x = 0$ in the order parameter Δ when crossing the center of the box, while the order parameter of the anti-symmetric solution displays a π phase jump

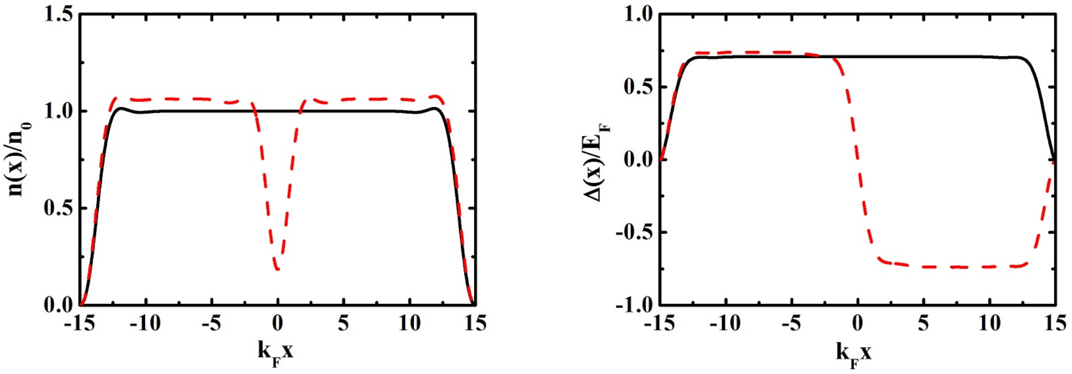

Figure 2.1: Density and order parameter of unitary fermions for the symmetric (solid lines) and anti-symmetric (dashed lines) solutions of the stationary BdG equations in a box of length $L = 30k_F^{-1}$ and $L_\perp = 13k_F^{-1}$. The particle number is $N = 156$ in both cases. The density n_0 is the ground state density in the center of the box.

$x = 0$. In both cases, the solution of the BdG equations provides the density $n(x)$, the order parameter $\Delta(x)$, the chemical potential μ and the energy E. We calculate the solutions by expanding quasiparticle amplitude u_k and v_k in the plane-wave basis. On such a basis, the left part of BdG equations is converted to a secular matrix. A matrix diagonalization then gives the desired quasiparticle energy spectrum and wave functions. Numerically we truncate the summation over the energy level. A improved regularization (2.18) is used to cure the ultraviolet divergence. Examples of symmetric state and anti-symmetric state with the same particle number N are shown in Fig. 2.1 for $L = 30k_F^{-1}$ and $L_\perp = 13k_F^{-1}$ and for a gas at unitarity.

This anti-symmetric state is the dark soliton solution of the BdG equations already calculated in Ref. [82]. The dark soliton exhibits a density depletion: particles are removed from the soliton region and displaced in the lateral regions, where the density becomes larger. Let us call E^+ and E^- the energy of the ground state and the anti-symmetric state, respectively. The difference $\Delta E = E^- - E^+$ is a measure of the cost in energy associated with the creation of the density depletion and the nodal structure of Δ at the box center.

Our results for the energies E^+ and E^- of unitary fermions as a function of $1/L$ are plotted in Figs. 2.2 and 2.3. Both energies must converge to the same asymptotic

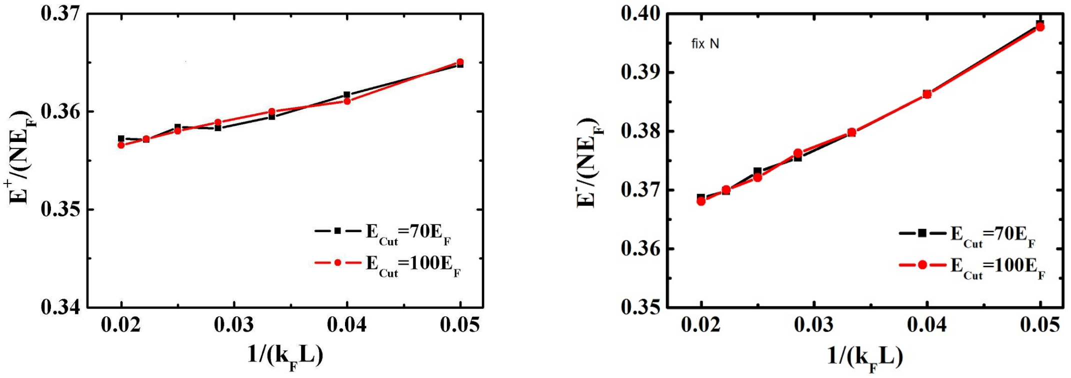

Figure 2.2: Energy per particle of the ground state (left) and the lowest anti-symmetric state (right) of unitary fermions in a box with periodic boundary conditions in the transverse direction and closed boundary conditions in the longitudinal direction. For each longitudinal length L, the two states have the same number of particles N. The number N, as a function of L, is such that the bulk density in the ground state is the same for all points. Energies are plotted as a function of $1/(k_F L)$. From a linear fit we extract the value in the $1/L \to 0$ limit, which is 0.351 and 0.348 for E^+/N and E^-/N, respectively. These values agree with the analytic BdG prediction $(3/5)(1+\beta) = 0.354$ for the ground state energy of a unitary gas. The remaining discrepancy, of the order of 1%, is due to numerical uncertainties induced by the finite cutoff energy, the discretization of the quasiparticles states in the transverse directions, and other sources of small numerical fluctuations.

value in the limit of an infinite system, where the soliton represents a vanishingly small perturbation on top of a uniform gas. The energy per particle of a uniform Fermi gas at unitarity, within the BdG theory, can be calculated analytically and the result is $E/N = (3/5)\mu$ with $\mu = (1+\beta)E_F$ and $\beta = -0.41$ [41]. Thus the two energies E^+/N and E^-/N must converge to the value $0.354E_F$ when $1/L \to 0$. Indeed the value extracted from a linear fit to both curves in Fig. 2.2 coincides with the analytic prediction within a statistical uncertainty of the order of 1%.

The increase of E^+/N, E^-/N with $1/L$ can be easily understood as due to the effect of the boundaries and, for the anti-symmetric state, of the soliton. Both the boundary and the soliton contribute to the energy with terms proportional

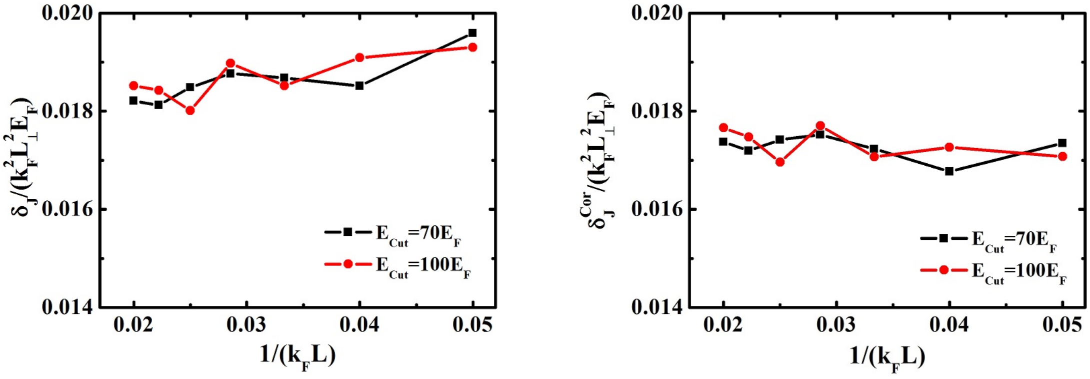

Figure 2.3: Left panel: energy difference $\Delta E = E^- - E^+$ per unit area, obtained from the energies plotted in Fig. 2.2. In the $(1/L) \to 0$ limit, the points should converge to the analytic BdG prediction $\epsilon_s = (1+\beta)^{1/2}/(8\pi\sqrt{3}) \simeq 0.0176$ [3] for the energy of a dark soliton in an infinite uniform gas. The value extracted from a linear fit to the data agree with this prediction within a 3% uncertainty. Right panel: soliton energy in the box as defined in Eq. (2.19). The $1/L \to 0$ limit is the same as in the left panel, but convergence is faster.

to the transverse area; given that N scales as the volume, their contributions to the energy per particle are inversely proportional to L and hence linear in $1/L$. Moreover, since the symmetric and anti-symmetric solutions almost coincide near the boundaries except for a phase difference, the contribution of the boundaries to the energy should cancel out when taking the difference. Therefore the energy difference ΔE divided by the transverse area is a direct measure of the soliton energy in the box, $\epsilon_s = \Delta E/(k_F^2 L_\perp^2 E_F)$. Our results are shown in the left panel of Fig. 2.3. In the limit of large boxes, this quantity must converge to the dark soliton energy in a uniform Fermi gas at unitarity. In the same limit the BdG theory provides the analytic value $\epsilon_s = (1+\beta)^{1/2}/(8\pi\sqrt{3}) \simeq 0.0176$ [3]. From a linear fit to our numerical results we indeed find the same value within a statistical error of the order of 3%. Notice that the relative uncertainty in ϵ_s is larger than the uncertainty in E^+ and E_- in Fig. 2.2, because ϵ_s is typically a small number obtained as a difference of two large numbers.

It is worth noticing that a faster convergence to the asymptotic soliton energy of the uniform gas can be obtained by properly accounting for finite size effects. In particular we notice that the soliton energy is usually defined as the difference between the energies of the states with and without soliton, sharing the same bulk density far away from the soliton itself. With this constraint, the solitonic solution has less particles in the soliton region than the ground state, since it exhibits a local density depletion. The difference ΔN is negative and corresponds to the particles which are "missing" at the soliton position. In our box, instead, we define ΔE from the energies of two solutions with the same N (see Fig. 2.1). This implies that the particles which are missing in the soliton remain in the box, in the regions between the boundaries and the soliton, thus the "bulk" densities of the two solutions are different and the chemical potentials are different as well. The leading correction to the soliton energy turns out to be proportional to $(\mu_N^- - \mu^+)\Delta N$, where μ^+ is the ground state chemical potential and μ_N^- is the chemical potential of the anti-symmetric solution with the same N, and we can write

$$\epsilon_s \simeq [\Delta E + (\mu_N^- - \mu^+)\Delta N]/k_F^2 L_\perp^2 E_F \ , \tag{2.19}$$

In the limit of an infinite box, we find $\Delta N \simeq -9.6$, while the difference of chemical potentials vanishes, so that the correction to ΔE can be neglected. For finite boxes, ΔN remains almost constant, while $(\mu_N^- - \mu^+)$ increases almost linearly. In the right panel of Fig. 2.3 we plot our results for the corrected ϵ_s. This quantity, as expected, is almost independent of L and close to the analytic prediction $\epsilon_s = 0.0176$, except for random numerical fluctuations.

These stationary solutions show that our method for the numerical solutions of the BdG equations works well in test cases where analytic results are available and we have also a good control on the numerical uncertainties.

2.3 Calculation of ΔE in the presence of a potential barrier

In this section, we calculate the energy difference, $\Delta E = E^- - E^+$, where E^+ is the energy of the (symmetric) ground state of the gas and E^- is the energy of the lowest anti-symmetric state with the same number of particles N in the box with a

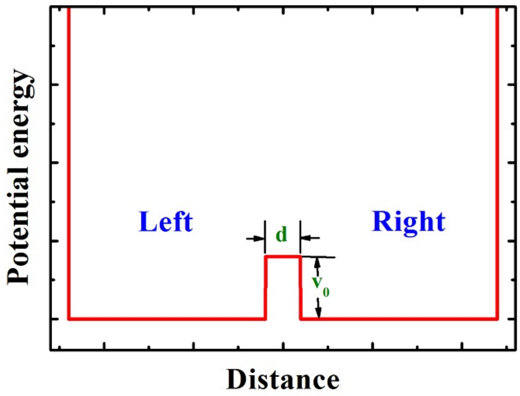

Figure 2.4: The rectangular-shape double well potential with a central barrier, whose width and height are d and V_0, respectively.

central barrier as in Fig. 2.4. Here symmetric and anti-symmetric refer to spatial reflection in the x-direction around $x = 0$. The anti-symmetric state corresponds to the solutions of Eqs. (2.12) exhibiting a π phase jump in the order parameter Δ when crossing the center of the box. For weakly coupled superfluids the quantity ΔE is directly related to the Josephson tunnelling energy, E_J, we will show later in section 3.2. Since the quantity ΔE is typically much smaller than the energies E^- and E^+, we must take care of all possible sources of numerical inaccuracy, in particular those introduced by the finite cutoff energy and the finite box.

Our results for ΔE as a function of V_0 and d are shown in Figs. 2.5 and 2.6. All results in these figures are obtained by using $N = 156$, $L_\perp = 13k_F^{-1}$, $L = 30k_F^{-1}$, and $E_{\text{cut}} = 70E_F$. As expected, ΔE approaches the same value in the limit of vanishingly small barrier (i.e, for $V_0 \to 0$ at finite d). This value is $\Delta E/(k_F^2 L_\perp^2 E_F) \simeq 0.0185$, which is slightly larger than the energy of dark soliton in an infinite system, due to the finite box size. For d of the order of k_F^{-1}, the quantity ΔE is rapidly decreasing when V_0 increases. The case of large barriers and small tunnelling (weak link) is where the physics of the Josephson effect is expected to manifest.

Finally we note that for V_0 much smaller than E_F the quantity ΔE tends to approach a constant value when $d \to \infty$. Typical density profiles and order param-

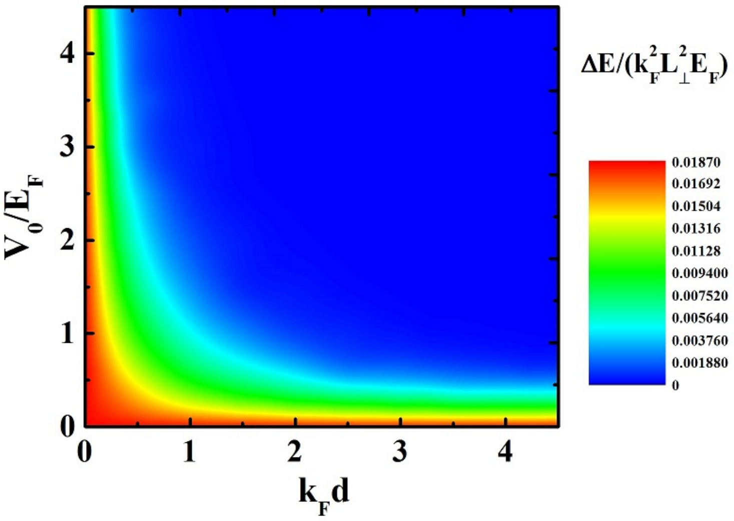

Figure 2.5: Energy difference $\Delta E = E^- - E^+$, divided by the area $L_\perp^2$, as a function of the barrier height V_0 and width d. Here $N = 156$, $L_\perp = 13k_F^{-1}$, $L = 30k_F^{-1}$, and $E_{\text{cut}} = 70E_F$.

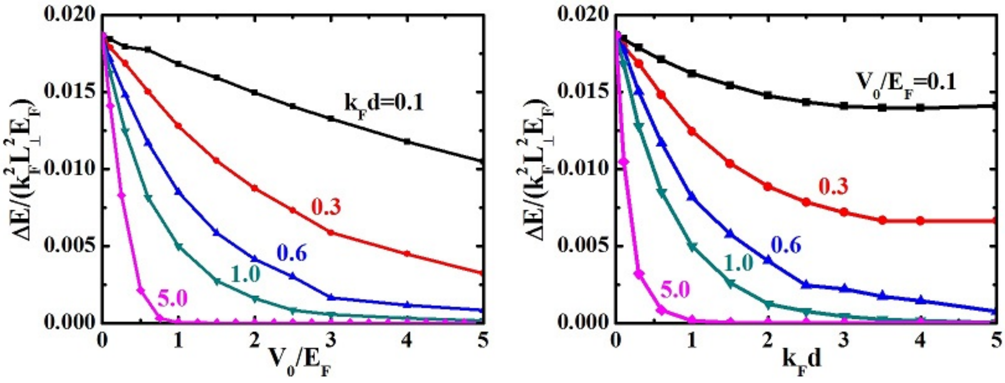

Figure 2.6: Left: energy difference $\Delta E = E^- - E^+$, divided by the area $L_\perp^2$, as a function of the barrier height V_0 for different widths d. Right: the same quantity as a function of the barrier width d for different values of height V_0. All the other parameters are the same as in the previous figure.

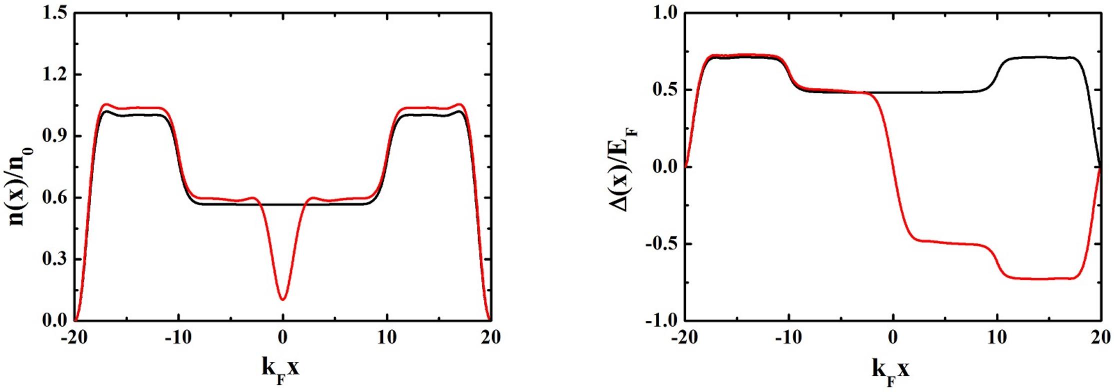

Figure 2.7: The density profile (left) and the order parameter profile (right) of the unitary fermions in a box, with a central barrier, whose height and width are $V_0 = 0.2E_F$ and $d = 20k_F^{-1}$, respectively. The black line is the ground state solution, while the red line is the anti-symmetric solution (or dark soliton solution). Both solutions have the same particle number $N = 164$.

eters of both symmetric and anti-symmetric system for such low and wide barrier are shown in Fig. 2.7. We notice that, in this case, the effect of the barrier is that of lowering the "bulk" density in the central region of the box. If d is larger than the soliton width, which is of the order of a few k_F^{-1}, this effect in ΔE can be accounted for by calculating the energy of a dark soliton in uniform gas of reduced density. Further increasing the width of the barrier has no effects on the soliton energy and hence ΔE remains constant.

2.4 TDBdG equations in a box

Time-dependent Bogoliubov-de Gennes equations is a powerful tool for investigating the dynamics of fermions. In order to solve the time-dependent BdG equations, we start from an initial input-state provided by stationary BdG equations, then we use a 4th order Runge Kutta algorithm to solve the TDBdG equations in real time. A proper time step must be chosen, large enough to produce fast simulations with reasonable computational effects, but not to large to cause instabilities in the

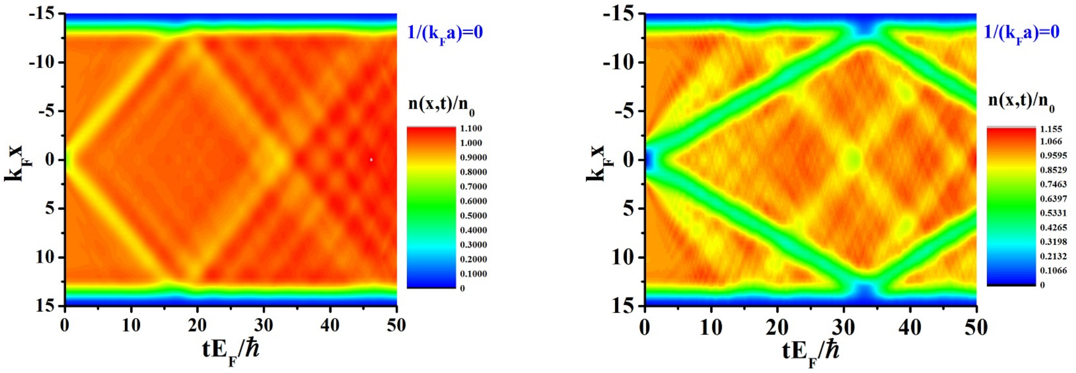

Figure 2.8: Left panel: sound wave-packets produced by an initial density perturbation in the center of the box and propagating back and forth in the uniform unitary gas. Right panel: same as before but for a stronger perturbation, at which, in addition to sound, generates also two dark solitons moving in opposite directions, slower than sound.

solutions. A standard recipe consists in taking the maximum time step is of the order of almost 10% of the inverse energy (E^+ or E^-) of the system divided by $\hbar$. In our simulation, the time step we use is of the order of $0.005\hbar/E_F$. In the following, we discuss four typical examples of simulations that we use to check the accuracy of the code.

First, we consider the propagation of sound waves. Initially, we introduce a rectangular barrier, whose height and width are $V_0 = 0.6E_F$ and $d = 0.6k_F^{-1}$, respectively, at the center of the box. The barrier produces a density depletion. Then we suddenly release this barrier and we follow the evolution of the gas. One can observe two sound wave-packets as in the left panel of Fig. 2.8, which are produced at the center and travel back and forth inside the box, with constant speed. This speed can be estimated by the slope of the yellow density depletion in our time-dependent simulation. From the above figure we obtain the value $c_s \approx 0.83E_F/(\hbar k_F) \approx 0.42v_F$, which is indeed rather close to the analytical predictions $c_s = \sqrt{(1+\beta)/3}v_F$ for a uniform gas at unitarity. Here $v_F = \hbar k_F/m$ is the Fermi velocity.

Secondly, we consider the coexistence of sound wave propagation and soliton propagation. We repeat the same operation as before but with a higher barrier ($V_0 =$

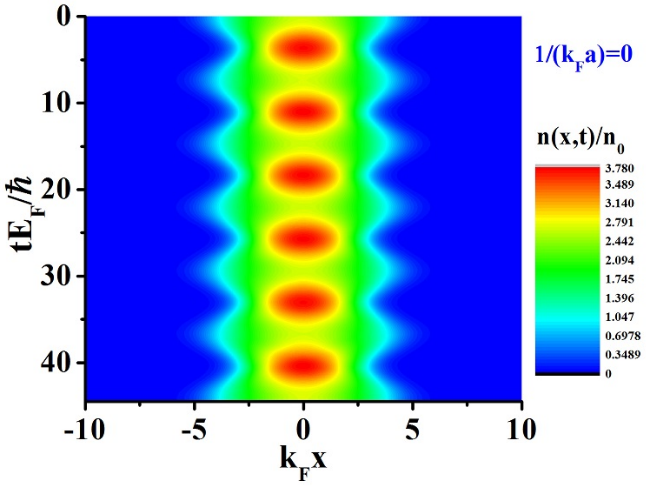

Figure 2.9: Breathing mode of unitary fermions in a harmonic trap $V_{\text{trap}} = m\omega_{\text{trap}}^2 x^2/2$. The frequency ω_{breath} of the trap is initially $0.4E_F/\hbar$, then suddenly changed to $0.5E_F/\hbar$. A breathing mode is generated, with frequency $\omega_{\text{breath}} = 0.86E_F/\hbar$.

$50E_F$), which depletes the central density to almost zero. By suddenly removing the barrier at $t = 0$, both sound wave-packets and grey solitons are produced at $x = 0$, propagating back and forth in the box (see the right panel of Fig. 2.8). The grey solitons correspond to the deeper density depletions propagating at slower velocity (smaller slope) than sound waves.

Thirdly, we consider a breathing mode in a harmonic potential. We put $N = 100$ atoms in a harmonic trap $V_{\text{trap}} = m\omega_{\text{trap}}^2 x^2/2$, whose trapping frequency is $\omega_{\text{trap}} = 0.4E_F/\hbar$, and then suddenly change the trapping frequency to $\omega_{\text{trap}}^{\text{fin}} = 0.5E_F/\hbar$. As shown in Fig. 2.9, the sudden change of the confining potential cause a periodic density oscillation, which is called breathing mode. In this simulation we obtain a period of oscillation $T_{\text{breath}} \approx 7.3\hbar/E_F$, and a corresponding frequency $\omega_{\text{breath}} = 2\pi/T_{\text{breath}} = 0.8607E_F/\hbar$. The ration between ω_{breath} and $\omega_{\text{trap}}^{\text{fin}}$ is 1.72, rather close to the prediction ($\omega_{\text{breath}}/\omega_{\text{trap}} = \sqrt{3}$) of the superfluid hydrodynamic equations for a unitary Fermi gas [83] in the same geometry.

Finally, we consider a soliton oscillation of unitary fermions in a harmonic trap

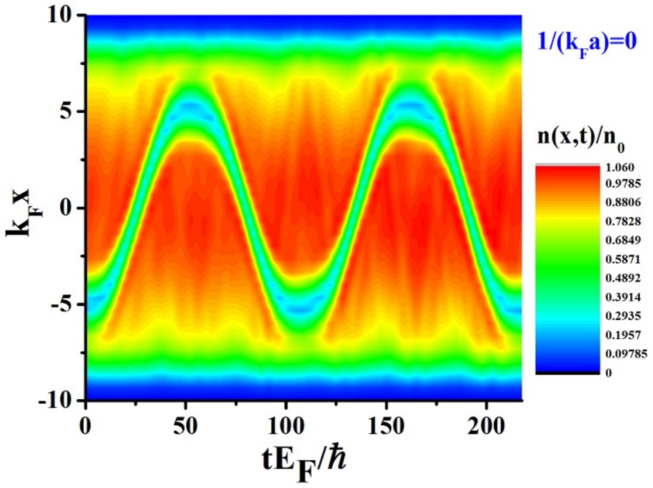

Figure 2.10: Soliton oscillation in a harmonic trap $V_{\text{trap}} = m\omega_{\text{trap}}^2 x^2/2$, with trapping period $T_{\text{trap}} = 2\pi/\omega_{\text{trap}} = 63\hbar/E_F$. The period of this oscillation is about $108\hbar/E_F \approx 1.71 T_{\text{trap}}$.

$V_{\text{trap}} = m\omega_{\text{trap}}^2 x^2/2$. We initially produce a dark soliton at position $x = -5k_F^{-1}$ as a particular solution of the stationary BdG equations and then solve the time-dependent BdG equations. The soliton begins to move towards the center of the trap with an increasing speed, reaching the maximum speed at the center, and then decreasing its velocity to zero at $x = 5k_F^{-1}$. After the soliton moves back and repeats the oscillation, as shown in Fig. 2.10. From the simulation in the figure we extract the period $T_s \approx 1.71 T_{\text{trap}}$, which turns out to be close to the prediction $T_s = \sqrt{3} T_{\text{trap}}$ [3], with $T_{\text{trap}} = 2\pi/\omega_{\text{trap}}$. The time-dependent BdG simulations of this soliton oscillation was first carried out by R. G. Scott [84].

These four dynamic solutions show that our method for the numerical interpretation of time-dependent BdG equations work well in test cases where analytical and/or numerical predictions already exist. We are thus ready to use it for novel configurations.

Chapter 3

Double wells and BdG equations

In this chapter, we use a double well potential to investigate the Josephson effect in ultracold Fermi gases. The double well is realized by simply adding a square potential barrier in the center of a rectangular box (see Fig. 3.1). The barrier has a variable height V_0 and width d, an offset potential V_{off} can help to produce the initial particle population imbalance. The square barrier is a convenient choice for computational reasons, but the main results of this work would not change by using barriers of different shape.

3.1 Josephson oscillations and self-trapping with TDBdG

Let us consider fermions at unitarity ($1/(k_F a) = 0$) in the presence of a thin ($d \sim k_F^{-1}$) and high ($V_0 > \mu$) square barrier centered at $x = 0$. We can define the number of atoms on the left, N_L, and right, N_R, as the integrals of the atom density $n(x)$ separately in the two regions of negative and positive x, respectively. The relative population imbalance can be defined as $z = (N_L - N_R)/N$, where $N = N_L + N_R$ is the total atom number. Another key quantity is the phase $\phi(x)$ of the complex order parameter $\Delta(x)$, which can also be different in the two wells. We define the right and left phases as $\phi_R = \phi(x = L/4)$ and $\phi_L = \phi(x = -L/4)$ respectively, and the phase difference as $\Phi = \phi_R - \phi_L$.

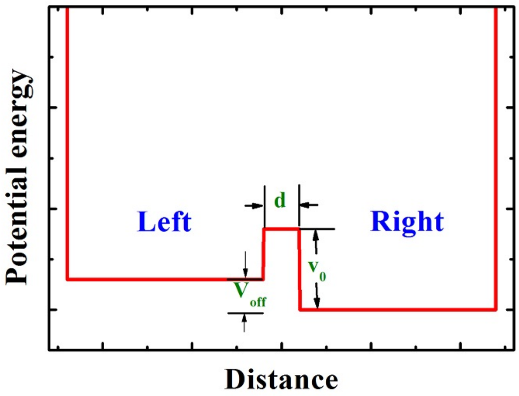

Figure 3.1: The rectangular-shape double well potential with a middle barrier, whose width and height is d and V_0, respectively. An offset potential V_{off} in the left helps to produce the initial population imbalance.

Our simulations start from an imbalanced configuration with $z_0 \equiv z(t=0) \neq 0$. This is obtained by first solving the stationary BdG equations (2.12) with a small constant offset potential V_{off} on the left side of the barrier. The ground state solution in such an asymmetric potential is then used as the initial ($t = 0$) state in the integration of the time-dependent BdG equations (2.15) in the symmetric double-well, after removing V_{off}. By solving the equilibrium condition of chemical potential, $\mu_L + V_{\text{off}} = \mu_R$, we find that z_0 and V_{off} have the relation $z_0 \approx 0.75V_{\text{off}}/(1+\beta)$.

If the initial imbalance is small ($|z_0| \ll 1$), the time evolution of the density and the order parameter shows clean periodic oscillations. As an example, in Fig. 3.2 we show the behavior of the density distribution for two different initial imbalances, $|z_0| = 0.024$ and $|z_0| = 0.06$; the barrier has width $d = 0.6k_F^{-1}$ and $V_0 = 5E_F$. The evolution of the relative population imbalance $z(t)$ and the phase difference $\Phi(t)$ is reported in Fig. 3.3. One already sees periodic oscillations, which can be interpreted as Josephson oscillations.

Josephson oscillations between weakly linked superfluids ($V_0 \gg \mu$) are characterized by the sinusoidal relation between current and phase difference [45]:

$$I(t) = I_J \sin\Phi(t) \ , \tag{3.1}$$

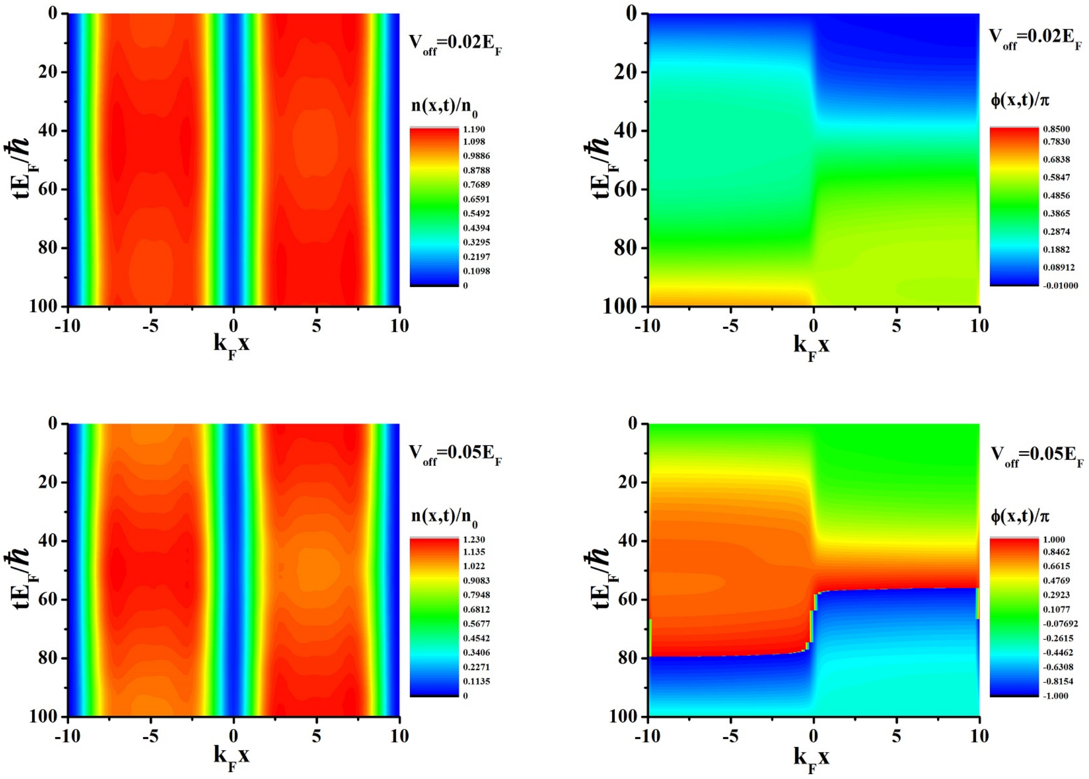

Figure 3.2: Evolution of the density distribution $n(x,t)/n_0$ (left plots) and the phase $\phi(x,t)/\pi$ (right plots) of a two-component superfluid Fermi gas at unitarity and zero temperature obtained by solving the time-dependent BdG equations (Eqs. 2.15). Time, in units of $\hbar/E_F$, flows from top to bottom. The gas is uniform in the transverse directions and confined between hard walls in the longitudinal direction at $x = \pm L/2$ with $L = 20k_F^{-1}$, with a central square barrier of height $V_0 = 5E_F$ and width $d = 0.6k_F^{-1}$ respectively. The number of atoms is $N = 100$. The initial imbalance is produced by adding a constant offset potential V_{off} at $t < 0$ on the left side only; here we use $V_{\text{off}} = 0.02E_F$ (upper plots) and $V_{\text{off}} = 0.05E_F$ (lower plots), which corresponds to an initial relative imbalance $z_0 = -0.024$ (lower plots) and $z_0 = -0.06$ (lower plots).

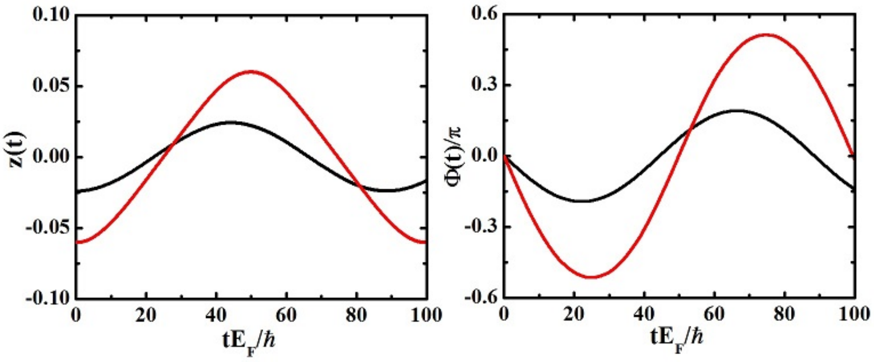

Figure 3.3: Relative population imbalance (left) and phase difference (right) as a function of time for the same simulation of Fig. 3.2 Black lines:$|z_0| = 0.024$ and $V_{\rm off} = 0.02E_F$; Red lines: $|z_0| = 0.06$ and $V_{\rm off} = 0.05E_F$

.

where the quantity I_J has the meaning of critical Josephson current. In our case, the current flowing at the barrier position can be easily calculated as $I = dN_R/dt = -dN_L/dt = -(N/2)dz/dt$. Fig. 3.4 shows four examples of the current-phase relation obtained in our simulations with different values of the initial imbalance. The upper plots correspond to the simulation of Fig. 3.3.

If the initial imbalance exceeds a critical value, the system enters into a different dynamical regime, where one of the two wells (in our case, the right well) remains always more populated than the other. The two numbers N_L and N_R oscillate in time, but around unequal mean values. This phenomenon is known as macroscopic quantum self-trapping [47, 48]. In Fig. 3.5 and 3.6 we show a typical example. We notice that the population imbalance oscillates with a period shorter than for small Josephson oscillation.

The transition from the regime of Josephson oscillations to the regime of self-trapping can be visualized by plotting the trajectories in the diagram of the population imbalance *vs.* the phase difference. Our results for the barrier with $V_0 = 5E_F$ and $d = 0.6k_F^{-1}$ are shown in Fig. 3.7. Josephson oscillations correspond to close trajectories, which become elliptic for small amplitudes, while self-trapping correspond to open trajectories. For the barrier used in these simulations, the transition

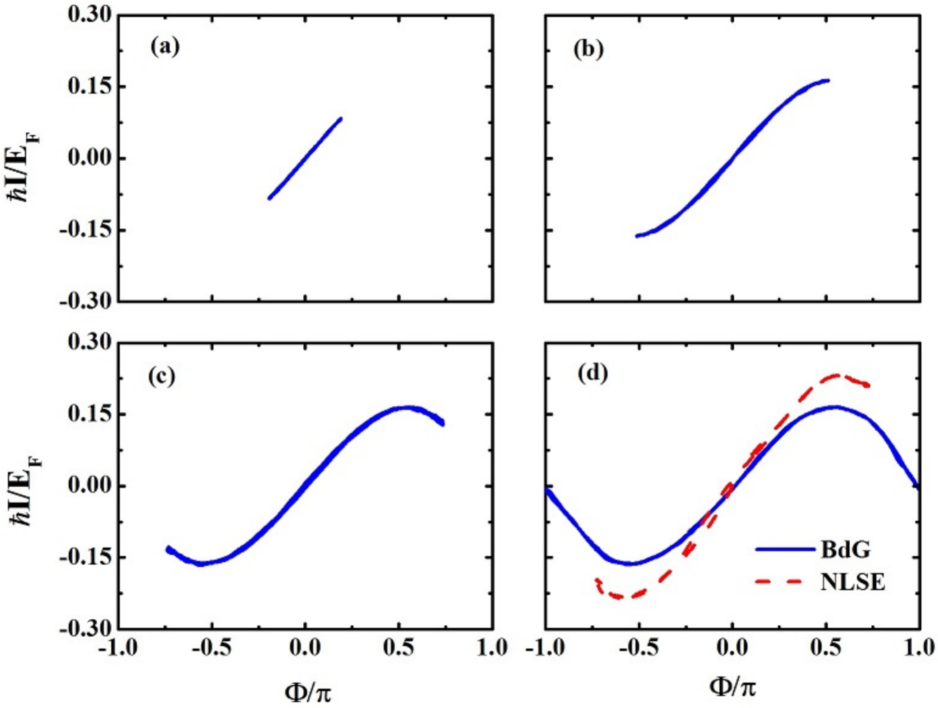

Figure 3.4: The current-phase relation obtained in four BdG simulations with the same barrier ($V_0 = 5E_F$ and $d = 0.6k_F^{-1}$) and different initial imbalance, $z_0 = -0.024$ (a), -0.06 (b), -0.078 (c), and -0.096 (d). The red dashed line in panel (d) is obtained by solving the nonlinear Schrödinger equation in the same configuration and for the same initial imbalance.

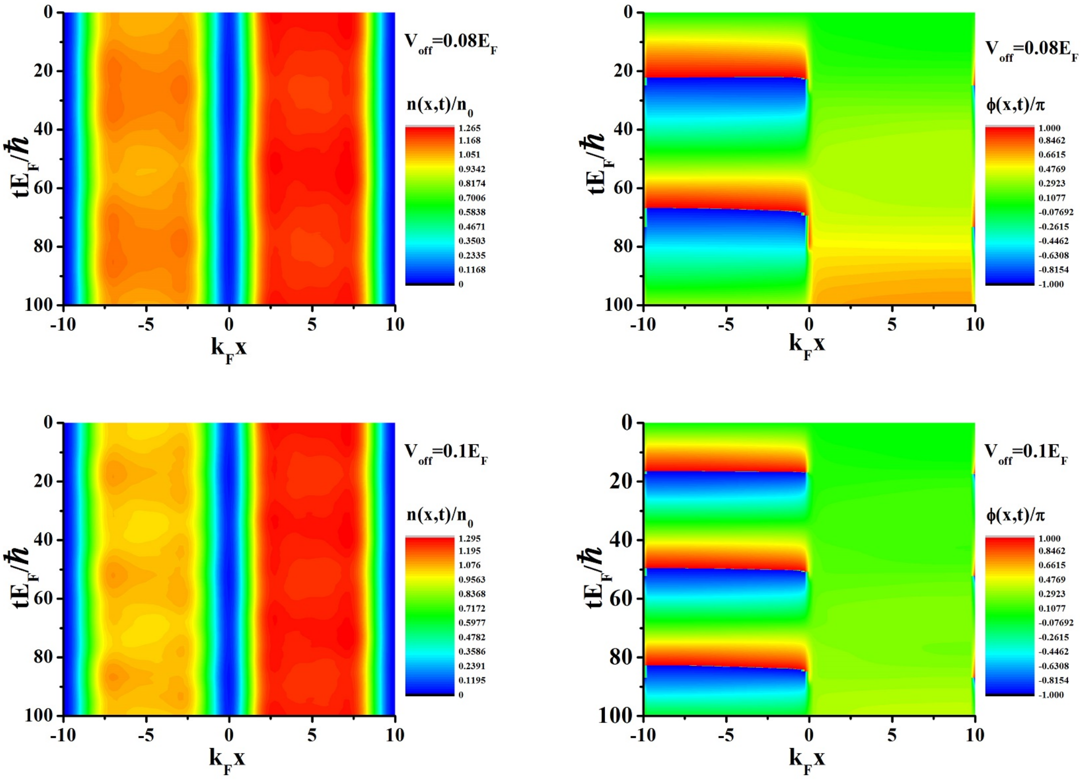

Figure 3.5: Same as in Fig. 3.2 but for a larger initial imbalance (in the upper two panels $z_0 = -0.096$, and in the lower ones $z_0 = -0.121$), such to cause self-trapping.

between the two regime occurs at an initial relative imbalance $|z_0| \approx 0.0869$. In the next chapter, we will give a detailed explanation of this critical transition after introducing a suitable two-mode model.

3.2 Two-mode model for small Josephson oscillations

In the previous section we have seen the results of numerical BdG simulations of weakly coupled superfluids (Fermi superfluid at unitarity) from the regime of small Josephson oscillations to the regime of self-trapping. In this section, we restrict

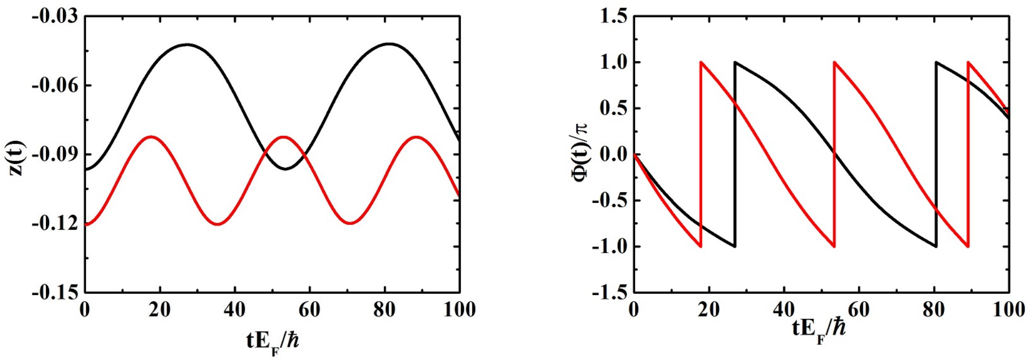

Figure 3.6: Relative population imbalance $z(t)$ and phase difference $\Phi(t)/\pi$ for the same simulation of Fig. 3.5. Black lines: $|z_0| = 0.096$ and $V_{\text{off}} = 0.08E_F$; Red lines: $|z_0| = 0.121$ and $V_{\text{off}} = 0.1E_F$.

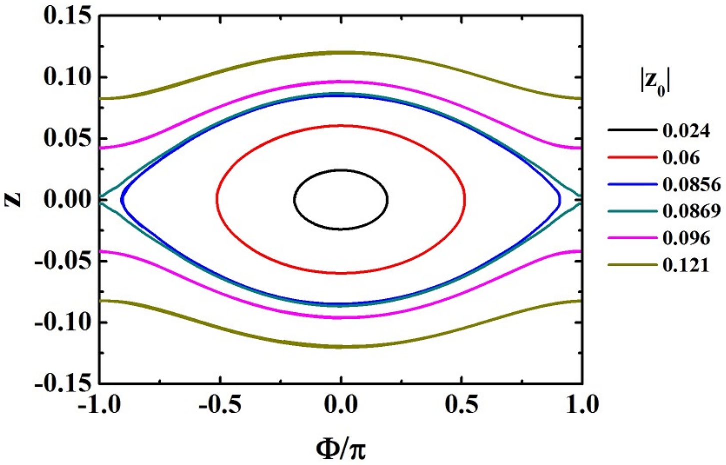

Figure 3.7: Population imbalance *vs.* phase difference in simulations with the same barrier ($V_0 = 5E_F$ and $d = 0.6k_F^{-1}$) and different initial imbalance, $|z_0| = 0.024$, 0.06, 0.0856, 0.0869, 0.096, 0.121, from the inner ellipse to the outer open trajectory. The red ellipse corresponds to the simulation in Fig. 3.2; the pink open trajectory corresponds to the simulation in Fig. 3.5. The transition from Josephson oscillations to self-trapping occurs at about $|z_0| \approx 0.0869$.

the discussions to the limit of small oscillation and we show that the above BdG results are well reproduced by Josephson junction equations for the two dynamical variables $z(t)$ and $\Phi(t)$, provided the barrier is large enough to remain in the weakly linked regime. In such a situation, the system can be described as composed by two superfluids located in each well and weakly coupled by tunneling. Unfortunately, a rigourous derivation of the Josephson equations from the BdG equations (2.15) within a two-mode approximation is not available. We thus proceed by analogy with the case of bosons where, in the Josephson regime, the population imbalance and the phase difference can be seen as canonically conjugates variables entering a classical Josephson Hamiltonian of the form [45]

$$H_J = \frac{E_C}{2} k^2 - E_J \cos\Phi \ . \tag{3.2}$$

The quantity k is defined as $k = (N_L^{(\mathrm{B})} - N_R^{(\mathrm{B})})/2$, where $N_L^{(\mathrm{B})}$ and $N^{(\mathrm{B})}$ are the number of bosons on the left and right side of the barrier, and is assumed to be small. The quantities E_C and E_J have the meaning of on-site energy (local interaction within each well) and tunneling energy (or Josephson coupling energy), respectively. From equation (3.2) one gets the equations of motion

$$\frac{\partial k}{\partial t} = -\frac{\partial H_J}{\partial(\hbar\Phi)} = -\frac{E_J}{\hbar}\sin\Phi \tag{3.3}$$

$$\frac{\partial \Phi}{\partial t} = \frac{\partial H_J}{\partial(\hbar k)} = \frac{E_C}{\hbar} k \ . \tag{3.4}$$

If $|\Phi| \ll 1$, the two equations admit harmonic solutions corresponding to Josephson oscillations of frequency

$$\omega_p = \frac{1}{\hbar}\sqrt{E_C E_J} \tag{3.5}$$

also known as plasma frequency. These results are valid in the Josephson regime where E_C/E_J is of order 1 or less, but much larger than N^{-2}; different regimes are obtained when $E_C/E_J \ll N^{-2}$ (Rabi regime) and $E_C/E_J \gg 1$ (Fock regime) [44, 46, 47, 48].

In order to check the applicability of this scheme to the BdG results of the previous section, we need to know how to calculate E_C and E_J within the same theory. We first notice that the tunneling energy E_J can be easily related to the

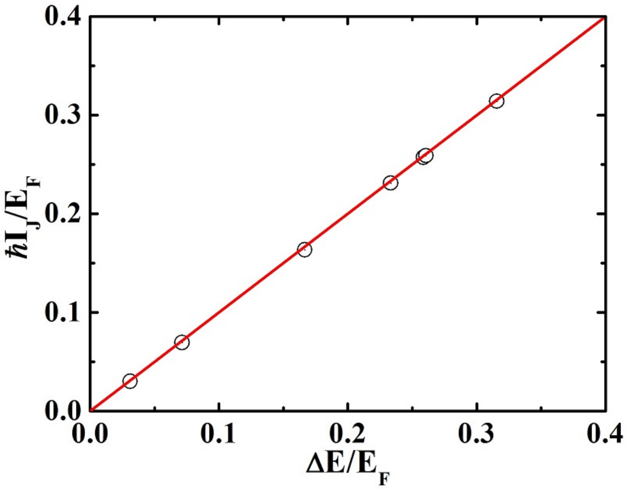

Figure 3.8: The Josephson current I_J extracted from time-dependent BdG simulations in the regime of small oscillations and weak tunneling is plotted as a function of the energy difference $\Delta E = E^- - E^+$, between the lowest antisymmetric and symmetric solutions of the stationary BdG equations (2.12). All points correspond to $E_{\text{cut}} = 50E_F$, $N = 100$, $L = 20k_F^{-1}$ and $L_\perp = 13k_F^{-1}$, while $(V_0/E_F,\ k_F d)$ is (5,1), (5,0.8), (5,0.6), (6,0.45), (5,0.5), (4,0.6), (4,0.55), for points from bottom-left to top-right. The red line represents the equality $\hbar I_J = \Delta E$.

energy difference $\Delta E = E^- - E^+$, where E^+ and E^- are the energies of the lowest symmetric and antisymmetric states in the double well potential with zero imbalance ($k = 0$). In fact, these states have $\Phi = 0$ and $\Phi = \pi$, respectively, and hence the Hamiltonian (3.2) gives $E_J = \Delta E/2$. Moreover we can relate both E_J and ΔE to the Josephson current I_J. In fact, the number of bosons, i.e., pairs of fermionic atoms, tunneling through the barrier at $x = 0$ per unit time is $I^{(\mathrm{B})} = -dk/dt$, so that the current of atoms is $I = 2I^{(\mathrm{B})} = (2E_J/\hbar)\sin\Phi$, as in Eq. (3.1), with $I_J = 2E_J/\hbar = \Delta E/\hbar$.

A nice feature of the last relation is that it can be numerically tested by performing two independent calculations. On one hand, the Josephson current I_J can be obtained by solving the time-dependent BdG equations (2.15): by looking at the current-phase plots, like those in Fig. 3.4, the current I_J can be extracted as the

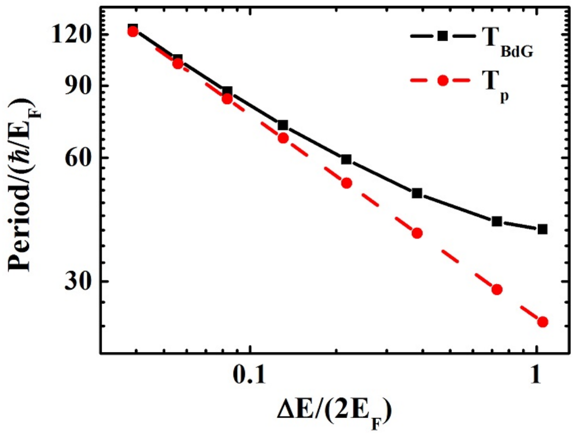

Figure 3.9: Period of small amplitude Josephson oscillations as a function of $\Delta E/2$, in log-log scale. The black solid line is the period T_{BdG} observed in time dependent BdG simulations for 99.3024 atoms in a double well potential. For each black point the width of the barrier is the same, $d = 0.6k_F^{-1}$, while its height decreases from $V_0 = 7E_F$ (leftmost point) to $0.6E_F$ (rightmost point). The red dashed line is the period $T_p = 2\pi/\omega_p = 2\pi\hbar/\sqrt{E_C E_J}$ of plasma oscillations, where E_C and E_J are calculated by solving the stationary BdG equations (2.12), assuming $E_J = \Delta E/2$.

maximum of the curve. On the other hand, the energy difference ΔE can be calculated by solving the stationary BdG equations (2.12) for the ground (symmetric) state and the lowest antisymmetric state (see details in section 2.3). In Fig. 3.8 we present the results obtained with about 100 particles in a box of size $L = 20k_F^{-1}$ and different barriers. This figure shows that the relation $I_J = \Delta E/\hbar$ is remarkably well satisfied. Remaining in the same regime of small tunneling (large barriers), we tested the same relation in the whole BCS-BEC crossover by performing the calculation of I_J and ΔE for different value of $1/(k_F a)$ from -1 (BCS) to $+1$ (BEC). The results are reported in the second and third columns of the table 3.1. The table shows that the relation $I_J = \Delta E/\hbar$ is accurate in the whole crossover.

The on-site energy E_C accounts for the variation of the interaction energy of the system due to the exchange of particles between the two wells. For a bosonic superfluid in a symmetric well, this parameter is given $E_C = 2d\mu^{(\mathrm{B})}/dN_L^{(\mathrm{B})}$ [45],

$1/(k_F a)$	$I_J(E_F/\hbar)$	$\Delta E(E_F)$	$E_J(E_F)$	$E_c(E_F)$	$T_p(\hbar/E_F)$	$T_{\mathrm{BdG}}(\hbar/E_F)$
1	0.109	0.1208	0.0604	0.0415	125.47	127.25
0.75	0.120	0.1293	0.0647	0.0463	114.82	116.76
0.5	0.135	0.1411	0.0705	0.0526	103.20	105.64
0.25	0.151	0.1549	0.0775	0.0598	92.29	95.29
0	0.167	0.1666	0.0833	0.0679	83.57	87.01
-0.25	0.170	0.1687	0.0844	0.0728	80.16	81.75
-0.5	0.167	0.1659	0.083	0.0812	76.54	80.02
-0.75	0.151	0.1517	0.0759	0.0846	78.42	81.55
-1	0.133	0.1339	0.067	0.0863	82.66	85.59

Table 3.1: For different values of the interaction strength $1/(k_F a)$, we report the values of critical Josephson current I_J, the energy difference $\Delta E = E^- - E^+$, the tunneling energy $E_J = \Delta E/2$, the on-site interaction energy $E_C = 8(\partial\mu/\partial N_L)$, the plasma period $T_p = 2\pi\hbar/\sqrt{E_C E_J}$ and the period T_{BdG} measured in TDBdG simulations. In all cases, the barriers has $V_0 = 5E_F$ and $d = 0.6k_F^{-1}$, and the number of atoms is $N = 100$.

where $\mu^{(\mathrm{B})}$ is the chemical potential and its derivative is calculated at $N_L^{(\mathrm{B})} = N^{(\mathrm{B})}/2$. Expressing the same quantity in terms of the chemical potential of the fermionic atoms and the number of atoms, we can write $E_C = 8d\mu/dN_L$. This quantity can be obtained by solving the stationary BdG equations (2.12) for different atom numbers in the same double well. Having E_J and E_C, we can finally calculate the plasma period $T_p = 2\pi/\omega_p = h/\sqrt{E_C E_J}$ and compare it with the period of the oscillations observed in the time-dependent BdG simulations for Josephson oscillations of small amplitude ($z_0 \to 0$). The comparison is reported in Fig. 3.9, where we plot T_{BdG} (black solid line) and T_p (red dashed line) as a function of $E_J = \Delta E/2$. The same data are also given in table 3.2. As one can see, in the limit of small tunneling ($\Delta E \to 0$), the period observed in the BdG simulations nicely approach the plasma period T_p. The same agreement is found in the whole BCS-BEC crossover (see table 3.1).

These results show that the small oscillations of two weakly coupled fermionic superfluids at unitarity, as obtained with the BdG equations, can be accurately

$V_0(E_F)$	$\Delta E(E_F)$	$E_J(E_F)$	$E_c(E_F)$	$T_p(\hbar/E_F)$	$T_{\mathrm{BdG}}(\hbar/E_F)$
7	0.078	0.039	0.0683	121.76	123.7
6	0.1119	0.0559	0.0681	101.8	104.3
5	0.1666	0.0833	0.0679	83.57	87.0
4	0.2606	0.1303	0.0676	66.95	72.0
3	0.4342	0.2171	0.0672	52.02	59.4
2	0.7671	0.3835	0.0667	39.29	49.1
1	1.4583	0.7291	0.0661	28.62	41.9
0.6	2.1059	1.0529	0.0659	23.86	40.1

Table 3.2: For a barrier of width $d = 0.6k_F^{-1}$ and different values of height V_0, we report the results of stationary BdG calculations of the energy difference $\Delta E = E^- - E^+$, the tunneling energy $E_J = \Delta E/2$, the on-site interaction energy $E_C = 8(\partial\mu/\partial N_L)$, and the plasma period $T_p = 2\pi\hbar/\sqrt{E_C E_J}$. In the last column we give the period of Josephson oscillations extracted from TDBdG simulations.

reproduced by a two-mode model for Josephson oscillations.

For larger oscillations and the transition to self-trapping, the classical Josephson Hamiltonian (3.2) does not apply anymore. However, the nonlinear effects can also be properly included in a new Josephson Hamiltonian derived from a nonlinear Schrödinger equation, as we will see in section 4.1.

3.3 Strong coupling

When the barrier is small and the coupling between the wells is strong, the two-mode model is no more valid. This happens when the overlap of the left and right parts of the order parameter under the barrier is large and the tunneling actually behaves like a macroscopic hydrodynamic flow [61]. The BdG equations can still be used to investigate the dynamics of the double well system also in this regime.

The stationary BdG equations were used by Spuntarelli *et al.* [4] to study the Josephson current in a uniform Fermi gas at unitarity in the presence of a square barrier. The calculations were performed in the regime of strong coupling, the

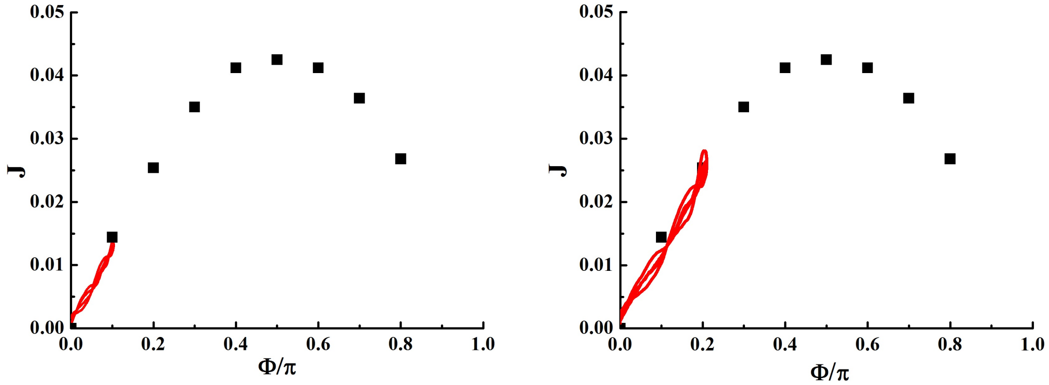

Figure 3.10: Current-phase relation for a unitary Fermi gas in the presence of a square barrier with $V_0 = 0.4E_F$ and $d = 4k_F^{-1}$. Black points were calculated in [4] by solving the stationary BdG equations in a uniform system and looking for solutions at constant current. The red lines are the results of our TDBdG simulations with a small initial imbalance in the double well potential with the same square barrier. The imbalance is produce with an offset potential $V_{\text{off}} = 0.02E_F$ (left) and $0.04E_F$ (right).

height of the barrier being smaller than the chemical potential of the gas. Their current-phase relation is reported in Fig. 3.10 (solid squares). We can compare their results with our time-dependent BdG simulations in a double well potential with the same barrier. The current density J is related to the current I by $J = I/L_\perp^2$. The tunneling energy is $E_J = 0.444E_F \approx 7E_C$. The simulation starts from a small initial imbalanced produced by an offset potential $V_{\text{off}} = 0.02E_F$ (left) and $0.04E_F$ (right). The system perform oscillations of small amplitude, without reaching the maximum current predicted by the stationary BdG calculations, but the two slopes agrees well. The small fluctuations in the current-phase relation in the TDBdG simulations are due to the presence of other excitations in the double well system, produced by the initial perturbation.

By further increasing the initial population imbalance (i.e., the offset potential), instead of stable large amplitude Josephson oscillations or self-trapping, we see the occurrence of a very complex dynamics. An example is shown in Fig. 3.11, where we plot the density $n(x,t)$ and phase different $\phi(x,t)$ in a time-dependent BdG

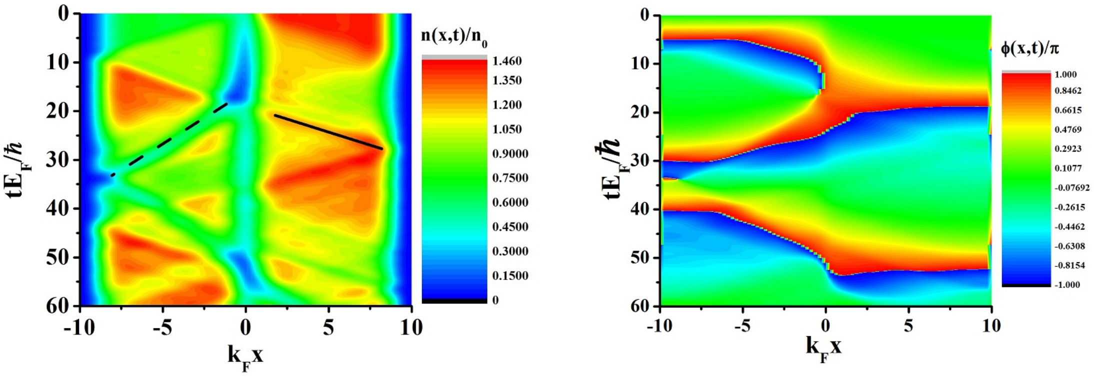

Figure 3.11: Evolution of the density distribution $n(x,t)/n_0$ and phase $\phi(x,t)$ at unitarity, obtained by solving the time-dependent BdG equations (2.15), as in Fig. 3.2, but for a lower barrier ($V_0 = 1E_F$ and $d = 0.6k_F^{-1}$). The initial imbalance is $|z_0| = 0.353$. Solid and dashed lines in the left panel represent the propagation of a sound-like density wave packet and a grey soliton, respectively.

simulation with a low barrier ($V_0 = 1E_F$ and $d = 0.6k_F^{-1}$), whose tunneling energy $E_J = 0.729E_F \approx 11E_C$. Besides Josephson current, the offset potential $V_{\rm off} = 0.3E_F$ also produce sound wave and soliton wave, and the Josephson current through the barrier is strongly coupled to the collective motion of the gas in the two wells. One can distinguish a density wave bouncing back and forth with a velocity of the order of the sound speed in a unitary Fermi gas with the same average density, $\sqrt{(1+\beta)/3}\ v_F$[41]. In addition, at about $t = 15\hbar/E_F$, when the density under the barrier almost vanishes, a grey soliton is nucleated. The soliton appears as a density depletion travelling leftward (dashed line) at a velocity smaller than the speed of sound. The phase of the order parameter has a variation of the order of π across the soliton. In the case of an infinite system, this mechanism of soliton nucleation induces a dissipation of the superfluid current due to phase slip [85]. In our confined double well system, solitons and collective sound-like waves are coupled by nonlinear mixing and eventually lead to a decay of the initial Josephson oscillation.

The current-phase relation for such complex dynamical processes is very different from the smooth sinusoidal behavior predicted by stationary calculations. An example of increasing complexity is given in Fig. 3.12, where we show what happens by increasing the initial imbalance. Each simulation starts at $t = 0$ from the point at $\Phi = 0$ and $I = 0$ and then follows a path backward in phase, but while for small imbalance the path traces a piece of sinusoidal curve in a small range of current and phase, for larger imbalance (bottom panels) both the phase and the current exhibit abrupt changes and the sinusoidal shape is completely lost. This is due to dynamical instabilities occurring in the region of the barrier, as in the case of the nucleation of the grey solitons of Fig. 3.11. These instability processes can not be predicted by the stationary BdG equations, but they are instead included in the full time-dependent BdG theory.

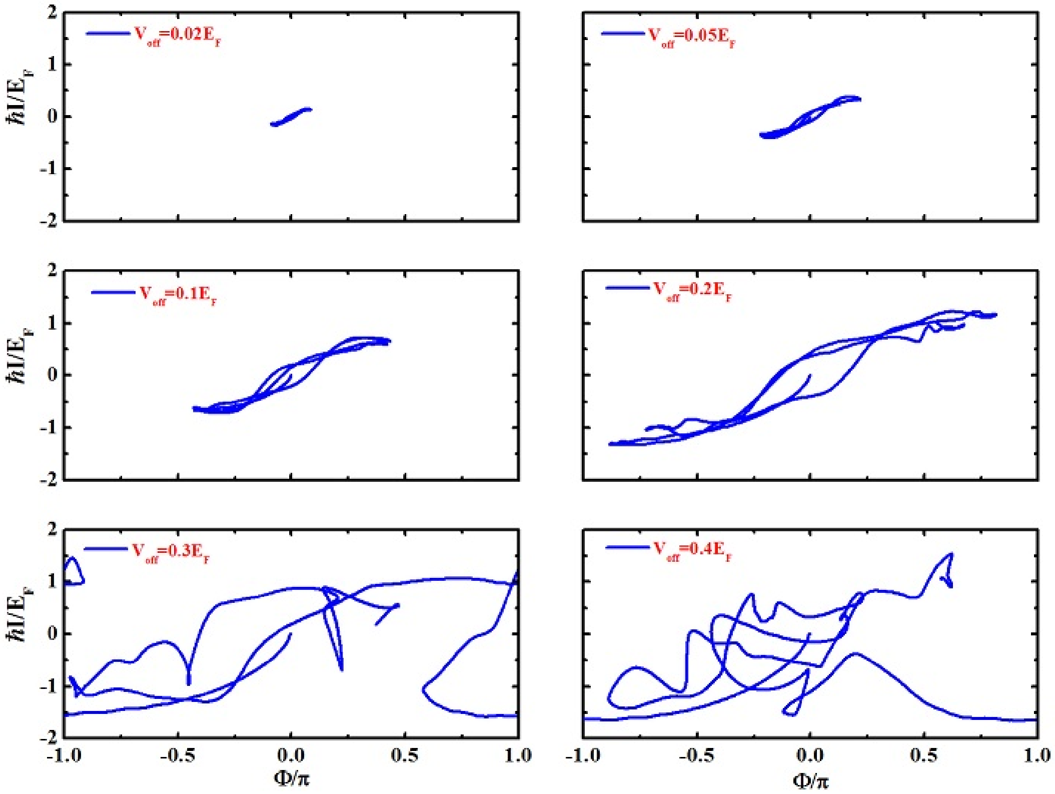

Figure 3.12: Phase-current relations obtained in time dependent BdG simulations for increasing initial population imbalance, from $V_{\mathrm{off}} = 0.02E_F$ (top left panel) to $V_{\mathrm{off}} = 0.4E_F$ (bottom right). The height and width of barrier are $V_0 = 1E_F$ and $d = 0.6k_F^{-1}$, respectively, and the corresponding tunneling energy is $E_J = 0.729E_F \approx 11E_C$.

Chapter 4

Nonlinear Josephson equations and density functionals

The classical Josephson Hamiltonian (3.2) does not apply for larger oscillations and the transition to self-trapping. In this chapter we discuss a different Josephson Hamiltonian perviously derived from a Nonlinear Schrödinger Equation (NLSE) [86]. We will give the comparison between NLSE and BdG equations. We will also discuss Superfluid Local Density Approximation (SLDA), developed by A. Bulgac *et al* [63, 64], which is a sort of generalized BdG-like equations and is expected to be more accurate than BdG at unitarity. NLSE and SLDA can be viewed as two different types of density functionals, suitable to describe lightly correlated fermions. We will apply all these methods to investigate the double well problem in the nonlinear regime.

4.1 Josephson effect in NLSE

For Bose-Einstein condensates governed by the Gross-Pitaevskii equation, coupled nonlinear Josephson junction equations for the number imbalance and the phase were analytically derived by Smerzi *et al.* [47, 48]. A similar derivation is also available for fermions in the BCS-BEC crossover within a phenomenological density functional theory [58, 59]. This theory is based on the use of the following nonlinear Schrödinger equation (NLSE) (also named density functional GP equation, or extended Thomas-

Fermi equation)

$$i\hbar\frac{\partial}{\partial t}\Psi(\mathbf{r},t) = \left[-\frac{\hbar^2}{4m}\nabla^2 + 2V_{\text{ext}}(\mathbf{r}) + \mu_{\text{loc}}^{(B)}(n,a)\right]\Psi(\mathbf{r},t) \tag{4.1}$$

for the order parameter Ψ of Cooper pairs of mass $2m$, with $|\Psi(\mathbf{r})|^2 = n(\mathbf{r})/2$, if n is the atom density. The key ingredient of this nonlinear Schrödinger equation is the local "bulk" chemical potential of Cooper pairs, $\mu_{\text{loc}}^{(B)}(n,a) = 2\mu(n,a) + \hbar^2/(ma^2)$, where $\mu(n,a)$ is the chemical potential of a uniform Fermi gas of density n and the second term is the binding energy of the pair. Its expression is an input of the theory; it can be taken from ab initio Monte Carlo calculations of the equation of state or from the mean-field BdG theory, or different suitable parameterizations. Once $\mu_{\text{loc}}(n,a)$ is given, the NLSE (4.1) can be numerically solved for studying stationary and/or time dependent configurations. The advantages and the limits of this approach have been widely discussed in the literature (see for instance the recent discussion in [87], and references therein). Here we only focus on the fact that, when applied to a double well potential in the weak link limit, the NLSE can be cast into the form of Josephson junction equations [58, 59]. This is done by assuming the order parameter to be a superposition of the left and right parts,

$$\Psi(\mathbf{r},t) = c_L(t)\Psi_L(\mathbf{r}) + c_R(t)\Psi_R(\mathbf{r}) \tag{4.2}$$

having an exponentially small overlap under the central barrier. By inserting this ansatz for Ψ into equation (4.1), after integration over space and neglecting exponentially small $\Psi_L\Psi_R$ terms, one obtains the equations

$$i\hbar\frac{\partial}{\partial t}c_L(t) = E_L c_L(t) - \mathcal{K} c_R(t) \tag{4.3}$$

$$i\hbar\frac{\partial}{\partial t}c_R(t) = E_R c_R(t) - \mathcal{K} c_L(t) \tag{4.4}$$

for the two complex coefficients $c_i(t)$ in region i, with $i = L, R$. The energy $E_i = E_i^0 + E_i^I$ is the sum of

$$E_i^0(\sqrt{N_i}) = \int d\mathbf{r}\Psi_i(\mathbf{r})\left[-\frac{\hbar^2}{4m}\nabla^2 + 2V_{\text{ext}}(\mathbf{r})\right]\Psi_i(\mathbf{r}) \tag{4.5}$$

$$E_i^I(\sqrt{N_i}) = \int d\mathbf{r}\Psi_i(\mathbf{r})\mu_{\text{loc}}^{(B)}(n_i,a)\Psi_i(\mathbf{r}) \ , \tag{4.6}$$

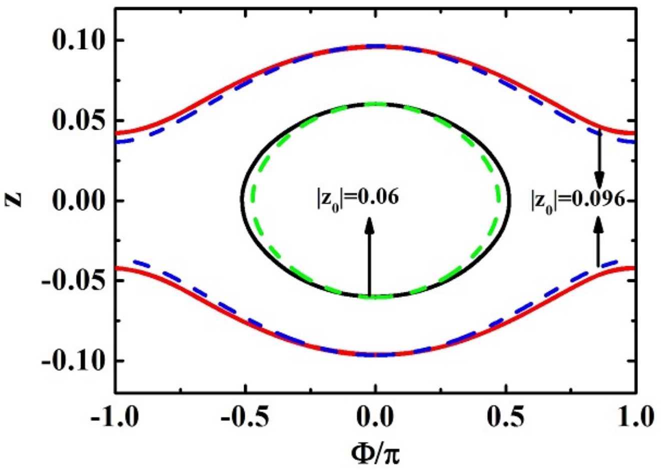

Figure 4.1: Population imbalance *vs.* phase difference at unitarity. The potential barrier has height $V_0 = 5E_F$ and width $d = 0.6k_F^{-1}$, as in Fig. 3.7. Solid lines are the results of time-dependent BdG simulations, while dashed lines are the solutions of the nonlinear Josephson equations (4.8) and (4.10), with $E_J = 0.0833E_F$ and $E_C = 0.0678E_F$ taken from the solutions of the stationary BdG equations. Closed trajectories correspond to Josephson oscillations with initial imbalance $|z_0| = 0.06$, while open trajectories correspond to self-trapped states with $|z_0| = 0.096$.

while the coupling term is given by

$$\mathcal{K} = -\int d\mathbf{r}\Psi_L(\mathbf{r})\left[-\frac{\hbar^2}{4m}\nabla^2 + 2V_{\text{ext}}(\mathbf{r})\right]\Psi_R(\mathbf{r})\ . \tag{4.7}$$

The functions $\Psi_R(\mathbf{r})$ and $\Psi_L(\mathbf{r})$ are real, obey the orthonormality condition $\int d\mathbf{r}\Psi_i\Psi_j = \delta_{i,j}$ and are localized in each of the two wells. In a symmetric system (i.e., $V_{\text{ext}}(-\mathbf{r}) = \mathrm{V}_{\text{ext}}(\mathbf{r})$), one has $\Psi_R(-\mathbf{r}) = \Psi_L(\mathbf{r})$ and thus $E_L^0 = E_R^0$ and $E_L^I = E_R^I = E^I$. By writing $c_{L,R} = \sqrt{N_{L,R}/2}\exp(i\phi_{L,R})$ and inserting it into Eqs. (4.3 and 4.4), one gets [58, 59]

$$\frac{\partial z}{\partial t} = -\frac{2\mathcal{K}}{\hbar}\sqrt{1-z^2}\sin\Phi \tag{4.8}$$

$$\frac{\partial \Phi}{\partial t} = \frac{1}{\hbar}\left[E^I(\sqrt{N_L}) - E^I(\sqrt{N_R})\right] + \frac{2\mathcal{K}}{\hbar}\frac{z\cos\Phi}{\sqrt{1-z^2}} \tag{4.9}$$

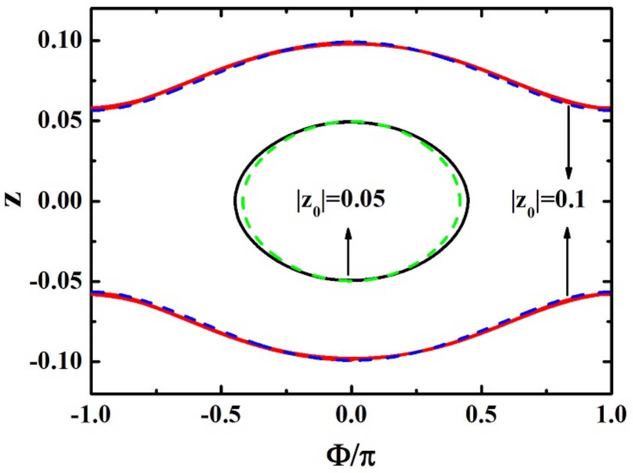

Figure 4.2: Population imbalance *vs.* phase difference at $1/(k_F a) = -0.5$. The potential barrier has height $V_0 = 5E_F$ and width $d = 0.6k_F^{-1}$. Solid lines are the results of time-dependent BdG simulations, while dashed lines are the solutions of the nonlinear Josephson equations (4.8) and (4.10), with $E_J = 0.083E_F$ and $E_C = 0.0812E_F$ taken from the solutions of the stationary BdG equations. Closed trajectories correspond to Josephson oscillations with initial imbalance $|z_0| = 0.05$, while open trajectories correspond to self-trapped states with $|z_0| = 0.1$.

where the imbalance z and the phase difference Φ are the same already defined at the beginning of section 3.1.

At unitarity the chemical potential of the uniform Fermi gas of density n is $\mu(n) = (1+\beta)E_F(n)$. This implies $E^I(\sqrt{N_i}) = U(N_i/2)^{2/3}$ with $U = [\hbar^2(3\pi^2)^{2/3}(1+\beta)/m]\int d\mathbf{r}\Psi_i^{10/3}$, and equation (4.9) becomes

$$\frac{\partial\Phi}{\partial t} = \frac{2\mathcal{K}}{\hbar}\left(\Lambda\left[(1+z)^{2/3} - (1-z)^{2/3}\right] + \frac{z}{\sqrt{1-z^2}}\cos\Phi\right) \tag{4.10}$$

where $\Lambda = (N/4)^{2/3}U/2\mathcal{K}$ [60] with the number of Fermi atoms $N = N_\uparrow + N_\downarrow$. The corresponding classical Hamiltonian is

$$\frac{H}{2\mathcal{K}} = \frac{3\Lambda}{5}\left[(1+z)^{5/3} + (1-z)^{5/3}\right] - \sqrt{1-z^2}\cos\Phi\ . \tag{4.11}$$

In the limit of small amplitude oscillations ($|\Phi| \ll 1$ and $|z| \ll 1$), the equations of motion (Eq. 4.8 and 4.10) reduce to the linear Josephson equations (3.3 and 3.4) provided the two parameters Λ and $\mathcal{K}$ are related to the on-site interaction energy E_C and the tunneling energy E_J by

$$\mathcal{K} = \frac{2E_J}{N} \ , \ \Lambda = \frac{3}{4}\left(\frac{N^2 E_C}{16 E_J} - 1\right) \ . \tag{4.12}$$

At this point we are ready to compare our BdG results of section 3.1 with the two-mode model including the nonlinear regime. For each configuration (i.e., for each set of parameters $L, L_\perp, V_0, d, N$) we can calculate the two energies E_C and E_J by solving the stationary BdG equations as explained in section 3.2. Then we can use them in Eq. (4.12) to calculate $\mathcal{K}$ and Λ and solve the nonlinear Josephson equations (4.8) and (4.10) for different values of the initial population imbalance. The results can then be compared with those obtained by solving the time-dependent BdG equations (2.15). In Fig. 4.1 we show typical results for the imbalance vs. phase diagram, for the same configuration of Fig. 3.7. The agreement between BdG equations (solid lines) and nonlinear Josephson equations (dashed lines) is remarkably good both in the case of Josephson oscillations (inner ellipse) and self-trapping (open trajectories). In the BdG simulations the transition between the two regimes occurs at $|z_0| \approx 0.0869$. In the case of the nonlinear Josephson equations (Eq. 4.8) and (4.10) the same transition is obtained when the energy (4.11) reaches the critical value [60]

$$E_{\rm cr} = 2\mathcal{K}\left(\frac{6\Lambda}{5} + 1\right) = \frac{4E_J}{N}\left(\frac{9N^2 E_C}{160 E_J} + \frac{1}{10}\right) \ . \tag{4.13}$$

For the parameters of Fig. 4.1, this condition corresponds to $|z_0| \approx 0.0893$, which is again very close to the BdG result.

The agreement between BdG equations and nonlinear Josephson equations is not restricted to unitarity. We tested that a similar agreement is found also for $1/(k_F a) \neq 0$, both at the BEC side ($1/(k_F a) > 0$) and BCS side ($1/(k_F a) < 0$, see Fig. 4.2) of the BCS-BEC crossover. This suggests that the validity of the nonlinear Josephson equations (4.8) and (4.9) is more general than the validity of the NLSE (4.1) which is known to be accurate in the BEC regime but not in the BCS regime, where it misses the fermionic degrees of freedom. In Ref. [58, 59] it was noticed

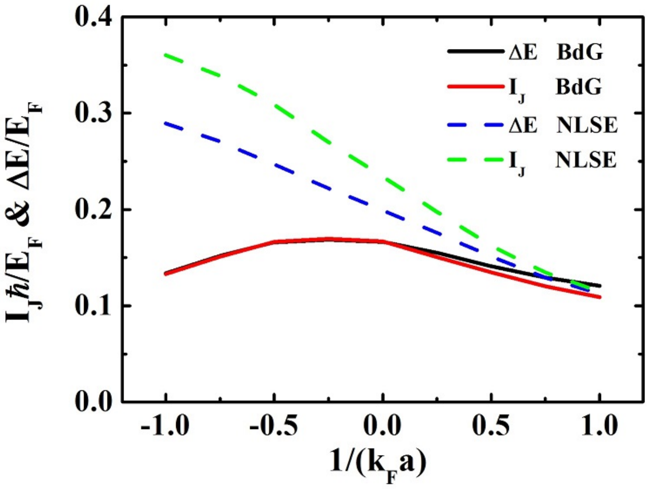

Figure 4.3: Energy difference ΔE and maximum Josephson current I_J calculated with the BdG equations (solid lines) and the NLSE (dashed lines), as a function of the interaction strength $1/(k_F a)$. The parameters of the barrier are $d = 0.6k_F^{-1}$ and $V_0 = 5E_F$, and the number of atoms $N = 100$.

that, despite this inaccuracy of the NLSE, the nonlinear Josephson equations can still be used in the whole crossover, provided the tunnelling energy is taken as a phenomenological parameter. Our numerical results show that the same nonlinear Josephson equations are a very good approximation of the weak link limit of the BdG equations, the parameters E_C and E_J being consistently calculated within the same BdG theory.

The difference between NLSE and BdG equations can be appreciated by looking at Fig. 4.3, where we plot the results for the maximum Josephson current, I_J, together with the energy difference ΔE. The quantity I_J is extracted from time-dependent simulations, either solving the BdG equations (2.15) (red solid line) or the NLSE (4.1) (upper dashed line), while ΔE is calculated from the corresponding stationary (time-independent) equations; in Eq. (4.1) we use the mean-field equation of state (MF EOS) for the local chemical potential [58, 59]. As discussed in section 3.2, in the weak link limit, where the nonlinear Josephson equations are expected to hold, the quantity ΔE should be equal to twice the tunneling energy

E_J and one should find $\hbar I_J = \Delta E$. This is clearly the case for BdG equations where ΔE (black solid line) and $\hbar I_J$ (red solid line) are almost indistinguishable in the whole crossover, the small difference in the BEC limit being likely due to the finite cutoff energy in the BdG calculations, which becomes a more critical parameter as $1/(k_F a)$ increases. Conversely in the case of NLSE, the two quantity are significantly different and the critical current I_J is increasingly larger than the BdG prediction in the BCS limit. The difference can be seen also in Fig. 3.4 where we show an example of Josephson oscillations at unitarity as obtained by solving Eq. (4.1) (dashed line) and Eqs. (2.15) (solid line) for the same configuration. The fact that I_J is larger in the NLSE than in BdG equations is well known and is simply due to pair-breaking processes which are included in BdG [88] but are absent in the NLSE. This effect was already discussed in Ref. [58, 59] in a regime of wider ($d > k_F^{-1}$) and lower ($V_0 < E_F$) barriers. Here, on purpose, we have chosen thinner barriers, i.e, d of the order or less than k_F^{-1}, in order to test the applicability of the two-mode model to cases where density and phase variations occur on the length scale of the inverse Fermi wave vector, such that the local density approximation becomes questionable and fermionic degrees of freedom might play a role. Our results indicate that, at least in the weak link limit and within a mean-field theory, the dynamics is still dominated by tunneling of bosonic pairs and is surprisingly well described by the nonlinear Josephson equations (4.8) and (4.9).

4.2 Can fermions exhibit π-mode oscillations?

Up to now, we have shown that the BdG theory successfully predicts the existences of Josephson oscillations and self-trapping of superfluid fermions and the results quantitatively agree with the ones of a two-mode model in the weak coupling limit. In particular the two-mode model can be used to find the critical initial population imbalance z_0 and phase difference Φ_0 for the transition between these two different dynamical regimes. For bosonic gases, the two-mode model also predicts π-mode Josephson oscillations which are periodic oscillations with time-average phase difference $\langle \Phi(t) \rangle = \pi$ and population imbalance $\langle z(t) \rangle = 0$. The corresponding π-mode self-trapping regimes corresponds to the case of oscillations with $\langle \Phi(t) \rangle = \pi$ but

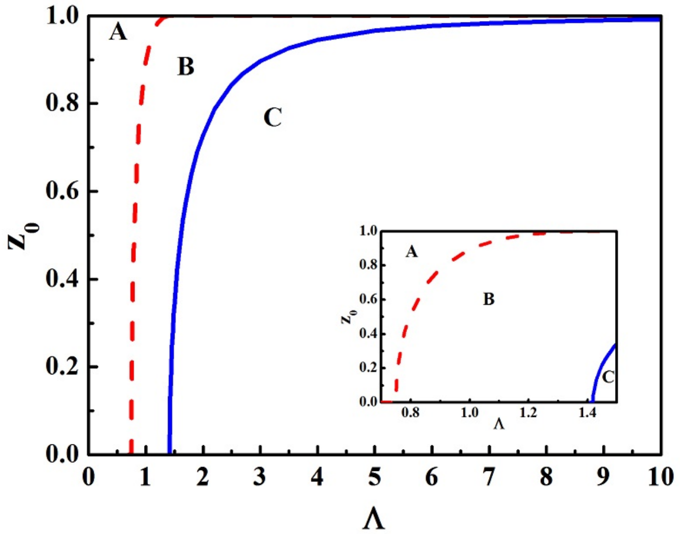

Figure 4.4: The phase diagrams for π-mode Josephson oscillation (region A), π-mode self-trapping (region B) and self-trapping (region C), when initial phase difference $\Phi_0 = \pi$. The red dashed line is the minimum initial population imbalance z_0 to investigate π-mode Josephson oscillation, while the blue solid line is the minimum z_0 to investigate π-mode self-trapping.

$\langle z(t) \rangle \neq 0$. It is natural to check whether the same π-mode exists also in superfluid fermions.

Let us start from the Fermi Josephson Hamiltonian $H(z, \Phi)$ (4.11), we want to find the range of parameters required to observe the π-mode Josephson and self-trapping oscillation. The emergence of these two dynamical regimes depend on the value of Λ in (4.12) and the initial values of z_0 and Φ_0. We focus our discussions on $\Phi_0 = \pi$. Our results are shown in Fig. 4.4. In the region A, we indeed find π-mode Josephson oscillation; in region B, we find π-mode self-trapping oscillation ($\langle \Phi(t) \rangle = \pi$); in region C, we find self-trapping oscillation ($\langle \Phi(t) \rangle = 0$). In the $z_0 \to 0^+$ limit, the thresholds are at $\Lambda = 0.75$ and 1.42, the first value can be obtained analytically by solving equation $\partial^2 H(z \to 0, \pi)/\partial z^2 = 0$, while the latter value obtained by solving equations $H(0, \pi) = H(1, 0)$. If Λ is large, the π-mode self-trapping is accessible only in a very narrow parameter space.

Both π-mode Josephson oscillations and π-mode self-trapping require Λ not too large. In our simulations, for $N = 100$, with a typical weak-coupling barrier, $V_0 = 5E_F$ and $d = 0.6k_F^{-1}$, from Eq. (4.12) and Table 3.2, we find $\Lambda = 375$, which is definitely too large. For this value of Λ, the system never exhibits the π-mode Josephson oscillations or π-mode self-trapping.

In order to get small enough value of Λ, one must use a smaller particle number N, small on-site energy E_C and a large tunneling energy E_J. However, E_C is proportional to the chemical potential μ, which is of the order of Fermi energy, while E_J is of the order of the soliton energy, which is proportional to the transverse area. Increasing transverse area would dramatically increase the computation time. In a word, one may observe the π-mode in the BEC side of the crossover for a system with less particles, but is almost impossible at unitarity.

4.3 Superfluid local density approximation

The density functional theory (DFT) introduced by Hohenberg and Kohn [89, 90] has become the tool of choice in the calculation of the properties of essentially most electron systems [91] after the introduction of the local density approximation (LDA) by Kohn and Sham [92]. The DFT was firstly used for electrons in the normal (non superconducting) state. It is based on the assumption that there is a unique mapping between the external potential, the total wave function of the system, and the normal density and that the exact energy of the system can be written as a density functional. A limit of the theory is that the exact form of the functional is not known. Phenomenological functionals are typically introduced for each system. The original formulations rely on the Kohn-Sham orbitals and thus can not deal effectively with superfluidity. The DFT extension to superfluid system is an important problem of the quantum many-body theory. Bulgac and Yu [93, 94, 95, 96] recently introduced a density functional from fermions a unitarity, named superfluid local density approximation (SLDA). This SLDA originates from similar DFT previously used in the context of nuclear physics [93, 95].

A nice feature of ultracold fermions is that at unitarity the form of the energy density functional is restricted by dimensional arguments. Another advantage is the availability of *ab initio* results for homogeneous and inhomogeneous system, which can be used to fix the parameters of the density functional.

In superfluid fermions, two atoms with different spin can form a Cooper pair. Correspondingly the system possesses an anomalous Cooper-pair density ν in addition to the normal atomic density n. The energy density functional ε of the system must include the kinetic density τ, the total normal density n, and the anomalous density ν. The density functional introduced by Bulgac and Yu [93, 95, 63]

$$\varepsilon(\mathbf{r}) = \alpha\frac{\hbar^2}{2m}\tau(\mathbf{r}) + \beta\frac{3\hbar^2(3\pi^2)^{2/3}}{10m}n^{5/3}(\mathbf{r}) + \gamma\frac{\hbar^2}{mn^{1/3}(\mathbf{r})}|\nu(\mathbf{r})|^2 \tag{4.14}$$

with

$$n(\mathbf{r}) = 2\sum_k |v_k(\mathbf{r})|^2,\ \tau(\mathbf{r}) = 2\sum_k |\nabla v_k(\mathbf{r})|^2,\ \nu(\mathbf{r}) = \sum_k u_k(\mathbf{r})v_k^*(\mathbf{r}). \tag{4.15}$$

The effective mass parameter α, the Hartree parameter β and the pairing parameter γ are all dimensionless parameters, and $u_k(\mathbf{r})$ and $v_k(\mathbf{r})$ are the usual Bogoliubov quasiparticle amplitude with k labels the quasiparticle states. With respect to the energy density of BdG theory, what is new is the introduction of the Hartree term $\beta(3\hbar^2(3\pi^2)^{1/3})n^{5/3}/(10m)$, which is the order of Fermi energy E_F, because E_F is the only energy scale of unitary Fermi gases. This Hartree term assumes that the atoms of different spins still interact with each other, even when the gas becomes normal, while BdG predicts that it becomes noninteracting.

Since the kinetic and anomalous densities diverge [62, 81, 78], a regularization procedure is needed for the pairing gap and for the energy density. The regularized density functional is as follow:

$$\varepsilon(\mathbf{r}) = \alpha\frac{\hbar^2}{2m}\tau_c(\mathbf{r}) + \beta\frac{3\hbar^2(3\pi^2)^{2/3}}{10m}n^{5/3}(\mathbf{r}) + g_{\text{eff}}|\nu_c(\mathbf{r})|^2 \tag{4.16}$$

where the effective coupling constant g_{eff} is given by

$$\frac{1}{g_{\text{eff}}(\mathbf{r})} = \frac{mn^{1/3}(\mathbf{r})}{\hbar^2\gamma} - \frac{mk_{\text{cut}}(\mathbf{r})}{2\pi^2\hbar^2\alpha}\left[1 - \frac{k_F(\mathbf{r})}{2k_{\text{cut}}(\mathbf{r})}\ln\frac{k_{\text{cut}}(\mathbf{r}) + k_F(\mathbf{r})}{k_{\text{cut}}(\mathbf{r}) - k_F(\mathbf{r})}\right] \tag{4.17}$$

an all summations are restricted by an energy cutoff E_{cut}

$$\tau_c(\mathbf{r}) = 2\sum_{E_k<E_{\text{cut}}} |\nabla v_k(\mathbf{r})|^2,\ \nu_c(\mathbf{r}) = \sum_{E_k<E_{\text{cut}}} u_k(\mathbf{r})v_k^*(\mathbf{r}). \tag{4.18}$$

The expression for order parameter is

$$\Delta(\mathbf{r}) = -g_{\text{eff}}(\mathbf{r})\nu_c(\mathbf{r}). \tag{4.19}$$

The stationary SLDA equations for the quasiparticle wave function is obtained by the standard functional minimization with respect to variations u and v. One obtains

$$\begin{bmatrix} h(\mathbf{r})-\mu & \Delta(\mathbf{r}) \\ \Delta^*(\mathbf{r}) & -h(\mathbf{r})+\mu \end{bmatrix} \begin{bmatrix} u_k(\mathbf{r}) \\ v_k(\mathbf{r}) \end{bmatrix} = E_k \begin{bmatrix} u_k(\mathbf{r}) \\ v_k(\mathbf{r}) \end{bmatrix} \tag{4.20}$$

with a single quasiparticle Hamiltonian

$$h(\mathbf{r}) = -\alpha\frac{\hbar^2}{2m}\nabla^2 + U(\mathbf{r}), \quad U(\mathbf{r}) = \beta\frac{\hbar^2(3\pi^2 n(\mathbf{r}))^{2/3}}{2m} - \frac{\hbar^2|\Delta(\mathbf{r})|^2}{3\gamma m n^{2/3}(\mathbf{r})} + V(\mathbf{r}) \tag{4.21}$$

Here E_{cut} is a cutoff energy and $V(\mathbf{r})$ is an external potential, with $E_{\text{cut}} + \mu = \alpha\hbar^2 k_{\text{cut}}^2(\mathbf{r})/(2m) + U(\mathbf{r})$ and $\mu = \alpha\hbar^2 k_F^2(\mathbf{r})/(2m) + U(\mathbf{r})$.

By requiring that a homogeneous gas of number density $n = N/V = k_F^3/(3\pi^2)$ has an energy per particle $E/N = 3\xi_S E_F/5$, a chemical potential $\mu = \xi_S E_F$, and a pairing order parameter $\Delta = \eta E_F$, one can determine the value of dimensionless parameters α, β and γ in Eq. (4.16) through the following equations

$$n = \int \frac{d^3k}{(2\pi)^3}\left(1 - \frac{\xi_k}{E_k}\right), \tag{4.22}$$

$$\frac{3}{5}E_F n(\xi_S - \beta) = \int \frac{d^3k}{(2\pi)^3}\left[\alpha\frac{\hbar^2k^2}{2m}\left(1 - \frac{\xi_k}{E_k}\right) - \frac{\Delta}{2E_k}\right], \tag{4.23}$$

$$\frac{mn^{1/3}}{\hbar^2\gamma} = \int \frac{d^3k}{(2\pi)^3}\left(\frac{m}{\alpha\hbar^2k^2} - \frac{1}{2E_k}\right), \tag{4.24}$$

where

$$\xi_k = \alpha\frac{\hbar^2k^2}{2m} + \left(\beta - \frac{(3\pi^2)^{2/3}\eta^2}{6\gamma} - \xi_S\right)E_F, \quad E_k = \sqrt{\xi_k^2 + \Delta^2}. \tag{4.25}$$

In these three constraint equations, ξ_S and η are the only two inputs, which can be taken from reliable quantum Monte Carlo calculations [97, 29, 98, 99] or experiment results [8]. For ξ_S, the Auxiliary Field Monte Carlo [98] provides the value $\xi_S = 0.372$ which is quite close to the experimental value $\xi_S = 0.376$ [8]. As to η, the QMC value is $\eta = 0.504$ [29] while RF-spectroscopy gives $\eta = 0.44$ [100]. By using $\xi_S = 0.372$ and $\eta = 0.504$ [97], one obtains the values of the effective mass parameter $\alpha = m/m^* = 1.076$, the Hartree parameter $\beta = -0.525$ and for pairing parameter $1/\gamma = -0.0853$.

In order to check the accuracy of SLDA, several calculations have already been performed to calculate the spectrum of the elementary fermionic excitations of a homogeneous unitary Fermi gas, and the total energy $E(N)$ of a finite system. The agreement with Monte Carlo results (the Green Function Monte Carlo and fixed node-diffusion Monte Carlo) is very good [63].

By replacing E_k in Eq. (4.20) with the operator $i\hbar\partial/\partial t$, one obtains the time-dependent SLDA equations (TDSLDA)

$$\begin{bmatrix} h(\mathbf{r},t)-\mu & \Delta(\mathbf{r},t) \\ \Delta^*(\mathbf{r},t) & -h(\mathbf{r},t)+\mu \end{bmatrix} \begin{bmatrix} u_k(\mathbf{r},t) \\ v_k(\mathbf{r},t) \end{bmatrix} = i\hbar\frac{\partial}{\partial t} \begin{bmatrix} u_k(\mathbf{r},t) \\ v_k(\mathbf{r},t) \end{bmatrix}. \tag{4.26}$$

However, if the effective mass parameter α is not equal to 1 (i.e., the effective mass is different from the bare atomic mass), then one must also introduce a term involving the current density in order to restore Galilean invariance. This complicates the numerical implementation. To avoid this trouble and since $\alpha \approx 1$, in TDSLDA one typically sets $\alpha = 1$, while adjusting β and γ to reproduce the energy per particle and pairing gap [101, 87, 102]. Following this idea, we set $\alpha = 1$, inserting $\xi_S = 0.372$ and $\eta = 0.504$ in Eqs. (4.22) and (4.24). We obtain $\beta = -0.432$ and $1/\gamma = -0.0758$. This TDSLDA is expected to give quantitatively reliable predictions of the dynamics of the unitary Fermi superfluid. This density functional has been already used to investigate the dynamics of quantized vortices [103], quantum shock waves and domain walls [104], quantized superfluid vortex rings [102].

In the next section, we will use this TDSLDA to study the Josephson effect of unitary Fermi gases at zero temperature.

4.4 Josephson effect with SLDA

Previously seen that the agreement between two-mode model and BdG theory is very good; the energy difference is equal to the critical Josephson current, $\Delta E = \hbar I_J$,

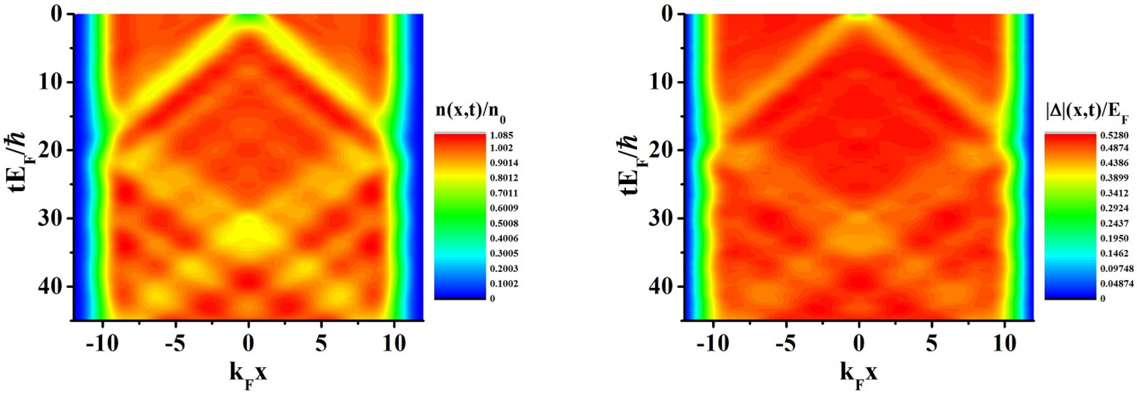

Figure 4.5: Evolutions of density $n(x,t)/n_0$, the phase of order parameter $\phi(x,t)/\pi$ and absolute value of order parameter $|\Delta(x,t)|/E_F$, obtained by solving the time-depend superfluid local density approximation equations (4.26). We use an offset potential $V_{\text{off}} = 1E_F$ and $d = 0.6k_F^{-1}$ to produce a locally low density in the middle of the box, then release it at $t = 0E_F/\hbar$. We could observe a sound wave travelling back and forth inside of the box, with speed approximately $0.35v_F$.

and for small amplitude the period of Josephson oscillations obtained from time-dependent BdG equations agrees well with plasma period at small coupling, namely $T_{\text{BdG}} = T_p$. However, the BdG theory is believed to be a qualitatively reliable theory, and thus, it is interesting to use TDSLDA (4.26) to check whether the physical pictures remains the same.

Here we do all the simulations in a box whose size is $L = 24k_F^{-1}$ and $L_\perp = 13k_F^{-1}$, with $N = 120$ atoms. We begin our work with the simulations of the sound waves, from which one can measure the first sound speed. We use a potential barrier $V_0 = 1E_F$ and $d = 0.6k_F^{-1}$ to produce a local density depletion in the center of the box, and then we remove it at time $t = 0$. In Fig. 4.5, as expected, we observe two sound wave-packets travelling back and forth in the box, with speed approximately $0.35v_F$. The analytical prediction $c_s = \sqrt{\xi_S/3}v_F$ with the parameters ξ_S taken from the SLDA gives $c = 0.35v_F$, in good agreement with the universal relation. The absolute value of order parameter $|\Delta(x,t)|$ also exhibits a local depletion moving at the same speed. This shows that $\Delta(x,t)$ and $n(x,t)$ are coupled.

$V_0(E_F)$	$\mathrm{d}(k_F^{-1})$	$I_J(E_F/\hbar)$	$E_J(E_F)$	$E_c(E_F)$	$T_p(\hbar/E_F)$	$T_{\mathrm{SLDA}}(\hbar/E_F)$
2	1	0.143	0.0711	0.0353	125.5	130.3
3	0.6	0.214	0.106	0.0350	103.3	110.3
3	0.8	0.107	0.0533	0.0353	144.9	148.7
4	0.6	0.122	0.0608	0.0352	135.8	140.0

Table 4.1: Results for small-amplitude Josephson oscillations for different initial conditions. On site energy E_C and tunneling energy $E_J \equiv \Delta E/2$ are calculated by stationary SLDA equations, which give the plasma period $T_p = 2\pi\hbar/\sqrt{E_J E_c}$, while T_{SLDA} is the same period but from TDSLDA simulations.

In the case of the Josephson effect in a double well system, we report the same procedure already used with BdG equations, using the same geometry and the same steps for the calculations. We first use the stationary SLDA equations to calculate all static physical quantities, e.g., on-site energy E_C and tunneling energy E_J, which is also defined as half of energy difference ΔE, from which we get the plasma period $T_p = 2\pi/\omega_p$. Then we solve the time-dependent SLDA equations to simulate the Josephson oscillations, extracting the values of the period T_{SLDA}. We also calculate I_J as the maximum current for full sinusoidal curves in the current-phase plot. The key result of this systematic analyses is that, again, small amplitude oscillations are very well reproduced by the two-mode model. In particular

$$2E_J \equiv \Delta E \cong I_J; \quad T_p \cong T_{\mathrm{SLDA}} \tag{4.27}$$

provided the parameters E_C and E_J are consistently calculated with the same SLDA theory. Examples of universal results are given in Table 4.1, for four different barriers, all of them in the weak coupling regime.

To summarize, we find that the time-dependent superfluid local density approximation theory predicts the same physics as time-dependent Bogoliubov-de Gennes theory, SLDA being quantitatively more accurate in the values of key physical quantities.

Chapter 5

Dynamic structure factor

As discussed in the introduction, dynamic structure factor is an important dynamical quantity which can be measured experimentally by two-photon Bragg scattering techniques. Theoretically, random phase approximation (RPA) is a simple and common method to calculate the dynamic structure factor. In this chapter, first we show how to derive the random phase approximation from the energy density functional of the system. The basic idea has already been introduced by S. Stringari [105], in the Landau Fermi liquid frame. He developed a formalism to bridge RPA and energy density functional, by which he calculated the density and spin response function of polarized normal Fermi gases at unitarity. Inspired his work, we extend this formalism to superfluid Fermi gases, where the pairing effect (or Cooper-pair density) plays an important role. Since RPA has already been used in BdG theory [106, 107, 6], we will briefly present some basic results. Then we will present in details the derivation of the RPA formalism with the superfluid local density approximation. With SLDA+RPA we calculate the dynamic structure factor at unitarity and at zero temperature. The results are finally compared with those of BdG+RPA.

5.1 Random phase approximation

In order to study the response of a superfluid Fermi gas to a weak external field V_{ext}, usually the system can be treated as a gas of long-live Bogoliubov quasiparticles interacting through a mean field. The essential idea of RPA is that the induced fluctuation term of interaction is assumed to be a self-generated mean-field potential experienced by quasiparticles, associated with the local changes in normal atomic density ($n_\uparrow$ and $n_\downarrow$) and Cooper-pairs density ν.

Differently from normal gases, which have only two normal densities, $n_\uparrow = \left\langle \Psi_\uparrow^+ \Psi_\uparrow \right\rangle$ and $n_\downarrow = \left\langle \Psi_\downarrow^+ \Psi_\downarrow \right\rangle$, superfluid fermions have also another two superfluid Cooper-pair densities, $\nu = \langle \Psi_\downarrow \Psi_\uparrow \rangle$ and $\nu^* = \left\langle \Psi_\uparrow^+ \Psi_\downarrow^\dagger \right\rangle$. Typically the Cooper-pair density is a complex number, which has two degrees of freedom, its mode and phase; here we use ν and its conjugate ν^* to play the roles of these two degrees of freedom. In the following, we replace these four densities $n_\uparrow$, $n_\downarrow$, ν and ν^* with n_1, n_2, n_3 and n_4, respectively. A small external perturbation induces variations δn_i and correspondingly variations of the energy of the system, In the linear response regime one can write four different quasiparticle Hamiltonians when describing the superfluid fermions with quasiparticle language:

$$H_1 = H_0 + \left(\frac{\partial \varepsilon_{\text{int}}}{\partial n_1}\right)_0 + \sum_i \left(\frac{\partial^2 \varepsilon_{\text{int}}}{\partial n_1 \partial n_i}\right)_0 \delta n_i, \tag{5.1}$$

$$H_2 = H_0 + \left(\frac{\partial \varepsilon_{\text{int}}}{\partial n_2}\right)_0 + \sum_i \left(\frac{\partial^2 \varepsilon_{\text{int}}}{\partial n_2 \partial n_i}\right)_0 \delta n_i, \tag{5.2}$$

$$H_3 = \left(\frac{\partial \varepsilon_{\text{int}}}{\partial n_3}\right)_0 + \sum_i \left(\frac{\partial^2 \varepsilon_{\text{int}}}{\partial n_3 \partial n_i}\right)_0 \delta n_i, \tag{5.3}$$

$$H_4 = \left(\frac{\partial \varepsilon_{\text{int}}}{\partial n_4}\right)_0 + \sum_i \left(\frac{\partial^2 \varepsilon_{\text{int}}}{\partial n_4 \partial n_i}\right)_0 \delta n_i. \tag{5.4}$$

where $H_0 = -\hbar^2 \nabla^2/(2m)$ is the free particle Hamiltonian and ε_{int} is the interaction energy density. The suffix 0 indicates that the derivatives are calculated at equilibrium, and $\delta n_{i=1,2,3,4}$ are the changes with respect to equilibrium. Indeed, if ε_{int} is the BdG (SLDA) interaction energy density functional, then $H_0 + (\partial \varepsilon_{\text{int}}/\partial n_i)_0$ is the corresponding quasiparticle Hamiltonian of BdG (SLDA) equations, while the other second-order terms play the role of a self-generated mean-field potential experienced by quasiparticles. In the following we call "reference gas" the gas described by the Hamiltonian $H_0 + (\partial \varepsilon_{\text{int}}/\partial n_i)_0$, and "real gas" the gas described by the full expression (5.1-5.4).

The dynamic response function of the system can be investigated by adding an external field V_{ext}^i to the quasi-particle Hamiltonian H_i, the linear response function

χ_{ij} is the quantity which connects the induced density fluctuations δn_i and the external field V^i_{ext} by equation $\delta n_i = \sum\limits_j \chi_{ij} V^i_{\text{ext}}$. By inserting this equation in second-order derivative terms of the quasiparticle Hamiltonian, we can define a new effective external field

$$V^i_{\text{eff}} = V^i_{\text{ext}} + \sum_j \left(\frac{\partial^2 \varepsilon_{\text{int}}}{\partial n_i \partial n_j} \right)_0 \delta n_j = V^i_{\text{ext}} + \sum_{j,l} E^I_{ij} \chi_{jl} V^l_{\text{ext}} \tag{5.5}$$

where $E^I_{ij} = (\partial^2 \varepsilon_{\text{int}} / (\partial n_i \partial n_j))_0$. We use χ^0 for the response function of the reference gas and χ for the response function of the real gas. The key result is that the dynamics of real gases in an external field V_{ext} can be treated as the dynamics of reference gases in an effective external field V_{eff}. Then, according to the definition of response function, we can write the following matrix equation

$$\begin{bmatrix} \chi_{11} & \chi_{12} & \chi_{13} & \chi_{14} \\ \chi_{21} & \chi_{22} & \chi_{23} & \chi_{24} \\ \chi_{31} & \chi_{32} & \chi_{33} & \chi_{34} \\ \chi_{41} & \chi_{42} & \chi_{43} & \chi_{44} \end{bmatrix} \begin{bmatrix} V^1_{\text{ext}} \\ V^2_{\text{ext}} \\ V^3_{\text{ext}} \\ V^4_{\text{ext}} \end{bmatrix} \equiv \begin{bmatrix} \delta n_1 \\ \delta n_2 \\ \delta n_3 \\ \delta n_4 \end{bmatrix} \equiv \begin{bmatrix} \chi^0_{11} & \chi^0_{12} & \chi^0_{13} & \chi^0_{14} \\ \chi^0_{21} & \chi^0_{22} & \chi^0_{23} & \chi^0_{24} \\ \chi^0_{31} & \chi^0_{32} & \chi^0_{33} & \chi^0_{34} \\ \chi^0_{41} & \chi^0_{42} & \chi^0_{43} & \chi^0_{44} \end{bmatrix} \begin{bmatrix} V^1_{\text{eff}} \\ V^2_{\text{eff}} \\ V^3_{\text{eff}} \\ V^4_{\text{eff}} \end{bmatrix}, \tag{5.6}$$

where the matrix form of the effective external field is

$$\begin{bmatrix} V^1_{\text{eff}} \\ V^2_{\text{eff}} \\ V^3_{\text{eff}} \\ V^4_{\text{eff}} \end{bmatrix} = \begin{bmatrix} V^1_{\text{ext}} \\ V^2_{\text{ext}} \\ V^3_{\text{ext}} \\ V^4_{\text{ext}} \end{bmatrix} + \begin{bmatrix} E^I_{11} & E^I_{12} & E^I_{13} & E^I_{14} \\ E^I_{21} & E^I_{22} & E^I_{23} & E^I_{24} \\ E^I_{31} & E^I_{32} & E^I_{33} & E^I_{34} \\ E^I_{41} & E^I_{42} & E^I_{43} & E^I_{44} \end{bmatrix} \begin{bmatrix} \chi_{11} & \chi_{12} & \chi_{13} & \chi_{14} \\ \chi_{21} & \chi_{22} & \chi_{23} & \chi_{24} \\ \chi_{31} & \chi_{32} & \chi_{33} & \chi_{34} \\ \chi_{41} & \chi_{42} & \chi_{43} & \chi_{44} \end{bmatrix} \begin{bmatrix} V^1_{\text{ext}} \\ V^2_{\text{ext}} \\ V^3_{\text{ext}} \\ V^4_{\text{ext}} \end{bmatrix}. \tag{5.7}$$

The matrix equation $\chi V_{\text{ext}} = \delta n = \chi^0 V_{\text{eff}} = \chi^0 \left(V_{\text{ext}} + E^I \chi V_{\text{ext}} \right)$ must be always satisfied by any external field V_{ext}. After some simple linear algebraic derivation we can find the relation between response functions of reference gases and real gases:

$$\chi = \frac{\chi^0}{1 - \chi^0 E^I}. \tag{5.8}$$

The only input quantity in this relation is an analytic expression of the interaction energy density functional ε_{int}.

The random phase approximation has previously been used to study the dynamic structure factor [106] and collective oscillations [107] of weakly interacting

Fermi superfluids. A dynamic mean-field approach, identical to the random phase approximation but based on kinetic equations, was developed to investigate dynamic and static structure factors [5] and collective modes [88] of a uniform, strongly interacting Fermi gas.

5.2 Dynamic structure factor in BdG theory

In the Bogoliubov-de Gennes theory, the interaction energy density functional of the superfluid fermions is

$$\varepsilon_{\text{int}} = g_{\text{eff}} n_1 n_2 + g_{\text{eff}} n_3 n_4, \tag{5.9}$$

where g_{eff} is the effective interaction strength, and $1/g_{\text{eff}} = m/(4\pi\hbar^2 a) - \sum_k m/(\hbar^2 k^2)$ is the regularization used to avoid the ultraviolet divergence. As I said in section 2.1, the normal density n_1 and n_2 is convergent, but the anomalous densities n_3 and n_4 are divergent if one used the bare delta-interaction. The regularization helps to cure this divergence by requiring $g_{\text{eff}} \to 0$, which induce that the Hartree term $g_{\text{eff}} n_1 n_2$ to do only a smaller order contribution to energy density functional than the pairing term $g_{\text{eff}} n_3 n_4$. Usually we can neglect the Hartree term and write $\varepsilon_{\text{int}} = g_{\text{eff}} n_3 n_4$. Here, for general we keep this Hartree term during the derivation (this choice does nothing influence to the final expression of dynamic structure factor, because the contribution from Hartree term just is much smaller to dynamic structure factor than that from pairing term in the BdG theory), and correspondingly the important interaction matrix E^I reads

$$E^I \equiv g_{\text{eff}} G, \quad G = \begin{bmatrix} 0 & 1 & 0 & 0 \\ 1 & 0 & 0 & 0 \\ 0 & 0 & 0 & 1 \\ 0 & 0 & 1 & 0 \end{bmatrix}. \tag{5.10}$$

we obtain the relation between the response functions of the real gas and reference gas in the BdG theory,

$$\chi = \frac{\chi^0}{1 - \chi^0 g_{\text{eff}} G}, \tag{5.11}$$

and the corresponding BdG-quasiparticle Hamiltonians are

$$H_1 = -\tfrac{\hbar^2}{2m}\nabla^2 + g_{\text{eff}} n_2, \quad H_2 = -\tfrac{\hbar^2}{2m}\nabla^2 + g_{\text{eff}} n_1, \quad H_3 = -\triangle^*, \quad H_4 = -\triangle. \tag{5.12}$$

The stationary BdG equations can be used to calculate the response function χ^0. There are 16 matrix elements inside χ^0.

$$\chi^0 \equiv \begin{bmatrix} \chi^0_{11} & \chi^0_{12} & \chi^0_{13} & \chi^0_{14} \\ \chi^0_{21} & \chi^0_{22} & \chi^0_{23} & \chi^0_{24} \\ \chi^0_{31} & \chi^0_{32} & \chi^0_{33} & \chi^0_{34} \\ \chi^0_{41} & \chi^0_{42} & \chi^0_{43} & \chi^0_{44} \end{bmatrix} \equiv \begin{bmatrix} \langle n_1 n_1 \rangle & \langle n_1 n_2 \rangle & \langle n_1 n_3 \rangle & \langle n_1 n_4 \rangle \\ \langle n_2 n_1 \rangle & \langle n_2 n_2 \rangle & \langle n_2 n_3 \rangle & \langle n_2 n_4 \rangle \\ \langle n_3 n_1 \rangle & \langle n_3 n_2 \rangle & \langle n_3 n_3 \rangle & \langle n_3 n_4 \rangle \\ \langle n_4 n_1 \rangle & \langle n_4 n_2 \rangle & \langle n_4 n_3 \rangle & \langle n_4 n_4 \rangle \end{bmatrix} \tag{5.13}$$

The derivation of these matrix elements is cumbersome. We show here, as an example, the derivation of $\chi^0_{\uparrow\uparrow} \equiv \chi^0_{11}$. According to the Wick theorem, the Matsubara retarded Green's function $\chi^0_{11}(\mathbf{r}, \mathbf{r}', \tau) = -\left\langle T_\tau \left[\hat{n}_1(\mathbf{r}, \tau)\hat{n}_1(\mathbf{r}', 0)\right]\right\rangle$ can be written as

$$\chi^0_{11}(\mathbf{r}, \mathbf{r}', \tau) = -\left\langle \Psi^\dagger_\uparrow(\mathbf{r}, \tau)\Psi_\uparrow(\mathbf{r}', 0)\right\rangle \left\langle \Psi_\uparrow(\mathbf{r}, \tau)\Psi^\dagger_\uparrow(\mathbf{r}', 0)\right\rangle \tag{5.14}$$

where τ is an imaginary time and we assume $\tau > 0$. Using the Bogoliubov transformations (2.14) for the field operators Ψ_σ and $\Psi^\dagger_\sigma$, one finds

$$\begin{aligned} \chi^0_{11}(\mathbf{r}, \mathbf{r}', \tau) &= -\tfrac{1}{2} \textstyle\sum_{i,n} \left\langle \left(u^*_{i\uparrow}(\mathbf{r}) c^\dagger_{i\uparrow} e^{E_{i\uparrow}\tau} + v_{i\downarrow}(\mathbf{r}) c_{i\downarrow} e^{-E_{i\downarrow}\tau}\right) \left(u_{n\uparrow}(\mathbf{r}') c_{n\uparrow} + v^*_{n\downarrow}(\mathbf{r}') c^\dagger_{n\downarrow}\right)\right\rangle \\ &\times \tfrac{1}{2} \textstyle\sum_{j,l} \left\langle \left(u_{j\uparrow}(\mathbf{r}) c_{j\uparrow} e^{-E_{j\uparrow}\tau} + v^*_{j\downarrow}(\mathbf{r}) c^\dagger_{j\downarrow} e^{E_{j\downarrow}\tau}\right) \left(u^*_{l\uparrow}(\mathbf{r}') c^\dagger_{l\uparrow} + v_{l\downarrow}(\mathbf{r}') c_{l\downarrow}\right)\right\rangle \end{aligned}$$

To avoid double counting, a factor of 1/2 appears in the summation during derivation.

$$\begin{aligned} \chi^0_{11}(\mathbf{r}, \mathbf{r}', \tau) &= -\tfrac{1}{4} \textstyle\sum_{i,j} \left[u^*_{i\uparrow}(\mathbf{r}) u_{i\uparrow}(\mathbf{r}') f(E_{i\uparrow}) e^{E_{i\uparrow}\tau} + v_{i\downarrow}(\mathbf{r}) v^*_{i\downarrow}(\mathbf{r}') f(-E_{i\downarrow}) e^{-E_{i\downarrow}\tau}\right] \\ &\times \left[u_{j\uparrow}(\mathbf{r}) u^*_{j\uparrow}(\mathbf{r}') f(-E_{j\uparrow}) e^{-E_{j\uparrow}\tau} + v^*_{j\downarrow}(\mathbf{r}) v_{j\downarrow}(\mathbf{r}') f(E_{j\downarrow}) e^{E_{j\downarrow}\tau}\right] \end{aligned}$$

where $\langle c^\dagger_i c_j \rangle = f(E_i)\delta_{ij}$ and $\langle c_i c^\dagger_j \rangle = f(-E_i)\delta_{ij}$, the quantity $f(x) = 1/(e^{\beta x}+1)$ is the Fermi distribution function of quasiparticle, $\beta = 1/(k_B T)$ is the inverse temperature. So that

$$\chi^0_{11}(\mathbf{r}, \mathbf{r}', \tau) = -\sum_{i,j} u^*_i(\mathbf{r}) u_i(\mathbf{r}') u_j(\mathbf{r}) u^*_j(\mathbf{r}') f(E_i) f(-E_j) e^{(E_i - E_j)\tau}, \tag{5.15}$$

where the spin index has been removed thanks to the spin-up and spin-down correspondence in Eqs. (2.7) and (2.8). By means of the Fourier transformation, $\chi^0_{11}(\mathbf{r}, \mathbf{r}', \omega_n) = \int_0^\beta d\tau e^{i\omega_n \tau} \chi^0_{11}(\mathbf{r}, \mathbf{r}', \tau)$, the above equation becomes

$$\chi^0_{11}(\mathbf{r}, \mathbf{r}', \omega_n) = \sum_{i,j} u^*_i(\mathbf{r}) u_i(\mathbf{r}') u_j(\mathbf{r}) u^*_j(\mathbf{r}') \frac{f(E_i) - f(E_j)}{i\omega_n + (E_i - E_j)} \tag{5.16}$$

where $\omega_n = 2n\pi/\beta$ is the bosonic Matsubara frequency.

For the homogeneous gas, a set of plane wave functions can be used to expand the eigenfunctions u_i in the form $u_i(\mathbf{r}) \to u_k e^{i\mathbf{kr}}$. By defining momentum transfer $\mathbf{p} = \mathbf{k}' - \mathbf{k}$ and relative coordinate $\Delta\mathbf{r} = \mathbf{r} - \mathbf{r}'$, then

$$\chi^0_{11}(\Delta\mathbf{r}, \omega_n) = \sum_{k,p} u^*_k u_k u_{k+p} u^*_{k+p} e^{i\mathbf{p}\Delta\mathbf{r}} \frac{f(E_k) - f(E_{k+p})}{i\omega_n + (E_k - E_{k+p})} \tag{5.17}$$

and using the Fourier transformation $\chi^0_{11}(q, \omega_n) = \int d\Delta\mathbf{r}\chi^0_{11}(\Delta\mathbf{r}, i\omega_n)e^{-i\mathbf{q}\Delta\mathbf{r}}$, we get

$$\chi^0_{11}(q, \omega_n) = \sum_{k} u^*_k u_k u_{k+q} u^*_{k+q} \frac{f(E_k) - f(E_{k+q})}{i\omega_n + (E_k - E_{k+q})} \tag{5.18}$$

Using the eigenfunction solutions of the Bogoliubov quasiparticle (2.13) from stationary BdG equations (2.12) of the homogeneous Fermi gases, finally we obtain

$$\begin{aligned} \chi^0_{11}(q, \omega_n) &= \textstyle\sum_k \frac{1}{2}\left(1 + \frac{\xi_k\xi_{k+q}}{E_kE_{k+q}}\right)\left[f(E_k) - f(E_{k+q})\right]\frac{1}{i\omega_n + (E_k - E_{k+q})} \\ &+ \textstyle\sum_k \frac{1}{2}\left(1 - \frac{\xi_k\xi_{k+q}}{E_kE_{k+q}}\right)\left[1 - f(E_k) - f(E_{k+q})\right]\frac{E_k + E_{k+q}}{(i\omega_n)^2 - (E_k + E_{k+q})^2} \end{aligned} \tag{5.19}$$

With similar procedures, we can get the other 15 elements of the reference response function χ^0. In fact, after considering all symmetries of these 16 matrix elements, one finds that only 6 of them are independent. One of the most important symmetry is the correspondence $\mathbf{k} \to -\mathbf{k} - \mathbf{q}$ (ξ_k and E_k are just the functions of the mode of k). Ultimately the response function of reference gases has the following expression

$$\chi^0 = \begin{bmatrix} a & b & c^* & c \\ b & a & c^* & c \\ c & c & -b & h^* \\ c^* & c^* & h & -b \end{bmatrix}, \tag{5.20}$$

the dimensions of each matrix elements of χ^0 are all N/E_F. The dimensionless expressions of all 6 independent matrix elements (a, b, c, c^*, h and h^*), which read

$$\begin{aligned} a &= a_1 + a_2, & b &= b_1 + b_2, \\ c &= (c_1 + c_2) + (c_3 + c_4), & c^* &= (c_1 + c_2) - (c_3 + c_4), \\ h &= (h_1 + h_2) + (h_3 + h_4), & h^* &= (h_1 + h_2) - (h_3 + h_4). \end{aligned} \tag{5.21}$$

a_1, a_2, b_1, b_2, c_1, c_2, c_3, c_4, h_1, h_2, h_3 and h_4 are 12 integration equations, their expressions are given in the following table

Label	Expression
a_1	$+\frac{3}{4}\int dkd\theta k^2\sin\theta\frac{1}{2}\left(1+\frac{\xi_k\xi_{k+q}}{E_kE_{k+q}}\right)[f(E_k)-f(E_{k+q})]\frac{1}{i\omega_n+(E_k-E_{k+q})}$
a_2	$+\frac{3}{4}\int dkd\theta k^2\sin\theta\frac{1}{2}\left(1-\frac{\xi_k\xi_{k+q}}{E_kE_{k+q}}\right)[1-f(E_k)-f(E_{k+q})]\frac{E_k+E_{k+q}}{(i\omega_n)^2-(E_k+E_{k+q})^2}$
b_1	$-\frac{3}{4}\int dkd\theta k^2\sin\theta\frac{1}{2}\frac{\triangle^2}{E_kE_{k+q}}[f(E_k)-f(E_{k+q})]\frac{1}{i\omega_n+(E_k-E_{k+q})}$
b_2	$+\frac{3}{4}\int dkd\theta k^2\sin\theta\frac{1}{2}\frac{\triangle^2}{E_kE_{k+q}}[1-f(E_k)-f(E_{k+q})]\frac{E_k+E_{k+q}}{(i\omega_n)^2-(E_k+E_{k+q})^2}$
c_1	$-\frac{3}{4}\int dkd\theta k^2\sin\theta\frac{1}{4}\left(\frac{\xi_k\triangle}{E_kE_{k+q}}+\frac{\triangle\xi_{k+q}}{E_kE_{k+q}}\right)[f(E_k)-f(E_{k+q})]\frac{1}{i\omega_n+(E_k-E_{k+q})}$
c_2	$+\frac{3}{4}\int dkd\theta k^2\sin\theta\frac{1}{4}\left(\frac{\xi_k\triangle}{E_kE_{k+q}}+\frac{\triangle\xi_{k+q}}{E_kE_{k+q}}\right)[1-f(E_k)-f(E_{k+q})]\frac{E_k+E_{k+q}}{(i\omega_n)^2-(E_k+E_{k+q})^2}$
c_3	$-\frac{3}{4}\int dkd\theta k^2\sin\theta\frac{1}{4}\left(\frac{\triangle}{E_k}-\frac{\triangle}{E_{k+q}}\right)[f(E_k)-f(E_{k+q})]\frac{1}{i\omega_n+(E_k-E_{k+q})}$
c_4	$+\frac{3}{4}\int dkd\theta k^2\sin\theta\frac{1}{4}\left(\frac{\triangle}{E_k}+\frac{\triangle}{E_{k+q}}\right)[1-f(E_k)-f(E_{k+q})]\frac{i\omega_n}{(i\omega_n)^2-(E_k+E_{k+q})^2}$
h_1	$+\frac{3}{4}\int dkd\theta k^2\sin\theta\frac{1}{2}\left(1-\frac{\xi_k}{E_k}\frac{\xi_{k+q}}{E_{k+q}}\right)[f(E_k)-f(E_{k+q})]\frac{1}{i\omega_n+(E_k-E_{k+q})}$
h_2	$+\frac{3}{4}\int dkd\theta k^2\sin\theta\frac{1}{2}\left(1+\frac{\xi_k}{E_k}\frac{\xi_{k+q}}{E_{k+q}}\right)[1-f(E_k)-f(E_{k+q})]\frac{E_k+E_{k+q}}{(i\omega_n)^2-(E_k+E_{k+q})^2}$
h_3	$+\frac{3}{4}\int dkd\theta k^2\sin\theta\frac{1}{2}\left(\frac{\xi_k}{E_k}-\frac{\xi_{k+q}}{E_{k+q}}\right)[f(E_k)-f(E_{k+q})]\frac{1}{i\omega_n+(E_k-E_{k+q})}$
h_4	$-\frac{3}{4}\int dkd\theta k^2\sin\theta\frac{1}{2}\left(\frac{\xi_k}{E_k}+\frac{\xi_{k+q}}{E_{k+q}}\right)[1-f(E_k)-f(E_{k+q})]\frac{i\omega_n}{(i\omega_n)^2-(E_k+E_{k+q})^2}$

where $n = n_1 + n_2$, $\xi_k = \hbar^2k^2/(2m) - \mu$ and $E_k = \sqrt{\xi_k^2 + \triangle^2}$. All equations in the upper table are expressed in units of N/E_F. At zero temperature, since Fermi distribution function $f(E_k) = 0$, a_1, b_1, c_1, c_3, h_1 and h_3 are all equal to zero. Also notice that h_2 is divergent because of the divergence of pairing fluctuation; we can cure this divergence by regularization procedure $h_2^r = h_2 - 1/g_{\text{eff}}$, which produces the new convergent expressions $h_r = (h_1 + h_2^r) + (h_3 + h_4)$ and $h_r^* = (h_1 + h_2^r) - (h_3 + h_4)$.

According to the definitions of density response function $\chi_D = 2(\chi_{11} + \chi_{12})$ and spin response function $\chi_S = 2(\chi_{11} - \chi_{12})$ for the balanced two-component Fermi gas, Eq. (5.11) gives

$$\chi_D = 2(a+b) - 4\frac{c^2h_r + c^{*2}h_r^* + 2bcc^*}{h_rh_r^* - b^2}. \tag{5.22}$$

$$\chi_S = 2(a-b). \tag{5.23}$$

A different derivation of the response function, based on the use of kinetic equations, was previously given by R. Combescot and collaborators [5, 88]. The expressions of

I, I', I'', I_{11}, I_{12} and I_{22} entering the density-density response function of [5, 88] are related to our expressions with the following relations

$$\begin{array}{lll} 4\pi^2 h_4 = \omega \mathrm{I}_{12}, & 4\pi^2(h_2^r + b_2) = -\mathrm{I}_{11}, & 4\pi^2(h_2^r - b_2) = -\mathrm{I}_{22}, \\ 4\pi^2 c_2 = -\frac{\triangle}{2}\mathrm{I}, & 4\pi^2 c_4 = -\frac{\triangle\omega}{2}\mathrm{I}', & 4\pi^2(a_2 + b_2) = -\mathrm{I}''. \end{array} \tag{5.24}$$

The density dynamic structure factor $S(q,\omega)$ is related to the imaginary part of the density response function via the fluctuation-dissipation theorem

$$S(q,\omega) = -\frac{1}{\pi}\frac{1}{1-e^{-\beta\omega}}\mathrm{Im}\chi\left(q, i\omega_n \to \omega + i0^+\right). \tag{5.25}$$

The same relation applies for the spin dynamic structure factor $S_S(q,\omega)$ in terms of the spin response function χ_S. In Figs 5.1 we report a few examples of our calculations of $S(q,\omega)$ and $S_S(q,\omega)$ for a uniform Fermi gas. As in [5] we show the results for uniform Fermi gas $q = 3k_F$ and for different values of the interaction strength $1/(k_F a) = 2, 1, 0, -1$. Our results agree well with those of [5], and we use this agreement as a test of our numerical predictions. The top left panel shows a single peak associated to a low energy bosonic collective excitation (phonon-like) in the BEC regime. In the top right panel one also sees a high energy tail above the threshold for pair-breakings. In the bottom left panel the low-lying peak, associated to the bosonic molecular (or dimer) degrees of freedom (molecular peak), overlaps with the single quasiparticle peak (atomic peak), which eventually dominates the dynamic structure factor in the bottom right panel. More discussions about the shape of the dynamic structure factor will be given in the next section.

The density dynamic structure factor satisfies the famous f-sum rule $\int d\omega\omega S(q,\omega) = Nq^2/(2m)$, and when do the integral to $S(q,\omega)$ over all possible ω, one can get the static structure factor $S(q) = \hbar\int d\omega S(q,\omega)$, which is intimately connected to the universal Tan's contact $\mathcal{I}$ [70, 71, 72] at high momentum transfer q via

$$\frac{\mathcal{I}}{Nk_F} = \frac{4q}{k_F}\left[\frac{S(q)-1}{1-4/(\pi q a)}\right] \tag{5.26}$$

where a is the s-wave scattering length. To date, the value given by the two-photon Bragg scattering experiment is $\mathcal{I}/(Nk_F) = 3.06 \pm 0.08$ [108], while QMC and BdG theory give $\mathcal{I}/(Nk_F) = 3.4$.

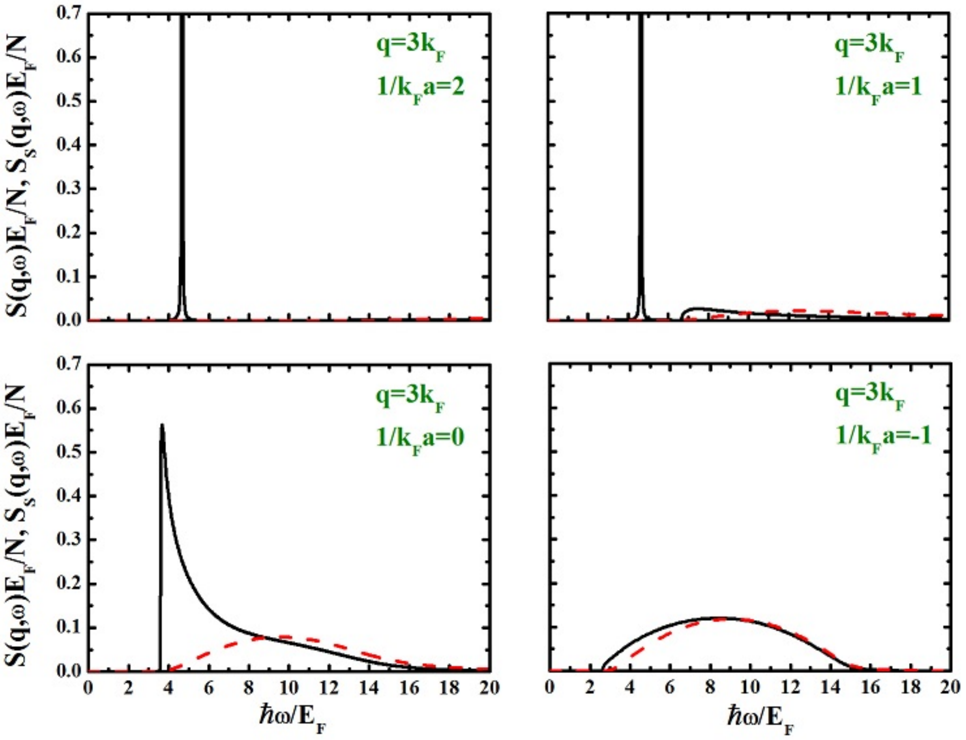

Figure 5.1: Dynamic structure factor, from BdG+RPA theory as a function of ω for fixed momentum transfer $q = 3k_F$ and for various interaction strength. Black solid lines (red dashed lines) refer to the density dynamic structure factor $S(q, \omega)$ (spin dynamic structure factor $S_S(q, \omega)$). The results almost coincide with those of [5]. The dynamic structure factor is given in units of N/E_F.

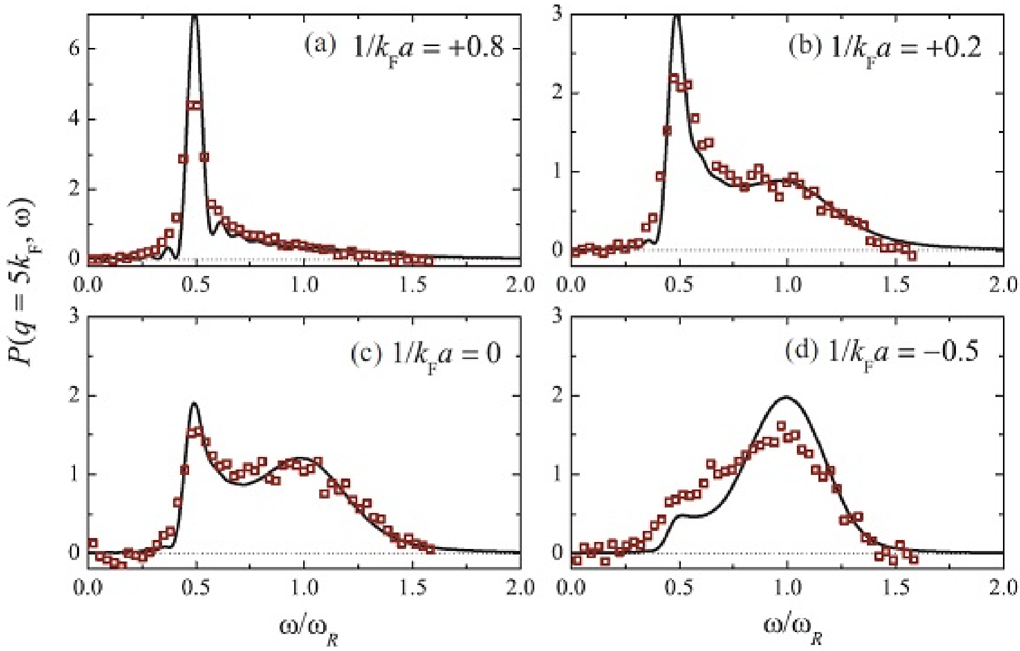

Figure 5.2: Comparison of theoretical and experimental results for the quantity $P(q, \omega)$ defined in 5.27 and measured by means of Bragg scattering. The LDA+RPA+BdG predictions (lines) agree reasonably well with the experimental data (empty squares) in the BCS-BEC crossover. The theoretical curves have no free parameters. The spectrum is normalized so that the area below the curve is unity. The frequency is measured in units of the recoil energy of the atoms. Taken from [6].

For superfluid fermions in a harmonic trap, a LDA+RPA+BdG strategy has already been utilized to calculate the dynamic structure factor [6], as displayed in Fig. 5.2, for a large momentum transfer $q = 5k_F$, this theoretical prediction of dynamic structure factor quantitatively agrees well with two-photon Bragg scattering experiment during the BEC-unitary regime, and worse in the BCS regime. For comparison with experiment, a convolution of $S(q,\omega)$ below

$$P(q,\omega) \propto \frac{1}{\pi}\int_{-\infty}^{\infty} d\omega' S(q,\omega')\mathrm{sinc}^2\left[\frac{\omega-\omega'}{\sigma}\right] \tag{5.27}$$

is required, where $\mathrm{sinc}(x) = \sin(x)/x$ and the energy resolution $\sigma = 2\tau_{Br}$ is set by the experimental Bragg pulse duration ($\tau_{Br} = 40\mu s$). We find $\sigma \approx 0.68E_F \approx 0.27\omega_R$, where recoil energy $\omega_R = \hbar q^2/(2m)$. The static structure factor of this LDA+RPA+BdG strategy again quantitatively agree with both experiment and Tan's relations. This is a surprising results.

5.3 Dynamic structure factor in SLDA theory

The same derivation of linear response function and the dynamic structure factor given in the section 5.1 and 5.2, can be straightforwardly repeated for SLDA instead of BdG. The key difference is the form of the energy density functional to start with. The expression of SLDA interaction energy density functional for a uniform unitary gas is

$$\varepsilon_{\mathrm{int}} = \beta\frac{\hbar^2 3(3\pi^2)^{2/3}}{10m}n^{5/3} + g_{\mathrm{eff}}n_3n_4, \tag{5.28}$$

with

$$\frac{1}{g_{\mathrm{eff}}} = \frac{mn^{1/3}}{\hbar^2\gamma} - \sum_k \frac{m}{\alpha\hbar^2k^2}. \tag{5.29}$$

where $n = n_1 + n_2$ is the total density. Differently from the BdG theory, here the effective interaction strength g_{eff} is a function of the total density. The corresponding second-order interaction matrix E^I which contains the second-order derivative of $\varepsilon_{\mathrm{int}}$ include also the coupling terms (t and t^*) between normal atomic density and anomalous Cooper-pair density. The matrix is

$$E^I = \begin{bmatrix} d & d & t^* & t \\ d & d & t^* & t \\ t^* & t^* & 0 & g_{\text{eff}} \\ t & t & g_{\text{eff}} & 0 \end{bmatrix} \tag{5.30}$$

where $d = 2\beta E_F/(3N) + (3\pi^2)^{2/3}|\Delta|^2/(9\gamma E_F N)$, $t = g_{\text{eff}}(3\pi^2)^{2/3}\Delta/(6\gamma E_F)$ and $t^* = g_{\text{eff}}(3\pi^2)^{2/3}\Delta^*/(6\gamma E_F)$. Another difference with respect to BdG is the matrix element d related to normal density, changed from a small number g_{eff} (or 0) to a finite order of E_F/N. Since n_3, n_4, t and Δ are all related to the quasipartitle amplitude u_k and v_k, both of which are real numbers when solving the stationary SLDA equations (4.20). So one can find that all physical quantities are real numbers, namely $n_3 = n_4$, $t = t^*$ and $\Delta = \Delta^*$.

At first order we find the quasiparticle Hamiltonians

$$H_1 = H_2 = -\alpha\tfrac{\hbar^2}{2m}\nabla^2 + \beta E_F - \tfrac{(3\pi^2)^{2/3}|\Delta|^2}{6\gamma E_F}, \quad H_3 = -\Delta^*, \quad H_4 = -\Delta. \tag{5.31}$$

which are just the quasiparticle Hamiltonians of SLDA equations. We can also get the SLDA response function for the reference gas χ^0 by solving the stationary SLDA equations (4.20). The actual expression of χ^0 is the same as in (5.20) for BdG with the same coefficient a, b, c, c^*, h and h^*, as in section 5.2. The expressions of the matrix elements are similar to the ones in BdG theory, but with $\xi_k = \alpha\hbar^2k^2/(2m) + \left(\beta - (3\pi^2)^{2/3}\eta^2/(6\gamma) - \xi_s\right)E_F$ and $E_k = \sqrt{\xi_k^2 + \Delta^2}$.

Using equation (5.8), one can obtain the response function of the real gases χ by solving the following matrix equation

$$G \begin{bmatrix} \chi_{11} & \chi_{12} \\ \chi_{21} & \chi_{22} \\ \chi_{31} & \chi_{32} \\ \chi_{41} & \chi_{42} \end{bmatrix} = \begin{bmatrix} a & b \\ b & a \\ c & c \\ c^* & c^* \end{bmatrix}, \tag{5.32}$$

where $G \equiv 1 - \chi^0 E^I$. After some simple algebraic derivations, we obtain the response of function of real gas:

$$\chi_{11} = \begin{vmatrix} a & -(a+b)d-(c^*+c)t & -(a+b)t-cg_{\text{eff}} & -(a+b)t-c^*g_{\text{eff}} \\ b & 1-(b+a)d-(c^*+c)t & -(b+a)t-cg_{\text{eff}} & -(b+a)t-c^*g_{\text{eff}} \\ c & -2cd-(-b+h^*)t & 1-2ct-h^*g_{\text{eff}} & -2ct+bg_{\text{eff}} \\ c^* & -2c^*d-(h-b)t & -2c^*t+bg_{\text{eff}} & 1-2c^*t-hg_{\text{eff}} \end{vmatrix} /|G| \tag{5.33}$$

$$\chi_{22} = \begin{vmatrix} 1-(a+b)d-(c^*+c)t & b & -(a+b)t-cg_{\text{eff}} & -(a+b)t-c^*g_{\text{eff}} \\ -(b+a)d-(c^*+c)t & a & -(b+a)t-cg_{\text{eff}} & -(b+a)t-c^*g_{\text{eff}} \\ -2cd-(-b+h^*)t & c & 1-2ct-h^*g_{\text{eff}} & -2ct+bg_{\text{eff}} \\ -2c^*d-(h-b)t & c^* & -2c^*t+bg_{\text{eff}} & 1-2c^*t-hg_{\text{eff}} \end{vmatrix} /|G| \tag{5.34}$$

$$\chi_{12} = \begin{vmatrix} b & -(a+b)d-(c^*+c)t & -(a+b)t-cg_{\text{eff}} & -(a+b)t-c^*g_{\text{eff}} \\ a & 1-(b+a)d-(c^*+c)t & -(b+a)t-cg_{\text{eff}} & -(b+a)t-c^*g_{\text{eff}} \\ c & -2cd-(-b+h^*)t & 1-2ct-h^*g_{\text{eff}} & -2ct+bg_{\text{eff}} \\ c^* & -2c^*d-(h-b)t & -2c^*t+bg_{\text{eff}} & 1-2c^*t-hg_{\text{eff}} \end{vmatrix} /|G| \tag{5.35}$$

$$\chi_{21} = \begin{vmatrix} 1-(a+b)d-(c^*+c)t & a & -(a+b)t-cg_{\text{eff}} & -(a+b)t-c^*g_{\text{eff}} \\ -(b+a)d-(c^*+c)t & b & -(b+a)t-cg_{\text{eff}} & -(b+a)t-c^*g_{\text{eff}} \\ -2cd-(-b+h^*)t & c & 1-2ct-h^*g_{\text{eff}} & -2ct+bg_{\text{eff}} \\ -2c^*d-(h-b)t & c^* & -2c^*t+bg_{\text{eff}} & 1-2c^*t-hg_{\text{eff}} \end{vmatrix} /|G| \tag{5.36}$$

We can obtain all matrix elements of χ with similar derivation. However, χ_{11}, χ_{12}, χ_{21} and χ_{22} are enough to calculate the density and spin response function. In fact, for two-component Fermi gases with equal spin components, one has $\chi_{11} = \chi_{22}$ and $\chi_{21} = \chi_{12}$. With the definition of density response function $\chi_D = 2(\chi_{11} + \chi_{12})$, we obtain

$$\chi_D = 2 \begin{vmatrix} b+a & -cg_{\text{eff}} & -c^*g_{\text{eff}} \\ 2c & 1-h^*g_{\text{eff}} & bg_{\text{eff}} \\ 2c^* & bg_{\text{eff}} & 1-hg_{\text{eff}} \end{vmatrix} /|G|, \tag{5.37}$$

As already done for BdG, we introduce the new functions $h_r = (h_1+h_2^r)+(h_3+h_4)$ and $h_r^* = (h_1+h_2^r)-(h_3+h_4)$, with $h_2^r = h_2 - 1/g_{\text{eff}}$. Finally we find

$$\chi_D = 2g_{\text{eff}}^2 \left[(a+b)\left(h_r h_r^* - b^2\right) - 2\left(c^2 h_r + c^{*2} h_r^* + 2bcc^*\right)\right]/|G| \tag{5.38}$$

and

$$
\begin{aligned}
|G| =& 4tg_{\text{eff}}\left(bc^* + ch_r + bc + c^* h_r^*\right) + 2t^2\left[-2(c^* - c)^2 + (h_r^* + h_r + 2b)(b + a)\right] \\
&+ (2dg_{\text{eff}}^2 - 4t^2 g_{\text{eff}})\left[-(b + a)(h_r h_r^* - b^2) + 2(c^2 h_r + 2cc^* b + c^{*2} h_r^*)\right] \\
&+ g_{\text{eff}}\left(h_r^* h_r - b^2\right)
\end{aligned}
\tag{5.39}
$$

One should pay attention to the order of t, d and g_{eff} (g_{eff} is a small number): d is has the order of $[g_{\text{eff}}]^0$, while t and g_{eff} the order of $[g_{\text{eff}}]^1$. Inside the determinant of $|G|$, most terms are of order $[g_{\text{eff}}]^2$, except $4t^2 g_{\text{eff}}$ whose order is $[g_{\text{eff}}]^3$ which can be neglected. So finally

$$
\begin{aligned}
|G| = \;& 4tg_{\text{eff}}\left(bc^* + ch_r + bc + c^* h_r^*\right) + 2t^2\left[-2\left(c^* - c\right)^2 + \left(h_r^* + h_r + 2b\right)\left(b + a\right)\right] \\
&+ 2dg_{\text{eff}}^2\left[-\left(b + a\right)\left(h_r h_r^* - b^2\right) + 2\left(c^2 h_r + 2cc^* b + c^{*2} h_r^*\right)\right] + g_{\text{eff}}^2\left(h_r h_r^* - b^2\right)
\end{aligned}
\tag{5.40}
$$

At this point, it is worth noticing that the BdG results for the response function can be straightforward recovered by setting $t = 0$ and $d = 0$, and the $|G|$ will be recovered into the result of BdG+RPA, $g_{\text{eff}}^2(h_r h_r^* - b^2)$. For simple, we do dimensionless treatment to all physical quantities, then we have $d = 2\beta/3 + (3\pi^2)^{2/3}\eta^2/(9\gamma)$, $t = g_{\text{eff}}(3\pi^2)^{2/3}\eta/(6\gamma)$, and $\eta = \Delta/E_F$. Also we obtain an dimensionless expression of the density response function

$$
\chi_D = 2\left[(a + b)(h_r h_r^* - b^2) - 2(c^2 h_r + c^{*2} h_r^* + 2bcc^*)\right]/|\widetilde{G}|
\tag{5.41}
$$

with

$$
\begin{aligned}
|\widetilde{G}| = \frac{|G|}{g_{\text{eff}}^2} =& \frac{2(3\pi^2)^{2/3}}{3\gamma}\eta\left(bc^* + ch_r + bc + c^* h_r^*\right) + \left(h_r h_r^* - b^2\right) \\
&+ \frac{(3\pi^2)^{4/3}}{18\gamma^2}\eta^2\left[-2(c^* - c)^2 + (h_r^* + h_r + 2b)(b + a)\right] \\
&+ \left(\frac{4\beta}{3} + \frac{2(3\pi^2)^{2/3}}{9\gamma}\eta^2\right)\left[-(b + a)(h_r h_r^* - b^2)2(c^2 h_r + 2cc^* b + c^{*2} h_r^*)\right]
\end{aligned}
\tag{5.42}
$$

Also with the definition of spin response function $\chi_S = 2(\chi_{11} - \chi_{12})$, we get the expression

$$
\chi_S = 2(a - b).
\tag{5.43}
$$

The dynamic structure factor is related to the imaginary part of the density-density response function via the fluctuation-dissipation theorem, as in Eq. (5.25). By this equation, we calculate the dynamic structure factor at both zero temperature and finite temperature.

At small momentum transfer $q \to 0$, the first sound speed c_s can be obtained at the peak position of dynamic structure factor ($\widetilde{G}$=0), where energy transfer is also very small $\omega \to 0$. After dimensionless treatment to all relative quantities, one get the dimensionless expression for c_s

$$\begin{aligned} \frac{c_s}{v_F} = \frac{\widetilde{\omega}}{2\sqrt{\alpha}\widetilde{q}} = & \sqrt{\frac{\alpha\eta\widetilde{J_4}}{3}\left[\frac{(1-F^2)\eta\widetilde{J_2}-2F\widetilde{J_\xi}}{\eta^2\widetilde{J_2}^2+\widetilde{J_\xi}^2}+(\beta+F\eta/2)\eta\right]} \\ = & \sqrt{\frac{\alpha\eta\widetilde{J_4}}{3}\left[\frac{(1-F^2)\eta\widetilde{J_2}-2F\widetilde{J_\xi}}{\eta^2\widetilde{J_2}^2+\widetilde{J_\xi}^2}\right]+\frac{(\beta+F\eta/2)}{3}} \end{aligned} \tag{5.44}$$

where $F = (3\pi^2)^{2/3}\eta/(3\gamma)$ and $\alpha\eta^2\widetilde{J}_4 = 1$,

$$\begin{array}{lll} 2\pi^2 a_2 = -\frac{\triangle^2}{4}J_2, & 2\pi^2 b_2 = -\frac{\triangle^2}{4}J_2, & 2\pi^2 c_2 = -\frac{\triangle}{4}J_\xi, \\ 2\pi^2 c_4 = -\frac{\triangle\omega}{4}J_2, & 2\pi^2 h_2^r = -\frac{\omega^2-2\triangle^2}{8}J_2+\alpha^2\frac{q^2}{24m^2}J_4, & 2\pi^2 h_4 = -\frac{\omega}{4}J_\xi. \end{array} \tag{5.45}$$

and the unit of first sound speed is $v_F = 2E_F/(\hbar k_F)$, v_F is the Fermi velocity.

5.4 Results

In the following, we present some results for the dynamic structure factor of unitary fermions with SLDA. A typical case is shown in Fig. 5.3. In the left panel we report $S(q,\omega)$ in the momentum range from 0 to $2k_F$. In the right panel we show the profile of the same function at $q = 1k_F$. In this low-q regime, the main structures visible in $S(q,\omega)$ are a low energy narrow peak, starting from zero energy with an almost linear dispersion, and a broader distribution at higher energy, above an almost horizontal threshold. The lowest excitation mode is a phononic branch, whose slope at $\omega \to 0$ is the sound speed. By fitting the position of the phononic peak as a function fo q we numerically extract the value $c_s = 0.35v_F$, which coincides, within the accuracy of the calculation, with the value obtained by the analytic expression (5.44), as well as with the value that can be obtained by solving the equations for the density (6.1) and

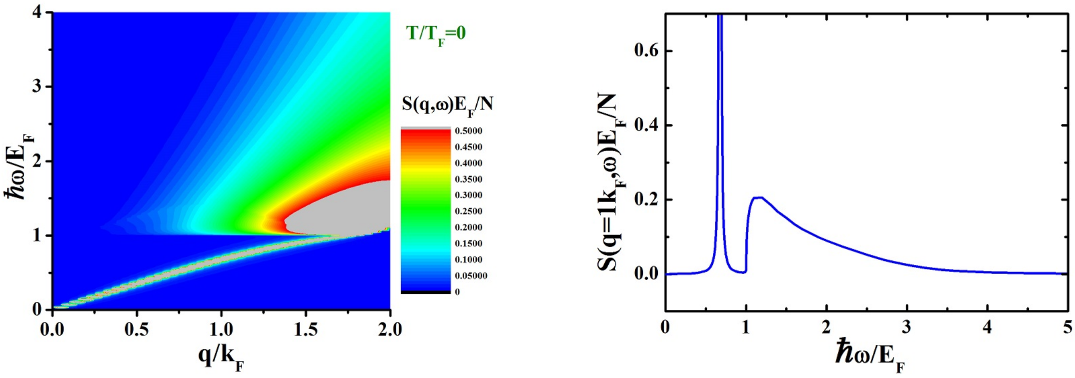

Figure 5.3: The color-plot (left) shows the dynamic structure factor for momentum transfer q in the range from 0 to $2k_F$ obtained with RPA calculations based on SLDA. The slope of the low energy branch corresponds to the sound speed $c_s = 0.35v_F$, while the horizontal threshold at $\omega = 1.0E_F/\hbar$ is equal to the minimum energy 2Δ to break a Cooper-pair. The same $S(q, \omega)$ for $q01k_F$ is plotted in the right panel.

order parameter (6.2) and using the definition of sound speed $c_s = \sqrt{(n/m)\partial\mu/\partial n}$. This value also coincides with the value extracted from experiments and from Monte Carlo ab initio calculations. This agreement is not surprising, since the parameters of SLDA have been chosen to reproduce known results, including the equation of state and hence the sound speed. It is worth noticing that the same phononic peak is also found in $S(q, \omega)$ with the same formalism but using the BdG energy density functional. However, in the BdG case sound speed is $c_s = 0.443v_F$, which is about 30% larger. A comparison between the phonon peaks in BdG and SLDA at a much lower value of q is shown in Fig. 5.4. The general structure of $S(q, \omega)$ in BdG theory has been presented for instance in [88].

The horizontal threshold is located at $\omega = 2\Delta = 1.0E_F$, which corresponds to the minimum energy transfer to activate pair-breaking. The broad peak above this energy thus include single quasi-particle excitations. This also tell us that the measurement of $S(q, \omega)$ in two-photon Bragg scattering experiments can give direct information on the gap, which characterizes the BCS superfluidity.

By integrating the dynamic structure factor in ω one obtains the static structure factor $S(q)$. Our results are shown in Fig. 5.5. The blue solid line represents the

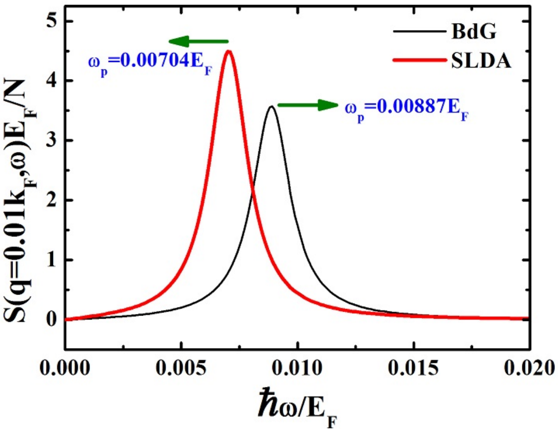

Figure 5.4: The phononic peak of the dynamic structure factor is shown in the low-q limit. The red solid line is the SLDA result and the black solid line is the BdG result.

SLDA+RPA prediction. The figure shows the comparison with Quantum Monte Carlo [5] (black dotted line) and with the BdG theory (red dashed line). Another interesting relation is the f-sum rule

$$\int d\omega\ \omega S(q,\omega) = \frac{Nq^2}{2m}. \tag{5.46}$$

We have numerically checked that SLDA+RPA satisfy this sum rule within 1% of accuracy.

For high momentum transfer q, one can investigate both the Cooper-pair excitations (bosonic) and the single atom excitations (fermionic), which typically produce a two-peak structure in the density dynamic structure factor. An example is given in Fig. 5.6. Experimentally, the dynamic structure factor was firstly measured at high momentum transfer q, in a range from $3.8k_F$ to $5k_F$ [9]. Theoretically the predictions for the dynamic and static structure factor from a mean-field BdG+RPA scheme agree quantitatively well with the results of two-photons Bragg scattering experiment (Fig. 1.3). However, to our disappointment, SLDA+RPA scheme predicts a quite lower molecular peak at momentum transfer $q = 4k_F$ than BdG+PRA. It seems that SLDA theory underestimates the contribution from molecular Cooper pairs and can not give a right description at high momentum transfer q. This is

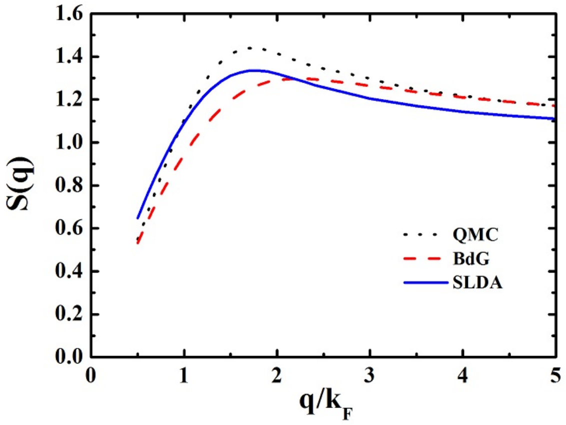

Figure 5.5: Static structure factor of superfluid unitary fermions at zero temperature calculated by SLDA+RPA theory (blue solid line), compared with the results of Quantum Monte Carlo (black dotted line) [5] and BdG+RPA (red dashed line) theory.

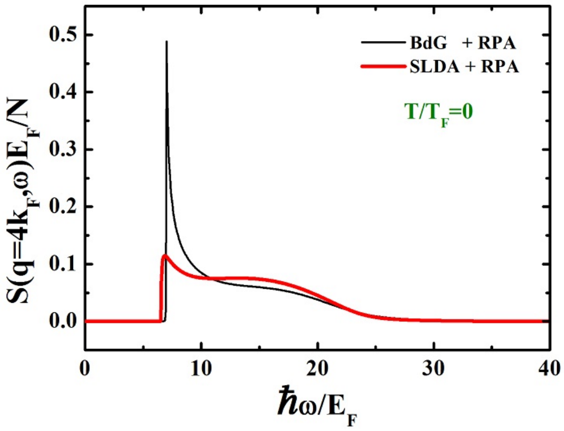

Figure 5.6: Dynamic structure factor for a relatively large momentum transfer ($q = 4k_F$) calculated by both SLDA+PRA theory (red line) and BdG+RPA theory (black line).

consistent with the behavior of the static structure factor in Fig. 5.5, where one clearly sees that the $S(q)$ of SLDA is systematically lower than BdG and QMC at high q.

Chapter 6

SLDA at finite temperature

In this chapter, we focus our discussion on the Superfluid Local Density Approximation at finite temperature. Since SLDA includes the Hartree term for the interaction among unpaired atoms, it can be used to describe also an interacting normal gas when the temperature is above the critical temperature T_c. So SLDA is expected to give better results than BdG theory at finite temperature. We first discuss the behavior of the chemical potential $\mu(T)$ and order parameter $\Delta(T)$ at finite temperature, where experimental data on the equation of state exist [8], and then we calculate the dynamic structure factor.

6.1 $\mu(T)$ and $\Delta(T)$

The BdG theory for superfluid fermions in the BCS-BEC crossover is expected to be only qualitatively reliable at zero temperature. Especially, BdG's predictions get worse for T of the order of, or larger than T_c, when the particles inside the normal gases should still interact with each other, but in BdG theory the system is treated as an ideal Fermi gas. Conversely, because of the existence of the Hartree term in the energy density function (4.14), SLDA can predict an interacting normal gas, which is a big improvement. So it is reasonable to expect that SLDA provides a better performance than BdG theory. In section 4.3, we have already introduce the basic idea of SLDA. In this section, we will extend it to finite temperature.

We know that there are three dimensionless parameters α, β and γ in the SLDA

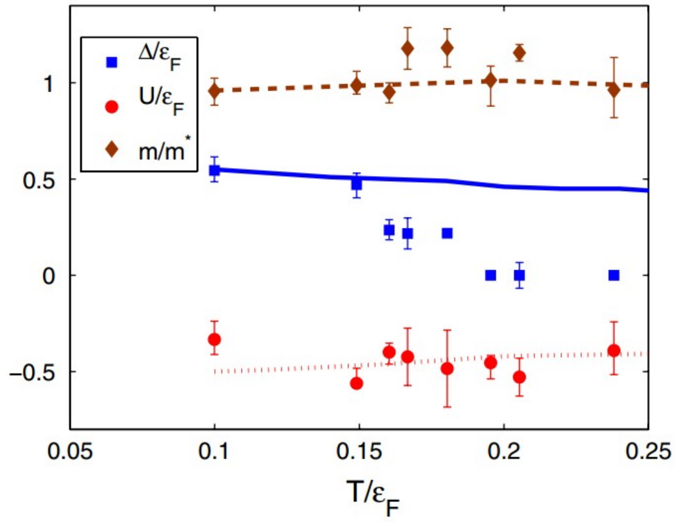

Figure 6.1: Order parameter (squares), mean-field interaction energy (circles) and effective mass (diamonds) of a unitary Fermi gas at finite temperature calculated with a Quantum Monte Carlo technique in [7]. The solid, dotted, and dashed lines are the same quantities calculated within an independent quasiparticle model. Taken from [7].

equations (4.20). In order to extend the theory to finite temperature, the first question is whether these parameters can be kept constant or they are temperature dependent. Luckily, Quantum Monte Carlo results are already available [7], and we can use them as a guide (see Fig. 6.1). The QMC results for the effective mass parameter $\alpha = m/m^*$ seem to indicate that α is almost T-independent and always of order 1. So, in the following we just assume $\alpha = 1$ at any temperature. The parameter β of SLDA is related to the to mean-field potential U/E_F which, again, seems to be almost T-independent and we take $\beta(T) = \beta(T = 0)$. Finally the pairing parameter γ is related to order parameter Δ/E_F. As shown in Fig. 6.1 the quantity Δ/E_F is almost constant at low temperature and then it decreases to zero above $\sim 0.2T_F$. The relation between Δ/E_F and the parameter γ of SLDA is however rather nontrivial. In fact, SLDA is known to ignore possible pseudogap effects which are instead included in Monte Carlo calculations. Adding the pseudogap physics to SLDA would be a big challenge. So, for simplicity, let us assume, in first approximation, that also γ is constant and $\gamma(T) = \gamma(T = 0)$. This implies that our finite temperature version of SLDA can be reasonably trustable in a range of temperature from 0 to $\sim 0.15T_F$, i.e., in the superfluid phase away from T_c, as well as above T_c where the gas is normal. It is instead less reliable in a range of T below T_c but close to it, where a pseudogap may be present.

With almost the same derivations as in BdG theory, we can calculate the density and order parameter at finite temperature, in the form

$$n = \int \frac{d^3k}{(2\pi)^3} \left[2\frac{\xi_k}{E_k} f(E_k) + \left(1 - \frac{\xi_k}{E_k} \right) \right], \tag{6.1}$$

and

$$\Delta \frac{mn^{1/3}}{\hbar^2 \gamma} = \int \frac{d^3k}{(2\pi)^3} \left[\frac{\Delta}{E_k} f(E_k) - \frac{\Delta}{2} \left(\frac{1}{E_k} - \frac{2m}{\alpha \hbar^2 k^2} \right) \right], \tag{6.2}$$

where $f(x)$ is the Fermi-Dirac distribution function of quasiparticles. By solving the Eqs.(6.1) and (6.2), one extracts the temperature dependence of the chemical potential and the order parameter. The results are shown by solid lines in Fig. 6.2. For comparison, we also show the predictions of BdG theory (dash lines) and the MIT experimental results (dot line) [8]. The SLDA chemical potential is much closer to the experimental data than BdG. SLDA gives also a transition temperature $T_c = 0.33T_F$, better than BdG's prediction $T_c = 0.5T_F$, but still far from the experimental

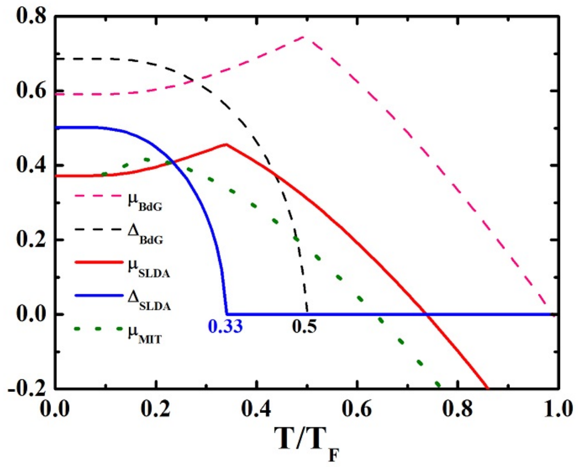

Figure 6.2: Chemical potential μ (red solid line) and order parameter Δ (blue solid line) as a function of temperature obtained with SLDA with T independent parameters α, β and γ. The dashed lines are the same quantities but in BdG theory. The experimental result for the chemical potential [8] is shown as the lowest long dashed line. The transition temperature T_c is $0.33T_F$ in SLDA and $0.5T_F$ in BdG. The SLDA curve of the chemical potential is much closer to the experimental data than BdG.

value $T_c = 0.167T_F$. However, we can consider the overall agreement as reasonably good in first approximation.

We may easily improve the agreement with the experimental data for the chemical potential, by forgetting the QMC results of Fig. 6.1 and using instead the parameters α, β and γ as free parameters to fit the experimental curve. If we set $\alpha = 1$ for simplicity and use β and γ as fitting parameters, we obtain, as a best result, the curve shown in Fig. 6.3, which corresponds to the values $\beta = -0.574$ and $1/\gamma = -0.193$. The agreement is indeed good. However, for consistency reasons, in this thesis we prefer to keep the values which better reproduce the low T behavior of the QMC results of Ref. [7]. The comparison between results obtained with different choices of the parameters will be the natural continuation of this analysis.

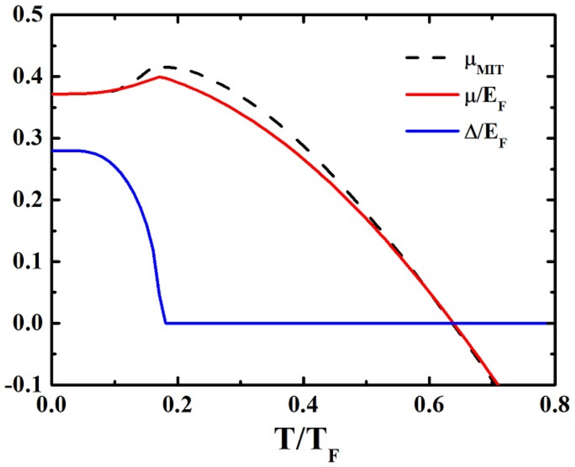

Figure 6.3: Chemical potential μ (red solid line) and order parameter Δ (blue solid line) as a function of temperature obtained with SLDA by using the parameters $\alpha = 1$, $\beta = -0.574$ and $1/\gamma = -0.193$. The MIT experimental results [8] are represented by the black dash line.

6.2 $S(q,\omega)$ at finite temperature

In the previous section we have shown that SLDA can be tuned to reasonably reproduce the equation of state and the transition temperature by properly choosing the parameters of the density functional. We showed that keeping the parameters α, β and γ constant is a sufficiently good approximation for our purposes. Now we want to apply this SLDA within the RPA scheme in order to calculate the density dynamic structure factor, with special attention to the low-q regime, where the role of the order parameter is more significant.

Typical results of our SLDA+RPA calculations are shown in Fig. 5.3 where $S(q,\omega)$ is plotted for three different values of temperature, $T/T_F = 0.2$, 0.3, and 0.4, one in the superfluid phase well below the transition temperature, one close to T_c and one above T_c (with our parameters T_c in SLDA is $0.33T_F$). At low temperature the overall behavior is similar to the one already discussed at zero temperature, with a low energy phononic (bosonic or molecular) collective mode and a gap for single-quasiparticle excitations. The effect of temperature can be seen in a significant

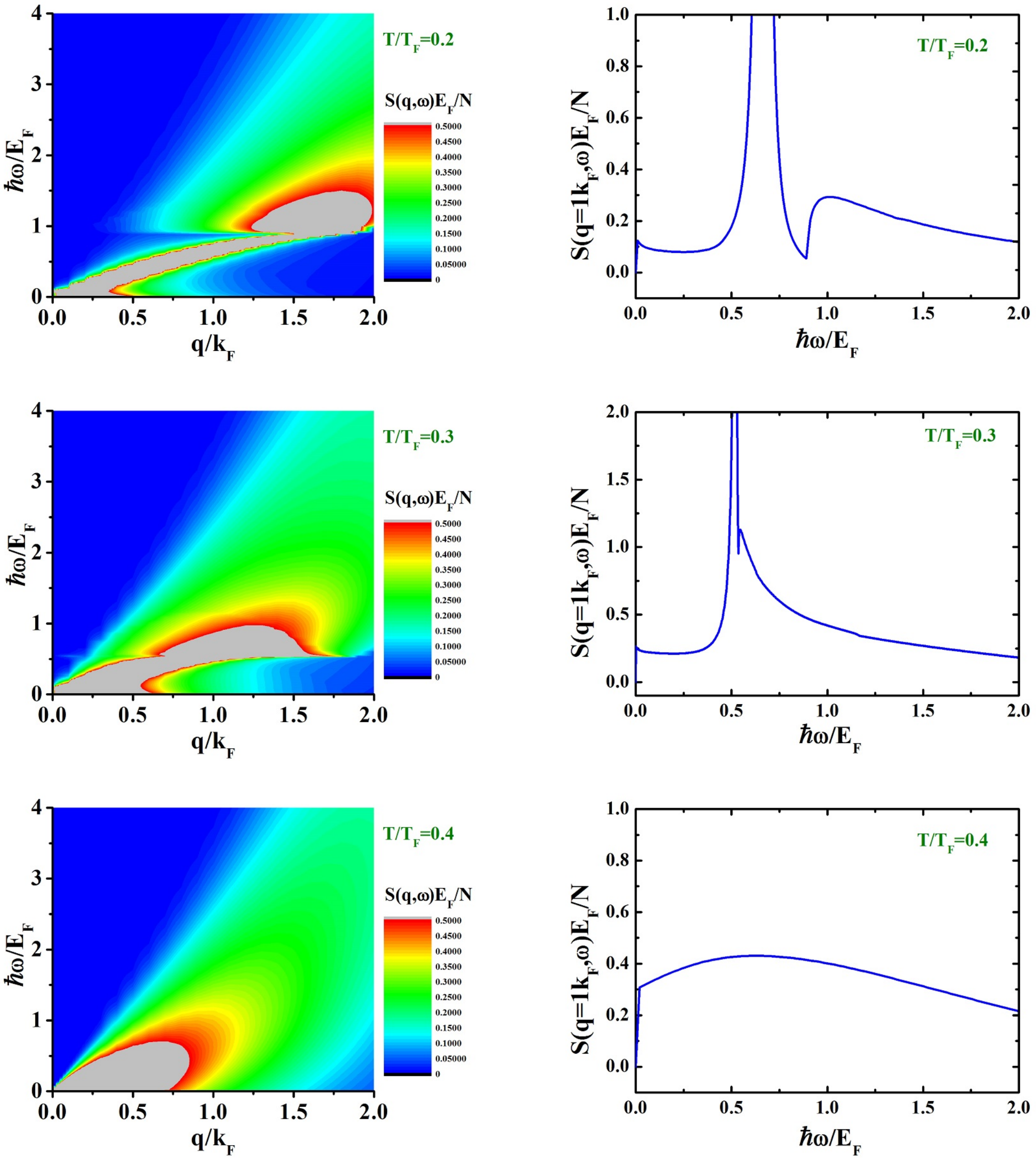

Figure 6.4: The color-plot(left) exhibits the dynamic structure factor at temperature $T/T_F = 0.2, 0.3, 0.4$, for momentum transfer q ranged from $0k_F$ to $2k_F$. When the system is superfluid (the upper and middle two panels), a horizontal line is emergent when the energy transfer ω is equal to the minimum energy $2\Delta(T)$ to break a Cooper-pair at temperature T, while this horizontal line disappear if $T > T_c$ (the under two panels). The right panel is the dynamic structure factor at momentum transfer $q = 1k_F$, when will give a sudden jump when $\omega = 2\Delta(T)/\hbar$ if $T < T_c$.

broadening of the phononic branch as well as in the lowering of the energy gap which eventually disappears above T_c. Near T_c the two peaks overlap while at larger temperature the spectrum is dominated by a single broad distribution of single particle-hole excitations.

In experiment, the realization two-photon Bragg scattering at small momentum transfer is still a big challenge. The dynamic structure factor of superfluid Fermi gas was recently measured at finite temperature [9]. To date, the typical values of momentum transfer q range from $3.8k_F$ to $5k_F$. In this range of relatively large q the atomic peak is centered at the recoil frequency $\omega_r = \hbar q^2/(2m)$, while the molecular peak is centered around $\omega_r/2$. An interesting experimental result is how the magnitude of molecular excitation component of the density dynamic structure factor changes with temperature. For $q = 4k_F$, this is shown in the right panel of Fig. 6.5, where the slope of the molecular peak height *vs.* T reveals two different decreasing trends, with the crossing point located near the superfluid-normal phase transition at temperature $T = T_c$. Actually, this is the method used in [9] to measure the transition temperature $T_c \approx 0.18T_F$, which is not far from MIT experimental value $T_c = 0.167T_F$ [8]. The lowest dotted line in the figure is the prediction for the response at $\omega = \omega_r/2$ in an ideal Fermi gas. The height of the molecular peak can be easily calculated in our RPA scheme. The results are given in the left panel of Fig. 6.5, where the dashed line is the prediction of BdG+RPA and the solid line is the prediction of SLDA+RPA. The comparison between theory and experiment is still preliminary and qualitative, but the figure suggests that this type of comparison can indeed be used as a potential benchmark for finite-temperature theories.

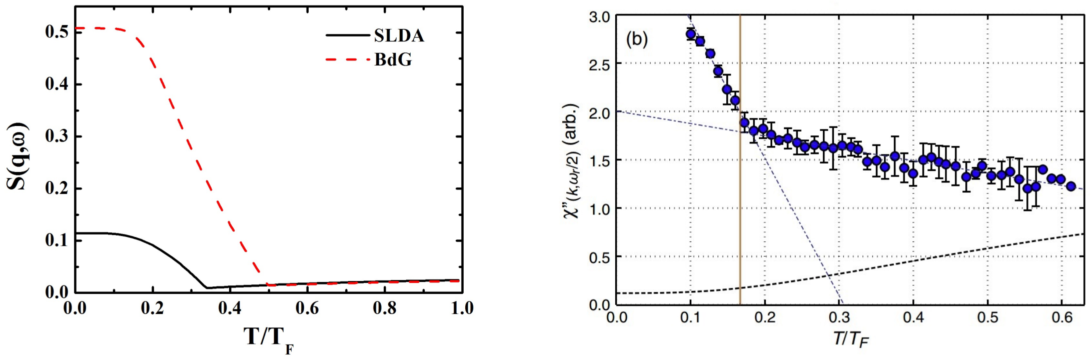

Figure 6.5: Height of molecular peak in dynamic structure factor at $q = 4k_F$ and $\omega = \omega_r/2 \approx 6.86E_F/\hbar$ as a function of temperature. Left panel: SLDA+RPA (black solid line) and BdG+RPA (red dash line). Right panel: experimental data from Bragg scattering [9], in arbitrary units; the vertical line indicates the transition temperature T_c; the lowest dotted line is the prediction for an ideal Fermi gas.

Chapter 7

Conclusions and Perspectives

In this thesis we have studied the dynamics of superfluid Fermi gases at unitarity and in the BCS-BEC crossover by using different approaches of mean-field theory. The main achievements of this thesis are the following.

1. We have investigated the Josephson effect of a two-component Fermi superfluid in a double well potential where a central barrier separates the system into left and right parts. Our strategy has been first to solve the stationary Bogoliubov-de Gennes equations with an offset potential on one side of the barrier, to obtain an initial population imbalance. Then, starting from this configuration, we have solved the time-dependent Bogoliubov-de Gennes equations to investigate the dynamics. For strong barriers the coupling between left and right is weak. In this limit, if the initial population imbalance is smaller than a critical value, we find that the system exhibits a dynamical regime of Josephson oscillations; above this critical value, the system enters the dynamical regime of self-trapping. We have numerically found that the maximum Josephson current I_J is equal to twice the tunneling energy E_J calculated from the difference in energy of the stationary antisymmetric and symmetric states. The period of the Josephson oscillations nicely approaches the prediction of the linear Josephson equations, that is the so-called plasma period T_p, provided the on-site energy E_C and tunneling energy E_J are consistently calculated within the same BdG theory. When the barrier is weak, the coupling between left and right is strong. In this case, a small population im-

balance still induces Josephson oscillations, while for larger imbalance, instead of simple self-trapping oscillations, a more complex dynamics is obtained, with the excitation of sound wave and the creation of solitons.

2. A formal derivation of the two-mode model of superfluid Fermi gases from Bogoliubov-de Gennes theory is still missing. Coupled nonlinear Josephson equations can be instead obtained from a density functional approach based on the use of an appropriate nonlinear Schrödinger equation (or generalized Gross Pitaevskii equation). We have compared the predictions of time-dependent nonlinear Schrödinger equation with those of time-dependent Bogoliubov-de Gennes equations. We have found that these two theories agree with each from the BEC regime to unitarity, while deviations become significant in the BCS regime, where the nonlinear Schrödinger equation does not account for pair-breaking effects.
3. A different density functional approach, known as superfluid local density approximation (SLDA), has been recently introduced to describe fermions at unitarity. This approach includes by constructing a better agreement with experiments and Monte Carlo calculations on some key properties of the systems, such as the equation of state. We have performed simulations in the double well potential with SLDA and compared the results with those of BdG theory. The behaviors of the system are qualitatively the same.
4. An open question about the Josephson effect in superfluid Fermi gases is whether or not one can find π-mode Josephson oscillations and π-mode self-trapping. By using the two-mode model we have searched the conditions required for the occurrence of these regimes. We have found that the particle number should be small and the tunneling energy large, such that these regimes are extremely hard to reach in time-dependent Bogoliubov-de Gennes simulations.
5. We have studied the dynamic structure factor of unitary fermions both at zero and finite temperature using the BdG theory and also SLDA. We have derived the expression of the linear response function and the dynamic structure factor in the random phase approximation. At zero temperature, the

SLDA+RPA formalism indeed provides a better accuracy at low momentum transfer and also its static structure factor is closer to quantum Monte Carlo value than that in BdG+RPA; however SLDA seems to give worse results for the molecular excitations at large momentum transfer. We have discussed the role of temperature and the comparison between SLDA and BdG, as well as with experimental data. The analysis is still at a preliminary level, but it suggests that mean-field theories can indeed be used to extract quantitative information about the order parameter and the excitations of the system by two-photon Bragg scattering experiments. This analysis may also provides some hints about the possible existence of a pseudogap, which is not include in the mean-field theory and whose effect in the dynamic structure factor is an interesting open issue.

The adventure of ultracold Fermi gases is still going on. We hope that our work on fermions can help clarify some aspects of the physics of Josephson effect and the linear response to external perturbations. Thank you for reading.

Appendix A

4th order Runge Kutta method algorithm

Runge Kutta methods are methods for solving the differential equations. They use the function and its first-order derivatives calculated at a given step to find the solution at the next step. Here we will introduce the basic idea of it.

The time evolution of the function $f(t)$ can be written in the generalized form

$$\frac{df(t)}{dt} = g[f,t], \tag{A.1}$$

where function $g[f,t]$ is the appropriate derivative operator for the system. In the absence of the ability to numerically calculate the derivative operator over a continuous rime range, we must instead use algorithms which advance function f between discrete time steps, such that

$$t_{i+1} = t_i + \Delta t, \tag{A.2}$$

where Δt is the time increment between numerically integrated solutions.

One of the most useful, accurate and widely used algorithms for such discrete time step propagation is the 4th order Runge Kutta algorithm. In this method the function at advanced time is written

$$f(t_{i+1}) = f(t_i) + \frac{1}{6}\left[h_1 + 2(h_2 + h_3) + h_4\right] + \mathcal{O}\left(\Delta t^5\right), \tag{A.3}$$

where the individual Runge Kutta terms are calculated as

$$\begin{aligned} h_1 &= g[f(t_i), t_i]\Delta t, && \text{(A.4)} \\ h_2 &= g[f(t_i) + \frac{h_1}{2}, t_i + \frac{\Delta t}{2}]\Delta t, && \text{(A.5)} \\ h_3 &= g[f(t_i) + \frac{h_2}{2}, t_i + \frac{\Delta t}{2}]\Delta t, && \text{(A.6)} \\ h_4 &= g[f(t_i) + h_3, t_i + \Delta t]\Delta t. && \text{(A.7)} \end{aligned}$$

Thus advancing the system by a single time step requires four derivative calculations.

The 4th order Runge Kutta algorithm displays fourth-order accuracy, hence the presence of error terms in Eq. A.3. Extensions of the Runge Kutta to higher orders in general lead to greater numerical accuracy, but at the cost of increased computational requirements.

Bibliography

[1] M. Albiez, R. Gati, J. Fölling, S. Hunsmann, M. Cristiani, M.K. Oberthaler, Direct Observation of Tunneling and Nonlinear Self-Trapping in a Single Bosonic Josephson Junction. Phys. Rev. Lett. **95**, 010402 (2005).

[2] G. Veeravalli, E. Kuhnle, P. Dyke, C.J. Vale, Bragg Spectroscopy of a Strongly Interacting Fermi Gas. Phys. Rev. Lett. **101**, 250403 (2008).

[3] R. Liao, J. Brand, Traveling dark solitons in superfluid Fermi gases. Phys. Rev. A **83**, 041604 (2011).

[4] A. Spuntarelli, P. Pieri, G.C. Strinati, Josephson Effect throughout the BCS-BEC Crossover. Phys. Rev. Lett. **99**, 040401 (2007).

[5] R. Combescot, S. Giorgini, S. Stringari, Molecular signatures in the structure factor of an interacting Fermi gas. EPL (Europhysics Letters) **75**, 695 (2006).

[6] P. Zou, E.D. Kuhnle, C.J. Vale, H. Hu, Quantitative comparison between theoretical predictions and experimental results for Bragg spectroscopy of a strongly interacting Fermi superfluid. Phys. Rev. A **82**, 061605 (2010).

[7] P. Magierski, G. Wlazłowski, A. Bulgac, J.E. Drut, Finite-Temperature Pairing Gap of a Unitary Fermi Gas by Quantum Monte Carlo Calculations. Phys. Rev. Lett. **103**, 210403 (2009).

[8] M.J.H. Ku, A.T. Sommer, L.W. Cheuk, M.W. Zwierlein, Revealing the Superfluid Lambda Transition in the Universal Thermodynamics of a Unitary Fermi Gas. Science **335**, 563 (2012).

[9] M.G. Lingham, K. Fenech, S. Hoinka, C.J. Vale, Local Observation of Pair Condensation in a Fermi Gas at Unitarity. Phys. Rev. Lett. **112**, 100404 (2014).

[10] S.N. Bose, Plancks Gesetz und Lichtquantenhypothese. Zeitschrift fur Physik **26**, 178 (1924).

[11] A. Einstein, Quantentheorie des einatomigen idealen Gases. Zweite Abhandlung, Sitzungsber. Preuss. Akad. Wiss **1925**, 3 (1925).

[12] M.H. Anderson, J.R. Ensher, M.R. Matthews, C.E. Wieman, E.A. Cornell, Observation of Bose-Einstein Condensation in a Dilute Atomic Vapor. Science **269**, 198 (1995).

[13] K.B. Davis, M.-O. Mewes, M.R. Andrews, N.J. van Druten, D.S. Durfee, D.M. Kurn, W. Ketterle, Bose-Einstein Condensation in a Gas of Sodium Atoms. Phys. Rev. Lett. **75**, 3969 (1995).

[14] B. DeMarco, D.S. Jin, Onset of Fermi Degeneracy in a Trapped Atomic Gas. Science **285**, 1703 (1999).

[15] F. Schreck, L. Khaykovich, K.L. Corwin, G. Ferrari, T. Bourdel, J. Cubizolles, C. Salomon, Quasipure Bose-Einstein Condensate Immersed in a Fermi Sea. Phys. Rev. Lett. **87**, 080403 (2001).

[16] A.G. Truscott, K.E. Strecker, W.I. McAlexander, G.B. Partridge, R.G. Hulet, Observation of Fermi Pressure in a Gas of Trapped Atoms. Science **291**, 2570 (2001).

[17] G. Roati, F. Riboli, G. Modugno, M. Inguscio, Fermi-Bose Quantum Degenerate ^{40}K-^{87}Rb Mixture with Attractive Interaction. Phys. Rev. Lett. **89**, 150403 (2002).

[18] Z. Hadzibabic, S. Gupta, C.A. Stan, C.H. Schunck, M.W. Zwierlein, K. Dieckmann, W. Ketterle, Fiftyfold Improvement in the Number of Quantum Degenerate Fermionic Atoms. Phys. Rev. Lett. **91**, 160401 (2003).

[19] C. Chin, R. Grimm, P. Julienne, E. Tiesinga, Feshbach resonances in ultracold gases. Rev. Mod. Phys. **82**, 1225 (2010).

[20] H. Heiselberg, Fermi systems with long scattering lengths. Phys. Rev. A **63**, 043606 (2001).

[21] T.-L. Ho, Universal Thermodynamics of Degenerate Quantum Gases in the Unitarity Limit. Phys. Rev. Lett. **92**, 090402 (2004).

[22] H. Hu, P.D. Drummond, X.-J. Liu, Universal thermodynamics of strongly interacting Fermi gases. Nature Physics **3**, 469 (2007).

[23] K.M. O'Hara, S.L. Hemmer, M.E. Gehm, S.R. Granade, J.E. Thomas, Observation of a Strongly Interacting Degenerate Fermi Gas of Atoms. Science **298**, 2179 (2002).

[24] I. Bloch, Ultracold quantum gases in optical lattices. Nature Physics **1**, 23 (2005).

[25] H. Hu, X.-J. Liu, P.D. Drummond, Universal thermodynamics of a strongly interacting Fermi gas: theory versus experiment. New Journal of Physics **12**, 063038 (2010).

[26] G.E. Astrakharchik, J. Boronat, J. Casulleras, S. Giorgini, Equation of State of a Fermi Gas in the BEC-BCS Crossover: A Quantum Monte Carlo Study. Phys. Rev. Lett. **93**, 200404 (2004).

[27] A. Bulgac, J.E. Drut, P. Magierski, Spin 1/2 Fermions in the Unitary Regime: A Superfluid of a New Type. Phys. Rev. Lett. **96**, 090404 (2006).

[28] E. Burovski, E. Kozik, N. Prokof'ev, B. Svistunov, M. Troyer, Critical Temperature Curve in BEC-BCS Crossover. Phys. Rev. Lett. **101**, 090402 (2008).

[29] J. Carlson, S. Reddy, Superfluid Pairing Gap in Strong Coupling. Phys. Rev. Lett. **100**, 150403 (2008).

[30] Y. Ohashi, A. Griffin, BCS-BEC Crossover in a Gas of Fermi Atoms with a Feshbach Resonance. Phys. Rev. Lett. **89**, 130402 (2002).

[31] Y. Ohashi, A. Griffin, Superfluidity and collective modes in a uniform gas of Fermi atoms with a Feshbach resonance. Phys. Rev. A **67**, 063612 (2003).

[32] H. Hu, X.-J. Liu, P.D. Drummond, Equation of state of a superfluid Fermi gas in the BCS-BEC crossover. EPL (Europhysics Letters) **74**, 574 (2006).

[33] X.-J. Liu, H. Hu, Self-consistent theory of atomic Fermi gases with a Feshbach resonance at the superfluid transition. Phys. Rev. A **72**, 063613 (2005).

[34] R. Haussmann, W. Rantner, S. Cerrito, W. Zwerger, Thermodynamics of the BCS-BEC crossover. Phys. Rev. A **75**, 023610 (2007).

[35] T.-L. Ho, E.J. Mueller, High Temperature Expansion Applied to Fermions near Feshbach Resonance. Phys. Rev. Lett. **92**, 160404 (2004).

[36] X.-J. Liu, H. Hu, P.D. Drummond, Virial Expansion for a Strongly Correlated Fermi Gas. Phys. Rev. Lett. **102**, 160401 (2009).

[37] X.-J. Liu, H. Hu, P.D. Drummond, Three attractively interacting fermions in a harmonic trap: Exact solution, ferromagnetism, and high-temperature thermodynamics. Phys. Rev. A **82**, 023619 (2010).

[38] X.-J. Liu, H. Hu, P.D. Drummond, Exact few-body results for strongly correlated quantum gases in two dimensions. Phys. Rev. B **82**, 054524 (2010).

[39] H. Hu, X.-J. Liu, P.D. Drummond, H. Dong, Pseudogap Pairing in Ultracold Fermi Atoms. Phys. Rev. Lett. **104**, 240407 (2010).

[40] H. Hu, X.-J. Liu, P.D. Drummond, Universal contact of strongly interacting fermions at finite temperatures. New Journal of Physics **13**, 035007 (2011).

[41] S. Giorgini, L.P. Pitaevskii, S. Stringari, Theory of ultracold atomic Fermi gases. Rev. Mod. Phys. **80**, 1215 (2008).

[42] B.D. Josephson, Possible new effects in superconductive tunnelling. Physics Letters **1**, 251 (1962).

[43] A. Barone, G. Paterno, *Physics and Applications of the Josephson Effect* (Wiley, New York, 1982).

[44] A.J. Leggett, Bose-Einstein condensation in the alkali gases: Some fundamental concepts. Rev. Mod. Phys. **73**, 307 (2001).

[45] L.P. Pitaevskii, S. Stringari, *Bose-Einstein Condensation* (Oxford University Press, 2003).

[46] R. Gati, M.K. Oberthaler, A bosonic Josephson junction. Journal of Physics B: Atomic, Molecular and Optical Physics **40**, 61 (2007).

[47] A. Smerzi, S. Fantoni, S. Giovanazzi, S.R. Shenoy, Quantum Coherent Atomic Tunneling between Two Trapped Bose-Einstein Condensates. Phys. Rev. Lett. **79**, 4950 (1997).

[48] S. Raghavan, A. Smerzi, S. Fantoni, S.R. Shenoy, Coherent oscillations between two weakly coupled Bose-Einstein condensates: Josephson effects, π oscillations, and macroscopic quantum self-trapping. Phys. Rev. A **59**, 620 (1999).

[49] E.A. Ostrovskaya, Y.S. Kivshar, M. Lisak, B. Hall, F. Cattani, D. Anderson, Coupled-mode theory for Bose-Einstein condensates. Phys. Rev. A **61**, 031601 (2000).

[50] D. Ananikian, T. Bergeman, Gross-Pitaevskii equation for Bose particles in a double-well potential: Two-mode models and beyond. Phys. Rev. A **73**, 013604 (2006).

[51] F.S. Cataliotti, S. Burger, C. Fort, P. Maddaloni, F. Minardi, A. Trombettoni, A. Smerzi, M. Inguscio, Josephson Junction Arrays with Bose-Einstein Condensates. Science **293**, 843 (2001).

[52] T. Anker, M. Albiez, R. Gati, S. Hunsmann, B. Eiermann, A. Trombettoni, M.K. Oberthaler, Nonlinear Self-Trapping of Matter Waves in Periodic Potentials. Phys. Rev. Lett. **94**, 020403 (2005).

[53] T. Zibold, E. Nicklas, C. Gross, M.K. Oberthaler, Classical Bifurcation at the Transition from Rabi to Josephson Dynamics. Phys. Rev. Lett. **105**, 204101 (2010).

[54] S. Levy, E. Lahoud, I. Shomroni, J. Steinhauer, The a.c. and d.c. Josephson effects in a Bose-Einstein condensate. Nature **449**, 579 (2007).

[55] L.J. LeBlanc, A.B. Bardon, J. McKeever, M.H.T. Extavour, D. Jervis, J.H. Thywissen, F. Piazza, A. Smerzi, Dynamics of a Tunable Superfluid Junction. Phys. Rev. Lett. **106**, 025302 (2011).

[56] A. Spuntarelli, P. Pieri, G.C. Strinati, Solution of the Bogoliubov-de Gennes equations at zero temperature throughout the BCS-BEC crossover: Josephson and related effects. Physics Reports **488**, 111 (2010).

[57] F. Ancilotto, L. Salasnich, F. Toigo, dc Josephson effect with Fermi gases in the Bose-Einstein regime. Phys. Rev. A **79**, 033627 (2009).

[58] L. Salasnich, N. Manini, F. Toigo, Macroscopic periodic tunneling of Fermi atoms in the BCS-BEC crossover. Phys. Rev. A **77**, 043609 (2008).

[59] L. Salasnich, F. Ancilotto, N. Manini, F. Toigo, DC and AC Josephson effects with superfluid Fermi atoms across a Feshbach resonance. Laser Physics **19**, 636 (2009).

[60] S.K. Adhikari, H. Lu, H. Pu, Self-trapping of a Fermi superfluid in a double-well potential in the Bose-Einstein-condensate-unitarity crossover. Phys. Rev. A **80**, 063607 (2009).

[61] G. Watanabe, F. Dalfovo, F. Piazza, L.P. Pitaevskii, S. Stringari, Critical velocity of superfluid flow through single-barrier and periodic potentials. Phys. Rev. A **80**, 053602 (2009).

[62] A. Bulgac, Y. Yu, Superfluid LDA (SLDA): Local Density Approximation for Systems with Superfluid Correlations. International Journal of Modern Physics E **13**, 147 (2004).

[63] A. Bulgac, Local-density-functional theory for superfluid fermionic systems: The unitary gas. Phys. Rev. A **76**, 040502 (2007).

[64] A. Bulgac, M. Forbes, P. Magierski, The Unitary Fermi Gas: From Monte Carlo to Density Functionals, in *The BCS-BEC Crossover and the Unitary Fermi Gas*, ed. by W. Zwerger. Lecture Notes in Physics, vol. 836 (Springer Berlin Heidelberg, 2012)., pp. 305. ISBN 978-3-642-21977-1

[65] S.B. Papp, J.M. Pino, R.J. Wild, S. Ronen, C.E. Wieman, D.S. Jin, E.A. Cornell, Bragg Spectroscopy of a Strongly Interacting ^{85}Rb Bose-Einstein Condensate. Phys. Rev. Lett. **101**, 135301 (2008).

[66] S. Hoinka, M. Lingham, M. Delehaye, C.J. Vale, Dynamic Spin Response of a Strongly Interacting Fermi Gas. Phys. Rev. Lett. **109**, 050403 (2012).

[67] A. Griffin, *Excitations in a Bose-condensed Liquid* (Cambridge University Press, 1993).

[68] A.L. Fetter, J.D. Walecka, *Quantum Theory of Many-particle Systems* (New York: McGraw-Hill, 1971).

[69] H. Hu, Many-body theories of density response for a strongly correlated Fermi gas. Frontiers of Physics **7**, 98 (2011).

[70] S. Tan, Energetics of a strongly correlated Fermi gas. Annals of Physics **323**, 2952 (2008).

[71] S. Tan, Large momentum part of a strongly correlated Fermi gas. Annals of Physics **323**, 2971 (2008).

[72] S. Tan, Generalized virial theorem and pressure relation for a strongly correlated Fermi gas. Annals of Physics **323**, 2987 (2008).

[73] E.M. Lifshitz, L.P. Pitaevskii, *Statistical Physics* (Oxford, 1980).

[74] H. Hu, X.-J. Liu, Universal dynamic structure factor of a strongly correlated Fermi gas. Phys. Rev. A **85**, 023612 (2012).

[75] D.M. Eagles, Possible Pairing without Superconductivity at Low Carrier Concentrations in Bulk and Thin-Film Superconducting Semiconductors. Phys. Rev. **186**, 456 (1969).

[76] A.J. Leggett, *Modern Trends in the Theory of Condensed Matter* (Springer, Berlin, 1980).

[77] M. Randeria, *Bose-Einstein Condensation* (Cambridge University Press, 1995).

[78] A. Bulgac, Local density approximation for systems with pairing correlations. Phys. Rev. C **65**, 051305 (2002).

[79] J. Reidl, A. Csordás, R. Graham, P. Szépfalusy, Finite-temperature excitations of Bose gases in anisotropic traps. Phys. Rev. A **59**, 3816 (1999).

[80] X.-J. Liu, H. Hu, P.D. Drummond, Mean-field thermodynamics of a spin-polarized spherically trapped Fermi gas at unitarity. Phys. Rev. A **75**, 023614 (2007).

[81] A. Bulgac, Y. Yu, Renormalization of the Hartree-Fock-Bogoliubov Equations in the Case of a Zero Range Pairing Interaction. Phys. Rev. Lett. **88**, 042504 (2002).

[82] M. Antezza, F. Dalfovo, L.P. Pitaevskii, S. Stringari, Dark solitons in a superfluid Fermi gas. Phys. Rev. A **76**, 043610 (2007).

[83] Y.-H. Hou, L.P. Pitaevskii, S. Stringari, Scaling solutions of the two-fluid hydrodynamic equations in a harmonically trapped gas at unitarity. Phys. Rev. A **87**, 033620 (2013).

[84] R.G. Scott, F. Dalfovo, L.P. Pitaevskii, S. Stringari, Dynamics of Dark Solitons in a Trapped Superfluid Fermi Gas. Phys. Rev. Lett. **106**, 185301 (2011).

[85] F. Piazza, L.A. Collins, A. Smerzi, Current-phase relation of a Bose-Einstein condensate flowing through a weak link. Phys. Rev. A **81**, 033613 (2010).

[86] N. Manini, L. Salasnich, Bulk and collective properties of a dilute Fermi gas in the BCS-BEC crossover. Phys. Rev. A **71**, 033625 (2005).

[87] M. McNeil Forbes, R. Sharma, Validating Simple Dynamical Simulations of the Unitary Fermi Gas. arXiv:1308.4387 (2013).

[88] R. Combescot, M.Y. Kagan, S. Stringari, Collective mode of homogeneous superfluid Fermi gases in the BEC-BCS crossover. Phys. Rev. A **74**, 042717 (2006).

[89] P. Hohenberg, W. Kohn, Inhomogeneous Electron Gas. Phys. Rev. **136**, 864 (1964).

[90] W. Kohn, Nobel Lecture: Electronic structure of matterwave functions and density functionals. Rev. Mod. Phys. **71**, 1253 (1999).

[91] R.M. Dreizler, E.K.U. Gross, *Density Functional Theory: An Approach to the Quantum Many-Body Problem* (Springer, Berlin, 1990).

[92] W. Kohn, L.J. Sham, Self-Consistent Equations Including Exchange and Correlation Effects. Phys. Rev. **140**, 1133 (1965).

[93] Y. Yu, A. Bulgac, Energy Density Functional Approach to Superfluid Nuclei. Phys. Rev. Lett. **90**, 222501 (2003).

[94] Y. Yu, A. Bulgac, Spatial Structure of a Vortex in Low Density Neutron Matter. Phys. Rev. Lett. **90**, 161101 (2003).

[95] A. Bulgac, Y. Yu, Vortex State in a Strongly Coupled Dilute Atomic Fermionic Superfluid. Phys. Rev. Lett. **91**, 190404 (2003).

[96] A. Bulgac, Y. Yu, Signatures of Superfluidity in Dilute Fermi Gases near a Feshbach Resonance. Journal of Low Temperature Physics **138**, 741 (2005).

[97] J. Carlson, S. Reddy, Asymmetric Two-Component Fermion Systems in Strong Coupling. Phys. Rev. Lett. **95**, 060401 (2005).

[98] J. Carlson, S. Gandolfi, K.E. Schmidt, S. Zhang, Auxiliary-field quantum Monte Carlo method for strongly paired fermions. Phys. Rev. A **84**, 061602 (2011).

[99] M.M. Forbes, S. Gandolfi, A. Gezerlis, Resonantly Interacting Fermions in a Box. Phys. Rev. Lett. **106**, 235303 (2011).

[100] A. Schirotzek, Y.-i. Shin, C.H. Schunck, W. Ketterle, Determination of the Superfluid Gap in Atomic Fermi Gases by Quasiparticle Spectroscopy. Phys. Rev. Lett. **101**, 140403 (2008).

[101] A. Bulgac, Time-Dependent Density Functional Theory and the Real-Time Dynamics of Fermi Superfluids. Annual Review of Nuclear and Particle Science **63**, 97 (2013).

[102] A. Bulgac, M.M. Forbes, M.M. Kelley, K.J. Roche, G. Wlazłowski, Quantized Superfluid Vortex Rings in the Unitary Fermi Gas. Phys. Rev. Lett. **112**, 025301 (2014).

[103] A. Bulgac, Y.-L. Luo, P. Magierski, K.J. Roche, Y. Yu, Real-Time Dynamics of Quantized Vortices in a Unitary Fermi Superfluid. Science **332**, 1288 (2011).

[104] A. Bulgac, Y.-L. Luo, K.J. Roche, Quantum Shock Waves and Domain Walls in the Real-Time Dynamics of a Superfluid Unitary Fermi Gas. Phys. Rev. Lett. **108**, 150401 (2012).

[105] S. Stringari, Density and Spin Response Function of a Normal Fermi Gas at Unitarity. Phys. Rev. Lett. **102**, 110406 (2009).

[106] A. Minguzzi, G. Ferrari, Y. Castin, Dynamic structure factor of a superfluid Fermi gas. The European Physical Journal D - Atomic, Molecular, Optical and Plasma Physics **17**, 49 (2001).

[107] G.M. Bruun, B.R. Mottelson, Low Energy Collective Modes of a Superfluid Trapped Atomic Fermi Gas. Phys. Rev. Lett. **87**, 270403 (2001).

[108] S. Hoinka, M. Lingham, K. Fenech, H. Hu, C.J. Vale, J.E. Drut, S. Gandolfi, Precise Determination of the Structure Factor and Contact in a Unitary Fermi Gas. Phys. Rev. Lett. **110**, 055305 (2013).

List of Publications

The major contents of this thesis have already appeared in some of the following papers:

- **Peng Zou** and Franco Dalfovo,
  Josephson oscillations and self-trapping of superfluid fermions in a double-well potential
  arXiv:1401.2007 (2014).
- **Peng Zou**, Hui Hu and Franco Dalfovo,
  Dynamic structure factor within superfluid local density approximation
  in preparation.